CENTRO DE INVESTIGACIÓN Y DE ESTUDIOS AVANZADOS
DEL INSTITUTO POLITÉCNICO NACIONAL

UNIDAD ZACATENCO

PROGRAMA DE NANOCIENCIAS Y NANOTECNOLOGÍA

Síntesis y aplicaciones de nanofósforos de niobato de gadolinio

T E S I S

que presenta

Anastasiya Sedova

Para obtener el grado de

DOCTORA EN CIENCIAS

EN NANOCIENCIAS Y NANOTECNOLOGÍA

Director de la tesis:

Dr. Ciro Falcony Guajardo

Ciudad de México **Diciembre, 2021**

CENTER FOR RESEARCH AND ADVANCED STUDIES OF THE NATIONAL POLYTECHNIC INSTITUTE

ZACATENCO CAMPUS

NANOSCIENCE AND NANOTECHNOLOGY PROGRAM

Gadolinium niobate nanophosphors: synthesis and applications

T H E S I S

submitted by

Anastasiya Sedova

In order to obtain the

DOCTOR IN SCIENCE

IN NANOSCIENCE AND NANOTECHNOLOGY

Advisor:

Dr. Ciro Falcony Guajardo

Mexico City **December, 2021**

Acknowledgements

I am grateful to my Ph.D. advisor Dr. Ciro Falcony Guajardo, for full support, supervision, and understanding all along the period of my doctoral work. Also, I am grateful to Dr. Ciro Falcony's group for the help in the lab and support.

Thanks to academic coordinator Dr. José Gerardo Cabañas Moreno for being supportive, responsive, and helpful in the academic affairs all along my Ph.D. stay.

Thanks to my Ph.D. committee: Dr. Miguel Angel Aguilar Frutis, Dr. José Gerardo Cabañas Moreno, Dr. Jaime Santoyo Salazar and Dr. Manuel García Hipólito for supervising me along the way.

Many thanks to the staff scientists Zacarías Rivera Álvarez for all the help regarding lab affairs, Marcela Guerrero for the assistance with XRD and FTIR, and Ana Bertha Soto and Angel Guillén Cervantes for the help with SEM.

Thanks to Dr. Miriam Marisol Tellez Cruz for the help with multiple analyses such as FTIR, Raman, UV-Vis, and XRD.

I am grateful to Marco Antonio Leyva Ramírez and Dr. Karina Suárez Alcántara for their assistance with XRD measurements. Thanks to Dr. Ana Maria Arizmendi Morquecho, Dr. José Martín Herrera Ramírez and Luis Gerardo Silva Vidaurri for their help with the XPS measurements. Also, I am thankful to Dr. Nicolás Cayetano Castro, Dr. Daniel Bahena Uribe and Dr. Josué Esaú Romero Ibarra for their assistance with TEM images.

I am grateful to my family for their support, especially to my dear husband, Dr. David Bermúdez Rosales, for being along my side during my Ph.D. and for his help with calculations regarding Mie scattering theory.

Funding: I am grateful for the financial support from Consejo Nacional de Ciencia y Tecnología (CONACYT), PhD scholarship 623213, "ayudantes de investigadores SNI" and Project CB-A1-S-26432 of Dr. Ciro Falcony. Also, I am thankful for the financial support from CINVESTAV.

Contents

Abstract

Luminescence characteristics of nanophosphors are of great interest for various applications, such as sensors, light-emitting diodes, lasers, *etc*. The common form of such materials is a host matrix doped with luminescent activators such as rare earth elements. The host matrix plays an important role in the sensitization of the activators in the photoluminescence processes. The $GdNbO_4$ micro-particles synthesized by the solid-state reaction are proposed in the literature as an efficient host matrix for Tm^{3+}/Yb^{3+} and Ho^{3+}/Yb^{3+} dopants for multi-modal luminescence. The $GdNbO_4$ and $GdTiNbO_6$ materials synthesized by the hydrothermal technique and co-doped with Er^{3+}/Yb^{3+} show efficient up-conversion characteristics. Nevertheless, control over the $GdNbO_4$ and $GdTiNbO_6$ morphologies during the synthesis remains a challenge.

In this work, controlled hydrothermal synthesis of a new $GdNb_2O_6$ compound is developed for optical applications. The nanoscale bar-, cube-, and flower-like morphologies are synthesized solely by strict control of pH and temperature of the precursors' solution and without the addition of any surfactant. A mixed $GdNb_2O_6/GdNbO_4$ phase is obtained for the flower-like morphology. The $GdNb_2O_6$ has an aeschynite-type orthorhombic crystalline phase and a *Pnma* (62) space group, similar to $GdTiNbO_6$.

This work contains a study on the intrinsic and water-related photoluminescence emissions of $GdNb_2O_6$. Doping of $GdNb_2O_6$ compound with Tm^{3+} ions ($Gd_{1-x}Tm_xNb_2O_6$) leads to λ_{em} = 457 nm emission, excited with λ_{ex} = 361 nm. In addition, doping this compound with Nd^{3+} ions result in an efficient emission in the near-infrared (NIR) region. The Nd^{3+} doped ($Gd_{1-x}Nd_xNb_2O_6$) cube-like morphology is tested for random laser application.

The cube- and bar-like morphologies of $GdNb_2O_6$ present Mie resonance in the UV-vis-NIR region. This phenomenon is studied by experimental and theoretical means in the current work.

These $GdNb_2O_6$, $Gd_{1-x}Tm_xNb_2O_6$, and $Gd_{1-x}Nd_xNb_2O_6$ compounds can be potentially used in applications such as random lasers, photonics, solar cells, *etc*.

Resumen

Las características de luminiscencia de nanofósforos son de gran interés para varias aplicaciones, tales como en sensores, diodos emisores de luz, láseres, etc. La forma más común de tales materiales es una matriz huésped dopada de activadores luminiscentes como algunos elementos de tierras raras. La matriz huésped juega un papel importante en la sensibilización de los activadores en los procesos de fotoluminiscencia. Las micropartículas de $GdNbO_4$ sintetizadas por una reacción de estado sólido se han propuesto en la literatura como una matriz huésped eficiente para dopantes Tm^{3+}/Yb^{3+} y Ho^{3+}/Yb^{3+} para luminiscencia multimodal. Los materiales $GdNbO_4$ y $GdTiNbO_6$ sintetizados por la técnica hidrotérmica y codopados con Er^{3+}/Yb^{3+} muestran características de conversión ascendente eficiente. Sin embargo, el control sobre las morfologías de $GdNbO_4$ y $GdTiNbO_6$ durante la síntesis es todavía un reto.

En este trabajo, una síntesis hidrotérmica controlada de un nuevo compuesto de $GdNb_2O_6$ es desarrollada para aplicaciones ópticas. Las morfologías nanoscópicas tipo barras, cubos y flores son sintetizadas únicamente con el control estricto del pH y la temperatura de la solución de los precursores y sin la adicción de ningún surfactante. Se obtiene una fase mezcla $GdNb_2O_6/GdNbO_4$ para la morfología tipo flor. El compuesto $GdNb_2O_6$ tiene una fase cristalina ortorrómbica tipo esquinita y un grupo espacial *Pnma* (62), similar al de $GdTiNbO_6$.

Este trabajo contiene un estudio de las emisiones fotoluminiscentes intrínsecas y relacionadas con agua del $GdNb_2O_6$. Dopando el compuesto $GdNb_2O_6$ con iones de Tm^{3+} ($Gd_{1-x}Tm_xNb_2O_6$) lleva a $\lambda_{em} = 361$ nm. Además, el dopaje de este compuesto con iones de Nd^{3+} resulta en una emisión eficiente en la región de infrarrojo cercano (NIR). La morfología tipo cubo del compuesto dopado con Nd^{3+} ($Gd_{1-x}Nd_xNb_2O_6$) se prueba para una aplicación como láser aleatorio.

Las morfologías tipo cubo y barra del $GdNb_2O_6$ presentan resonancia Mie en las regiones UV-Vis-NIR (ultravioleta-visible-infrarrojo cercano). Este fenómeno es estudiado en este trabajo por medios experimentales y teóricos. Estos

compuestos de $GdNb_2O_6$, $Gd_{1-x}Tm_xNb_2O_6$ y $Gd_{1-x}Nd_xNb_2O_6$ podrían potencialmente ser usados en aplicaciones como láseres aleatorios, fotónica, celdas solares, etc.

1. Introduction

Niobium oxides are a broad family of materials with diverse compositions and applications in the macro and nanoscale. The Nb_2O_5 semiconductor (band gap of 3.4 eV) is widely studied for several applications such as electrochromic materials [1], lithium storage [2], supercapacitors [3], and others [4]. Alkali niobates perovskites ($ANbO_3$, A = Li, K, Na) presented nonlinear optical emission [5] and great photocatalytic activity [6]. Alkaline earth and transition-metal niobates with general formula ANb_2O_6 (A = divalent cation) adopt orthorhombic and monoclinic crystalline structures [7–10]. This broad group of compounds has applications in energy storage [11], photoluminescence (PL) [12], photoelectrochemistry [13], *etc*.

The intrinsic [14,15] and doped [14,16–18] gadolinium niobates such as $GdNbO_4$ are drawing substantial attention for optical applications in the past years. Nevertheless, control over the morphology of gadolinium niobate compounds in the nanoscale is still a challenge, and only a few studies are reported [19,20]. Also, thermal treatments at elevated temperatures ($T \geq 1000$ ˚C) are often essential to obtain an efficient optical emission [17,20]. These thermal treatments result in aggregation of the nanomaterials and make them difficult to disperse in solvents and polymeric media and, as a result limiting their use.

Submicron particles supporting Mie resonance in the UV-Vis and near-infrared (NIR) regions offer a range of applications such as enhanced photoluminescence [21], lasing [22], low-loss meta-optics [23], coloring [24], enhanced Raman scattering [25], *etc*. The most studied materials for these applications are spherical crystalline silicon [24,26], perovskites [21,22,27], and gold and silver nanoparticles (NP's) [28]. The Mie resonance is not limited to spherical particles and is observed in cube-shape halide perovskites ($CsPbBr_3$)[21], random-shape $MAPbI_3$ [22], and fullerene-like WS_2 NP's [29]. Among the studied materials, all-dielectrics with high refractive indices such as silicon [25] and germanium [30] offer a great alternative to the plasmonic gold and silver NP's [31].

Replacing the plasmonic NP's with all-dielectrics allows overcoming some limitations such as energy dissipation and absorption [31].

1.1. Photoluminescence

Luminescent materials are of great interest for many applications, such as lasers, light-emitting diodes (LEDs), cathode rays' tubes, field emission displays, sensors, etc. The most attractive luminescent materials are lanthanides (rare-earth) doped phosphors. Lanthanides are commonly used as trivalent ions (Ln^{+3}) (**Figure 1.1.1a**). Their emission (usually high color purity) is due to the f-f transitions inside the 4f shell [32]. The partially filled 4f shell is isolated from the environment by the closed $5s^2$ and $5p^6$ shells. This shielding is responsible for narrowband emission and the long lifetimes of the excited states. Photoluminescence (PL) of lanthanide ions is usually very efficient. Nevertheless, all lanthanide ions suffer from weak light absorption and, as a result, weak emission. The problem of weak light absorption can be overcome by energy sensitization processes such as energy transfer through the charge transfer band (CTB), codopants, ligands, etc. Another possibility is using self-activated matrices [18]. Lanthanides doped phosphors can transfer energy by various mechanisms such as downshifting (DS), quantum cutting (QC), and up-conversion (UC) (**Figure 1.1.1b**) [33]. In the DS process, after absorption of a high-energy photon by the system, a non-radiative relaxation takes place, followed by the emission of a lower energy photon. As for QC, a two-step radiative relaxation of two or more low-energy photons occurs upon absorption of a high-energy photon [34]. Up-conversion is a non-linear optical process, where two or more absorbed low energy photons (near-infrared - NIR) are emitted as a single high energy photon (ranging from NIR to ultraviolet - UV) [33]. Luminescence by all three processes in the same material is called multi-modal luminescence [35].

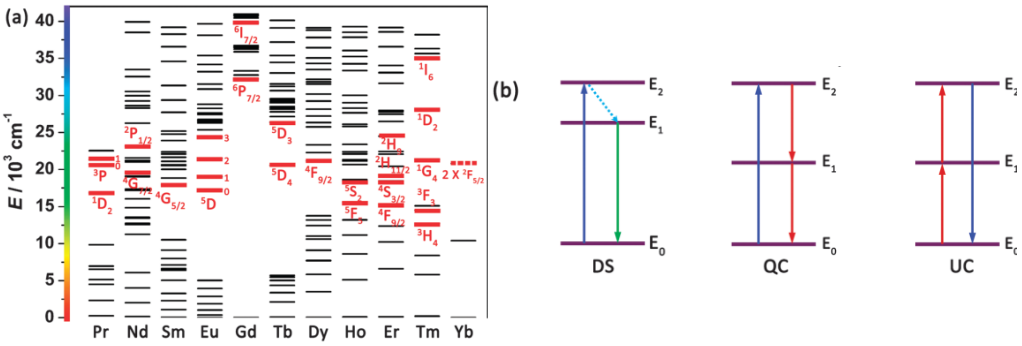

Figure 1.1.1. (a) Partial energy level diagrams of Ln^{3+}. Corresponding typical UC emissive excited levels are highlighted with red bold lines. (b) Schematic illustration of the three energy transfer modes of Ln^{3+}. From left to right, these are DS, QC, and UC. Upward and downward full arrows stand for photon excitation and emission processes, respectively. The dashed line represents a non-radiative relaxation process [33].

1.2. Hydrothermal Process

The hydrothermal technique is simple, low-cost, and commonly used for inorganic nano/microstructures synthesis [36]. This process is defined as "Any heterogeneous or homogeneous chemical reaction in the presence of solvent (whether aqueous or non-aqueous) above room temperature and at a pressure greater than 1 atm in a closed system" [37]. For the non-aqueous solvent or solvents in or near supercritical conditions, the process is more frequently called solvothermal [36]. The pressure developed inside the closed chamber is described as a function of the temperature and percentage of the filled vessel (**Figure 1.2.1**) [38]. Hydrothermal conditions can affect the reactivity and solubility of inorganic materials. The hydrothermal process is originated in nature, and it is the main process responsible for the formation of the Earth's crust minerals [39]. The hot to warm fluids (T = 50 to > 500 ˚C) circulation facilitates the formation of the mineral deposits. Water circulation followed by

the physico-chemical conditions allows the mineral precursors to be leached, transported, and finally precipitated. Water polarity is crucial in hydrothermal processes. Consequently, water is a good cations ligand for processes like hydration and hydrolysis. When water is surrounding the ion of interest, the dissolution process occurs. In some cases, the water of crystallization is a part of the mineral lattice [39]. Beyond the critical temperature ($T_c \approx 400$ ˚C) and pressure ($P_c \approx 40$ MPa), water properties change. This water is termed "supercritical" [40]. Supercritical water is less dense and becomes compressible. The density variates with temperature and pressure. In addition, dielectric constant drops with the pressure ($\varepsilon = 1 - 10$) compared to the value ($\varepsilon = 80$) at normal conditions ($T < 400$ ˚C, $P_c < 40$ MPa).

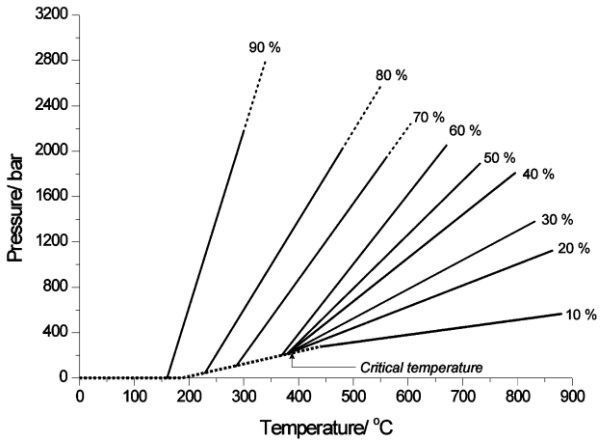

Figure 1.2.1. Pressure as a function of temperature and percentage fill of water in a sealed vessel [38].

1.3. Gadolinium Niobates

Materials of the type AB_2O_6 (A = RE: rare earth, B = Ti and Nb) are of interest for optical applications such as luminescence [17,41] and laser gain media [42]. For RE = La, Ce, Pr, Nd, Sm, and Eu (atomic number Z = 57-63), these compounds have aeschynite crystalline phase, and for RE = Gd, Tb, Dy, Ho, Er,

Tm, Yb, Lu (Z = 64-71) the phase can be aeschynite or euxenite depending on the synthesis conditions [42–44]. The (Eu, Gd)$TiNbO_6$ synthesized *via* hydrothermal method has an aeschynite-type orthorhombic crystalline phase with a *Pnma* (62) space group [43]. Annealing this material at 1300 ˚C leads to a euxenite-type orthorhombic crystalline structure with a *Pbcn* (60) space group. The aeschynite-type $EuTiNbO_6$ has an indirect band gap (Eg) of 3.55 eV [45]. Co-doping of $GdTiNbO_6$ with Er^{3+}/Yb^{3+} leads to up-conversion PL [17].

Other niobate compounds of type $ANbO_4$ (A = RE^{3+}) are monoclinic with a fergusonite structure and a space group *C12/c1* (15) [46,47]. In the $GdNbO_4$ matrix, the niobate groups (NbO_4^{3-}) act as fluorescent centers with blue emission under UV excitation [16]. When the NbO_4^{3-} groups are excited, the absorbed energy is transferred to the Gd^{3+} ions. This process leads to luminescence quenching due to the abundance of gadolinium ions. On the other hand, when the excitation is through the Gd^{3+} ions, the energy is transferred in a nonradiative manner to the NbO_4^{3-} groups, resulting in stronger luminescence [18]. A typical luminescence spectrum of the $GdNbO_4$ is a broad peak centered at 440 nm [14,15], excited with 254 [48] and 305 [49] nm. The submicron mesoporous $GdNbO_4$ presents a distinct behavior of broad emission between 400 – 600 nm with peaks maxima at 440, 483, and 522 nm when excited with 346 nm [19]. The $GdNbO_4$ is an indirect band gap material with Eg of 3.745 eV according to the first-principle calculation and 3.84 eV extracted experimentally [50]. The experimental refractive index (*n*) of this material is about 2.15 and calculated 2.14 – 2.108 (wavelength range 600 – 2000 nm) [51]. Multi-modal luminescence is present in $GdNbO_4$ microcrystals co-doped with Yb^{+3}/Tm^{+3} [16] and Yb^{+3}/Ho^{+3} [18]. The $GdNbO_4$ nanoparticles (NP's) co-doped with Yb^{+3}/Er^{+3} synthesized by the hydrothermal technique show efficient up-conversion characteristics [14]. Doping of $GdNbO_4$ with Nd^{3+} ions leads to a near-infrared (NIR) emission incorporated in lasers and solar cells in macro [52,53] and nanoscale [54]. Numerous works are published on a solid-state synthesis of $GdNbO_4$ microcrystals [15,18]. In the case of the sol-gel reaction, spherical $GdNbO_4$ NP's are realized [20]. Only a few studies reported the

hydrothermal synthesis of $GdNbO_4$ micro [55] and nanocrystals [56]. Recently, mesoporous nanospheroids of this material were synthesized by the hydrothermal process with the assistance of Ethylenediaminetetraacetic acid (EDTA) [19]. These Eu^{+3} doped $GdNbO_4$ mesoporous nanospheroids are promising nanoprobes for multimodal bio-imaging and photodynamic therapy.

1.4. Rietveld Analysis

Rietveld analysis is named after Hugo Rietveld, who developed a computer-based procedure to analyze diffraction data [57,58]. This method consists of least-squares refinements that are carried on until the best fit between the experimental and the calculated data is obtained. In the refinement, the diffraction optics effects, instrumental factors, and structural characteristics (lattice parameters, space group, *etc.*) are considered [58]. Rietveld analysis uses step intensity data *y(i)*, where each data point is observable. The full diffraction pattern is considered with different parameters that can be refined. For polycrystalline materials, the three-dimensional reciprocal lattice is reduced to a one-dimensional diagram, leading to peaks overlap [57]. This problem is solved by using the step-scanned profile intensities instead of integrated ones. Diffraction pattern can provide information on the crystal structure (peaks intensities), atomic positions, lattice parameters and space group (from peaks position), amorphous fraction in the sample and local order/disorder (from the background), particles size, strain/stress, and domain size (from the broadening of the peak). In addition, qualitative and quantitative phase analysis can be performed [57].

In the Rietveld analysis, several parameters indicate the goodness of fit between the experimental and the calculated diffraction data. One of them is the profile fitting R-factor (R_p) (**equation 1.4.1**) that is calculated from the difference between the observed *y(i)*(obs.) and the calculated *y(i)*(calc.) step intensities at

the observed scanning points Δ(2-theta), before any calculation or refinement [57]. This calculation can be done, on a single peak, various peaks, or the full profile. The important factor in this calculation is the absolute number of counts (*y(i)*(obs.)).

(1.4.1.)

$$R_p = \frac{\sum_i |y_i(obs.) - y_i(clac.)|}{\sum_i |y_i(obs.)|}$$

The second parameter is the weighted R-factor (R_{wp}), where w_i (**equation 1.4.2**) is the weight taken from the experimental error margins [57]. The experimental standard deviation of the observed counts (y_i'(obs.)) is strongly dependent on the Bragg scattering and the background.

(1.4.2.)

$$w_i = \frac{1}{y_i'(obs.)}$$

The R_{wp} with the background is calculated with **equation 1.4.3** and without with **equation 1.4.4**:

(1.4.3.)

$$R_{wp} = \frac{\sqrt{\sum_i w_i'\left(y_i'(obs.) - y_i'(clac.)\right)^2}}{\sqrt{\sum_i w_i'\left(y_i'(obs.)\right)^2}}$$

(1.4.4.)

$$R_{wp} = \frac{\sqrt{\sum_i w_i\left(y_i(obs.) - y_i(clac.)\right)^2}}{\sqrt{\sum_i w_i\left(y_i(obs.)\right)^2}}$$

An additional parameter is the expected profile R-factor (R_{exp}) (**equation 1.4.5**). This parameter specifies the possible limit for the R_{wp} using the statistics in the

nominators, where *n* is the number of steps and *m* is the number of refined parameters [57].

(1.4.5.)

$$R_{exp} = \frac{\sqrt{n-m}}{\sqrt{\sum_i w_i \left(y_i(obs.)\right)^2}}$$

Finally, the goodness of fit (GOF) is defined from the ratio between the R_{wp} and the R_{exp} (**equation 1.4.6**) [59].

(1.4.6.)

$$GOF^2 = \left(\frac{R_{wp}}{R_{exp}}\right)^2$$

1.5. Mie Scattering

When electromagnetic (EM) radiation is traveling through a medium containing small particles, several phenomena can occur [60]. For example, particles can convert part of the EM energy to heat (*absorption*), and part of it can be transmitted (*transmission*) without a loss. Another phenomenon is *elastic scattering*, where the light is scattered in all directions at the frequency of the incident beam. Accordingly, the polarization of the scattered beams diverges from the polarization of incident one. The total scattering depends on the arrangement of the particles' charges with respect to the scattered and incident directions. Thus, the charges forming the particle are treated as a macroscopic body with specific distribution of the refractive index. The energy of the incident beam that passes through a particle is reduced by the amount of the sum: *absorption* + *scattering*, and it is termed *extinction.* In addition, if the temperature of the particle is deviating from T = 0 ˚C, the particle emits radiation at all the frequencies and directions (*thermal emission*) [60].

The scattering mechanism by small particles can be described by two main theories [60,61]. Rayleigh scattering theory works best for particles that are much smaller than the wavelength (a (particle radius) << λ). As for the bigger particles ($a \leq \lambda$), the Mie theory is the appropriate one.

According to the Rayleigh scattering theory, a light that interacts with a particle is a plane electromagnetic wave. The spherical particle is assumed to be small under the restrictions of ($a << \lambda$) $x << 1$ and $|m|x << 1$, with particle and medium permittivity's ε_p and ε_m, respectively. Where x is a size parameter with formula $x = 2\pi N_m a/\lambda$, $N_m = n + ik$ is a complex refractive index of the medium, a is the particle radius, λ is the wavelength, and m is a relative refractive index $m = N_p$ (refractive index particle)/N_m [61].

The electrostatic approximation implies a uniform static electric field inside and near the particle, where the particle is getting polarized, and an electric dipole is induced. This dipole can oscillate and radiate (scatter) electromagnetic energy into the far-field. The absorption (Q_{abs}) and scattering (Q_{sct}) efficiencies can be described by **equations 1.5.1** and **1.5.2**.

(1.5.1.)

$$Q_{abs} = 4xIm\frac{\varepsilon_p - \varepsilon_m}{\varepsilon_p + 2\varepsilon_m} \propto \frac{1}{\lambda}$$

(1.5.2.)

$$Q_{sct} = \frac{8}{3}x^4\left|\frac{\varepsilon_p - \varepsilon_m}{\varepsilon_p + 2\varepsilon_m}\right|^2 \propto \frac{1}{\lambda^4}$$

In the Mie theory, the assumption is that a plane x-polarized wave incident a homogeneous isotropic sphere of a radius a ($a \leq \lambda$) [61]. The incident electric field is expanded in an infinite series of vector spherical harmonics. Similar expansion is applied on the scattered and inside the sphere electromagnetic field. The corresponding magnetic field is obtained from the curl. The form of expansions for the scattered and the inside sphere fields is dictated by the orthogonality of the vector harmonics, boundary conditions, and the form of expansion of the incident field. In the Mie theory, the scattered field is the

superposition of the normal modes, each weighted by the appropriate coefficient a_n or b_n. The natural frequencies of the sphere are complex, and the related modes are called virtual. Nevertheless, when the real part of these frequencies is bigger compared with the imaginary part, these frequencies can be related to as real frequencies of the EM waves at which the various EM modes of the sphere are excited. When the permeability of the particle is equal to the one of the media ($\mu_p = \mu_m$), the a_n and b_n coefficients can be described by the **equations 1.5.3** and **1.5.4** [61]:

(1.5.3.)

$$a_n = \frac{m\psi_n(mx)\psi_n'(x) - \psi_n(x)\psi_n'(mx)}{m\psi_n(mx)\xi_n'(x) - \xi_n(x)\psi_n'(mx)}$$

(1.5.4.)

$$b_n = \frac{\psi_n(mx)\psi_n'(x) - m\psi_n(x)\psi_n'(mx)}{\psi_n(mx)\xi_n'(x) - m\xi_n(x)\psi_n'(mx)}$$

Where the *Riccati-Bessel* functions are introduced (**Figure 1.5.1**):

$$\psi_n(\rho) = \rho j_n(\rho),\ \ \xi_n(\rho) = \rho h_n{}^{(1)}(\rho),\ \ \rho\ (dimensionless\ variable) = \mathrm{k}r$$

Where k is the wave vector, k = k' + ik" = $\omega N/c$, ω – is the angular frequency, N – is the complex refractive index, c – is the speed of light in a vacuum, and r is the radius of the imaginary sphere.

It is important to note that a_n and b_n vanish as m approaches unity. That is when the refractive index of the medium is similar to the one of the particle.

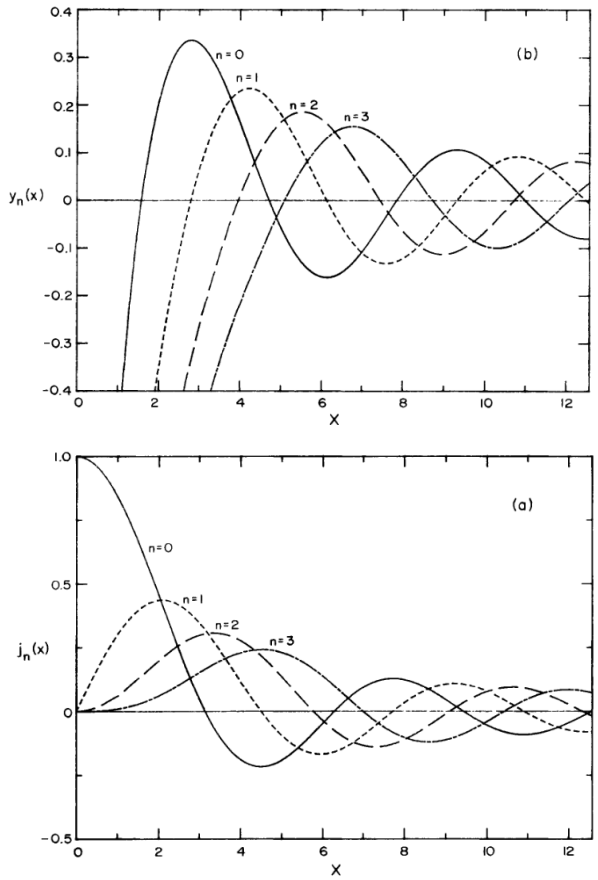

Figure 1.5.1. Spherical Bessel functions of the first (a) and second (b) kind [61].

The spherical Bessel function of the third kind can be described by **equation 1.5.5**.

(1.5.5.)

$$h_n^{(1)}(\rho) = j_n(\rho) + iy_n(\rho)$$

This **equation (1.5.5)** originated from a physical ground where the scattered field is an outgoing wave at a large distance from the particle (far-field). The $h_n^{(1)}$ function specifies the radial dependence for the vector spherical harmonics.

The larger the sphere, the more intense the forward scattering direction compared to the backscattered one (**Figure 1.5.2**).

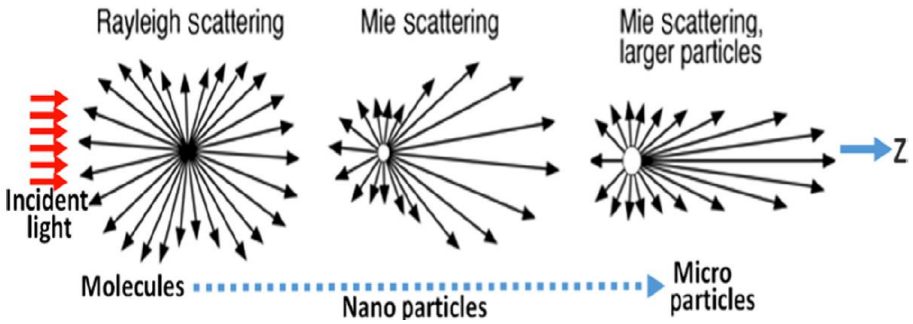

Figure 1.5.2. The angular distribution of Rayleigh scattering of light by molecules and Mie scattering by nanoparticles and microparticles [62].

When scattering coefficients (a_n and b_n) are known, the measurable quantities associated with the scattering and absorption (cross-sections and scattering matrix elements) can be determined. The net rate at which the electromagnetic energy is crossing the surface of an imaginary sphere is denoted as W_{abs}, $W_{abs} = W_{ext} - W_{sct}$, where *abs* is the absorption, *ext* – extinction, and *sct* – is the scattering. For the nonabsorbing surrounding medium, W_{abs} is independent of the radius of this imaginary sphere. To use the far-field approximation for the electromagnetic field the radius of the sphere has to be adequately large. The scattering and the extinction cross-sections are described by **equations 1.5.6** and **1.5.7**.

(1.5.6.)

$$C_{sct} = \frac{W_{sc}}{I_i} = \frac{2\pi}{\mathrm{k}^2}\sum_{n=1}^{\infty}(2n+1)(|a_n|^2 + |b_n|^2)$$

(1.5.7.)

$$C_{ext} = \frac{W_{ext}}{I_i} = \frac{2\pi}{\mathrm{k}^2}\sum_{n=1}^{\infty}(2n+1)Re\{a_n + b_n\}$$

Where k is the k-vector and I_i is the irradiance incident on the imaginary sphere.

The scattering and the extinction efficiencies can be derived from the relation $Q_{sct/ext} = C_{sct/ext}/\pi a^2$ and the absorption efficiency is $Q_{abs} = Q_{ext} - Q_{sct}$.

1.6. Random Lasers

Lasing materials have been always drawn attention. With a growing field of nanoscience and nanotechnology, nanoparticles with lasing properties have become an attractive topic. Laser stands for light amplification by stimulated emission of radiation. For a proper lasing action a population inversion is essential, where a major part of the luminescent ions (active medium) are excited [63]. When the ions are emitting in a coherent, monochromatic, and non-divergent way, the process is called stimulated emission. The working principle of the conventional and random lasers is illustrated in **Figure 1.6.1a**. The conventional laser is composed of an active medium, which is responsible for the amplification of electromagnetic (EM) radiation. The pump system is accountable for the population inversion, and the laser resonator (2 parallel mirrors) can store a coherent EM field. In addition, laser resonators enable the EM field to interact with the active medium [64].

Earlier, light scattering was considered to be harmful to laser action. The main reason is the removal of the photons from the lasing modes of a conventional laser resonator. Nevertheless, in a strongly scattering active medium, light scatterings play an important role; (1) multiple scattering increases the time light is traveling in the active medium, thus enhancing light amplification by stimulated emission; (2) multiple light scattering leading to coherent feedback (**Figures 1.6.1b** and **1.6.1c**) [65]. An essential condition for the random laser's proper operation is a sufficient amplification of light (to balance the loss) before it leaves the system (active medium). Thus, the scattering mean free path (l_s)

must be equal or greater than gain (active) length (l_g). The l_g is defined as a path length over which the intensity is amplified by a factor of e [66]. There are two types of random lasers, the first presents incoherent (non-resonant) feedback (single spectral peak) (**Figures 1.6.1b** and **1.6.1c**). In the first case, the spontaneously emitted photons undergo multiple scattering before exiting the system. In the course of the photon travel in the active medium, additional photons are generated through stimulated emissions and the EM radiation is being amplified [66]. The second type of random laser displays coherent (resonant) feedback (several laser-like spectral lines). In this type of random laser $l_s \leq \lambda$ (wavelength), as a result, light can return to a scatter from which it was scattered, and a closed-loop is formed. Consequently, laser oscillations might occur, and the loop acts as a laser resonator [67] (**Figure 1.6.1b**). Coherent feedback (**Figure 1.6.1c**) is observed in ZnO NP's deposited on ITO-coated substrate [68] or pellet [65]. In this case, ZnO NP's are scatterers and active media at the same time. Incoherent feedback was presented in lanthanides doped powders [69] and dye solution (active medium) with nanoparticles like TiO_2 as scattered centers [70].

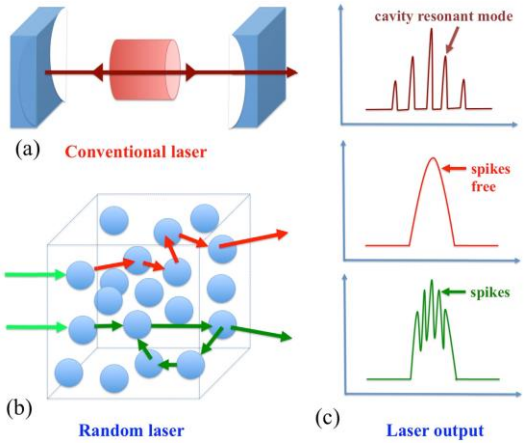

Figure 1.6.1. Working principle of lasing in traditional cavity and random media. (a) conventional laser cavity; (b) random laser cavity illustrating the incoherent feedback (red arrows) and coherent feedback (green arrows); (c) illustration of spectral outputs of a conventional laser and a random laser, where the spikes free correspond to incoherent feedback, whereas the coherent feedback is recognized by its spiky signature [66].

Recently, lasing properties have been addressed to the nanoparticles such as gold [71] and silver [72] supporting surface Plasmon. Due to the interaction of the free conduction electrons in the metal with the electromagnetic radiation, the free electrons collectively oscillate at the resonance frequency [73]. These oscillations are called surface Plasmon (SP). Materials with negative real and small positive imaginary dielectric constant can support a surface Plasmon resonance (SPR) [74]. In spherical subwavelength NP's, it is termed localized surface Plasmon resonance (LSPR) (**Figure 1.6.2**).

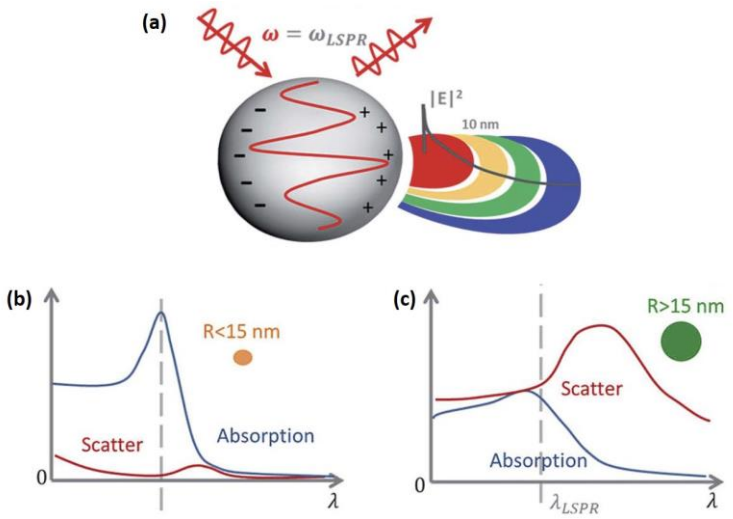

Figure 1.6.2. Localized surface Plasmon resonance (LSPR) exists when the metal nanoparticle (NP) is smaller than the incident wavelength, making the electron oscillations in phase. (a) The collective oscillations lead to a large absorption and scattering cross-section, as well as an amplified local EM field. For small particles less than (b) R < 15 nm, absorption dominates and the absorption cross-section is large. For bigger nanoparticles greater than (c) R > 15 nm, the scattering cross-section dominates [75].

It is shown in the literature that by the proper transfer of energy between the metal NP's (gold or silver) and fluorophore, the fluorescence processes are enhanced (**Figure 1.6.3**) [75]. After the excitation of the LSPR in metal NP's, the energy is stored as an intense local EM field. In the case of small NP's (< 15 nm), this energy will mainly convert to heat and eventually will be absorbed by the particle (**Figure 1.6.2b**). The bigger particles (> 15 nm) will mainly scatter the light back into the far-field (**Figure 1.6.2c**). The energy transfers between NP's Plasmon and the fluorophore are dominated by the dipole-dipole interactions. When the distance between the plasmonic NP's and the fluorophore is 1–10 nm, the non-radiative local field of one dipole can excite the second one (known as FRET- Förster resonance energy transfer). When the radiative dipole is placed in a resonant cavity, the emission intensity will be enhanced on-resonance and quenched off-resonance when compared to free space (Purcell effect). This process is justified by the modification of the local density of optical states by the cavity. The spectral overlap between the Plasmon and the fluorophore is needed for the proper energy transfer by the Purcell effect or FRET mechanisms (**Figure 1.6.3**). When Plasmon resonance overlaps with the fluorophore's absorption, the excitation rate of the fluorophore will be enhanced from its free space value (**Figure 1.6.3a**). If the Plasmon resonance is overlaps with the fluorophore emission, an enhancement or quenching of the emission intensity is possible (**Figure 1.6.3b**). For metal nanoparticles dominated by absorption mechanism (< 15 nm) at a distance less than ~10 nm from the fluorophore, the Plasmon has to overlap with the excitation band of the fluorophore to avoid emission quenching. If mainly scattering NP's are used, the Plasmon should overlap with both the absorption and the emission at a distance about ~10 – 30 nm from the fluorophore for the maximum fluorescence enhancement [75].

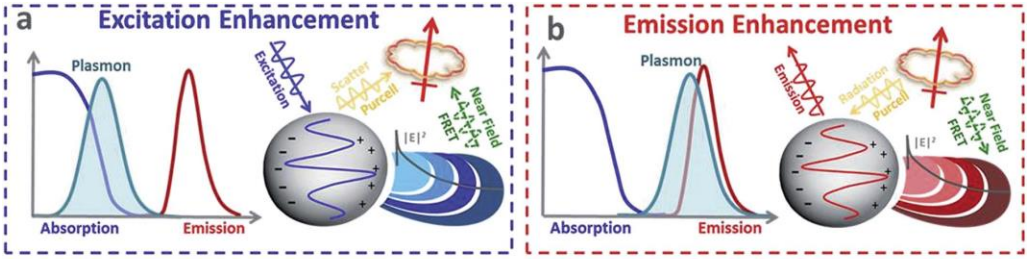

Figure 1.6.3. Dependence on distance and sphere radius of Plasmon-enhanced fluorescence. (a) If the Plasmon overlaps with the absorption of the fluorophore, an excitation enhancement is possible through the near field and FRET or scattering. (b) If the Plasmon overlaps with the emission of the fluorophore, an emission enhancement is possible through the Purcell effect or FRET [75].

2. Experimental Section

2.1. Materials

Gadolinium(III) nitrate hexahydrate ($Gd(NO_3)_3 \cdot 6H_2O$, 99.9%), Thulium(III) chloride hexahydrate ($TmCl_3 \cdot 6H_2O$, 99.9%), Neodymium(III) chloride hexahydrate ($NdCl_3 \cdot 6H_2O$, 99.9%), Niobium(V) chloride ($NbCl_5$, 99%), potassium hydroxide (KOH, ≥ 85%), and poly(methyl methacrylate) $[(CH_2C(CH_3)(CO_2CH_3)]_n$, Mw ~ 120,000) are purchased from Sigma-Aldrich.

2.2. Synthesis

The $GdNb_2O_6$ and $GdNb_2O_6/GdNbO_4$ submicron morphologies are synthesized *via* the hydrothermal method (**Figure 2.2.1**). First, $Gd(NO_3)_3 \cdot 6H_2O$ (0.504 g) is dissolved in deionized water (DI, 18 MΩ·cm^{-1}, 20 mL). The $NbCl_5$ (0.308 g) fine powder is added to 75 mL DI and sonicated (about 15 min) until a turbid colloidal suspension is obtained. For the basic solution, KOH pellets (4.43 g) are dissolved in 50 mL DI. The $Gd(NO_3)_3 \cdot 6H_2O$ and $NbCl_5$ solutions are mixed (pH ≈ 1) and transferred to a hot plate magnetic stirrer (IKA® C-MAG HS-7, 100 – 1500 rpm speed) for a constant stirring (the stirring velocity is set to 2). Then, 2.8 mL of the KOH solution is instantly added to the $Gd(NO_3)_3/NbCl_5$ mixture, while the rest of the KOH solution is added slowly to adjust the pH (**Table 2.2.1**). A gel-like precipitate is formed after the KOH addition (precursor solution). The final pH of the precursor solution is 6.53 ± 0.03, 7.21 ± 0.09, 7.93 ± 0.05 for the bar-, cube-, and flower-like morphologies, respectively (they will also be referred to as bars, cubes, and flowers, respectively). The temperature of the mixture is constantly monitored during the KOH addition (**Table 2.2.1**). Finally, the precursor solution is transferred to a Teflon vessel (volume 150 mL) (**Figure 2.2.1a**) and further sealed into the stainless steel chamber (**Figure 2.2.1b**). The synthesis is carried out at 160 ˚C for 24 h (**Figure 2.2.2a**). The

resulting white precipitate is washed and centrifuged (5000 rpm) three times with DI, and then dried at 75 ˚C for 1.5 h. Similar experimental procedure is applied for preparation of $GdNb_2O_6$ with different content of thulium Tm^{3+} ($Gd_{1-x}Tm_xNb_2O_6$) (**Table 2.2.2**) and neodymium Nd^{3+} ($Gd_{1-x}Nd_xNb_2O_6$) (**Table 2.2.3**).

All the thermal treatments are conducted in a closed system with a nitrogen (N_2) atmosphere (**Figure 2.2.2b**). For the proper elimination of water three-step thermal treatments are performed: (1) 120 ˚C – 3h, (2) 200 ˚C – 2h, and (3) T = 250, 400, 500, 600, 700 and 800 ˚C for 16 h.

Figure 2.2.1. The hydrothermal system used in the experiment (a) Teflon vessel and (b) Stainless Steel chamber.

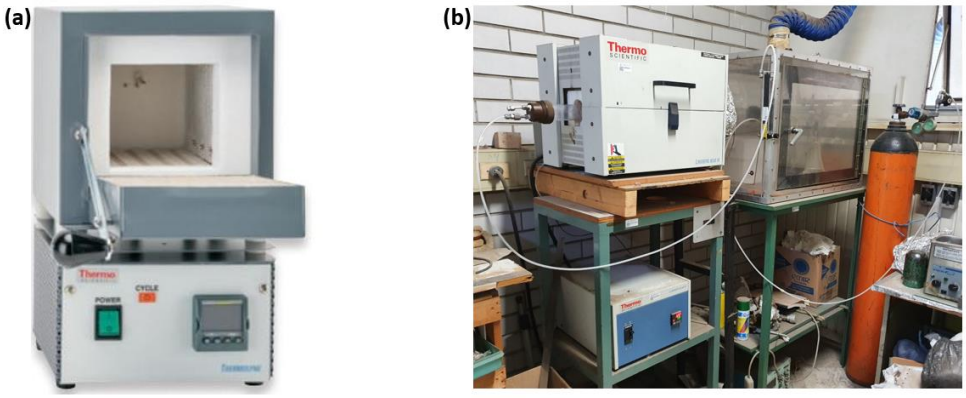

Figure 2.2.2. (a) Oven of the brand Thermo scientific used to heat the hydrothermal system, (b) system for the powders annealing in the nitrogen atmosphere.

Table 2.2.1. The pH and temperature of the precursors' solution, and the KOH solution (C = 1.34 M) volume (V) are added at the rate of μL/min to obtain the various morphologies.

Morphology	**pH**	**T [˚C]**	**V [μL] 50 μL/2 min**	**V [μL] 10 μL/2 min**	**V [μL] 10 μL/3 min**
Bars	6.53 ± 0.03	16.5 – 17.5	300	50	90 – 110
Cubes	7.26 ± 0.07	18.0 – 19.0	300	70	180 – 190
Flowers	7.93 ± 0.05	18.0 – 19.0	500	180	210 – 220

Table 2.2.2. The moles (n) number and weight (m) of $Gd(NO_3)_3 \cdot 6H_2O$ and $TmCl_3 \cdot 6H_2O$ are used for the preparation of $Gd_{1-x}Tm_xNb_2O_6$ compounds with different content of Tm^{3+}.

$Gd_{1-x}Tm_xNb_2O_6$	**n (mol) $Gd(NO_3)_3$**	**m (g) $Gd(NO_3)_3$**	**n (mol) $TmCl_3$**	**m (g) $TmCl_3$**
x = 0.01	$11.06 \cdot 10^{-4}$	0.499	$11.17 \cdot 10^{-6}$	0.004
x = 0.02	$10.94 \cdot 10^{-4}$	0.494	$22.33 \cdot 10^{-6}$	0.009
x = 0.03	$10.83 \cdot 10^{-4}$	0.489	$33.50 \cdot 10^{-6}$	0.013
x = 0.04	$10.72 \cdot 10^{-4}$	0.484	$44.67 \cdot 10^{-6}$	0.017

Table 2.2.3. The moles (n) number and weight (m) of $Gd(NO_3)_3 \cdot 6H_2O$ and $NdCl_3 \cdot 6H_2O$ are used for the preparation of $Gd_{1-x}Nd_xNb_2O_6$ compounds with different content of Nd^{3+}.

$Gd_{1-x}Nd_xNb_2O_6$	n (mol) $Gd(NO_3)_3$	m (g) $Gd(NO_3)_3$	n (mol) $NdCl_3$	m (g) $NdCl_3$
x = 0.01	$11.06 \cdot 10^{-4}$	0.499	$11.17 \cdot 10^{-6}$	0.004
x = 0.02	$10.94 \cdot 10^{-4}$	0.494	$22.33 \cdot 10^{-6}$	0.008
x = 0.03	$10.83 \cdot 10^{-4}$	0.489	$33.50 \cdot 10^{-6}$	0.012
x = 0.04	$10.72 \cdot 10^{-4}$	0.484	$44.67 \cdot 10^{-6}$	0.016

2.3. Calculations (Mie theory)

Wolfram Mathematica 12.1.1 is used to compute the absolute absorbance and extinction for a homogeneous sphere by Mie theory. As a starting point, code provided by Sarid and Challener in Ch. 9 [76] is used. This code is originally developed by Bohren and Huffman in Appendix A [61]. The real part of the refractive index is approximated with data for potassium niobate ($KNbO_3$), available at refractiveindex.info database [77]. The imaginary part of the refractive index (extinction coefficient *k*) is obtained from **equations 2.3.1-2.3.3** [78] using the absolute absorbance (Q_{abs}) measured for powder samples in the air between 250-380 nm:

(2.3.1.)

$$OD = \log_{10}\left(\frac{1}{1 - Q_{abs}}\right) \rightarrow$$

(2.3.2.)

$$\alpha = \frac{2.303 \cdot (OD)}{x} \rightarrow$$

(2.3.3.)

$$k = \frac{\alpha \cdot \lambda}{4\pi}$$

where α is the absorption coefficient, *OD* is the optical density, and *x* is the sample thickness (0.2 cm in the current case). Further on, the absorption coefficient (Q_{abs}) is fitted with one Gaussian function, and it is used to calculate the extinction spectra (Q_{ext}). The Q_{ext} is calculated in two ways: (1) using Mie theory with weight functions from the particle size distribution (~ 300 particles) measured from SEM images (Mie-Measured Size) and (2) by fitting experimentally measured Q_{ext} (240-1100 nm range) using Mie theory particle size distribution of two Gaussian functions (Mie-2-Gaussian). For the measured size distribution, the size of the bar-like particles is approximated with two equally-weighted dimensions called length and width (**Figure 2.3.1a**). The dimensions of the cube-like morphology are approximated with three equally-weighted dimensions: length, width, and diagonal (**Figure 2.3.1b**). For the fitting (Mie-2-Gaussian), the Mie extinction spectra are first calculated for 490 spheres of diameters 20 to 1000 nm. Then the minimum square fit of the experimentally measured Q_{ext} is done using a two Gaussian weighted size distribution.

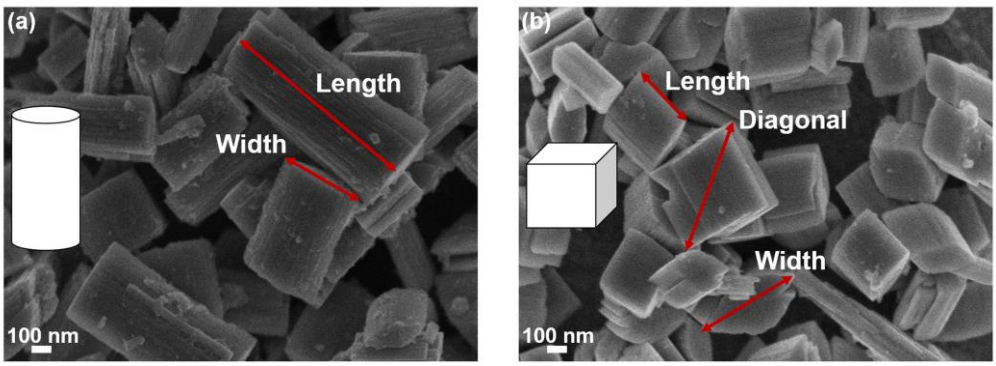

Figure 2.3.1. SEM images with measured particles dimensions of (a) bars and (b) cubes.

It assumed that the orientation of the particles in the solution is random. Therefore, all the dimensions above have to be considered in the sizes distribution. The bar- and cube-like morphologies are approximated as cylinders and cubes, respectively (**Figure 2.3.1**).

To calculate the refractive index, **equation 2.3.4** is used. This equation is proposed by Herve and Vandamme [79,80].

(2.3.4.)

$$n = \sqrt{1 + \left(\frac{A}{E_g + B}\right)^2}$$

Where E_g is the material band gap, A is the constant of value 13.6 eV, which corresponds to the hydrogen ionization energy, and B is equal to 3.4 eV.

2.4. Preparation of PMMA Films

To prepare the poly(methyl methacrylate) (PMMA) films, 0.009 g of $Gd_{1-x}Nd_xNb_2O_6$ powder (cube-like morphology) are first dispersed in chloroform by 15 min sonication. Then 1.0 g of PMMA is added to the solution. The chloroform solution with the $Gd_{1-x}Nd_xNb_2O_6$ powder and PMMA is sonicated for about 40 min, followed by manual agitation every 10 min until the polymer completely dissolves. Next, the formed solution is drop-cast into polypropylene ice molds and dries in the laminar flow cabinet overnight. Finally, the PMMA films are ejected from the molds and analyzed.

2.5. Characterization

2.5.1. Electron Microscopy and Energy-Dispersive X-Ray Spectroscopy

The transmission electron microscopy (TEM) is done using JEM-ARM200F, operated at the accelerated voltage of 200 kV. Scanning electron microscopy (SEM) is performed with JEOL JSM-7401F, using a secondary electrons (SEI) detector. The accelerated voltage and the working distance are 3.5 – 4.5 kV and 3 mm, respectively. SEM is equipped with Thermo Scientific™ Noran System SIX Energy-dispersive X-ray spectrometer (EDS). EDS is done with an accelerated voltage of 20 kV. Particles dimensions are measured with ImageJ [81].

2.5.2. X-Ray Diffraction

X-ray Diffraction (XRD) is measured using D8 ADVANCE Eco, BRUKER diffractometer. The pattern is recorded using a 1-D LYNXEYE detector. The diffractometer is equipped with a Cu anode (CuKα radiation with 1.5418 Å wavelength), operated at 40 kV, 25 mA. The 2-theta scans are performed in the Bragg-Brentano mode in the interval 9.5 – 100 degrees, with step size and a scan speed of 0.015 degrees and 8 s/step, respectively.

2.5.3. Rietveld Analysis

The crystalline structure is first analyzed using Fox Wiki [82] software. This software is based on the ab-initio crystal structure solution from diffraction data. X-ray diffractograms of the bar- and cube-like morphologies are used for the analysis. The obtained lattice parameters (a = 11.1539, b = 7.4940, and c = 5.2690 Å) and the space group (*Pnma* (62)) are used to simulate a perfect

$GdNb_2O_6$ structure using HighScore Plus (HSP) [83] software. The Gd^{3+} and Nb^{5+} ions are used for the simulation. Atoms coordinates of the $EuTiNbO_6$ structure are used as a template to simulate the $GdNb_2O_6$ structure (SpringerMaterials database) [84]. Finally, the lattice parameters are refined with Rietveld analysis incorporated in HSP [85].

2.5.4. Raman

Raman analysis is done using i-Raman Plus (BWTEK) spectrometer BWS465 – 785H, resolution < 3.5 cm^{-1}@912 nm. It is equipped with a 785 nm excitation laser, exiting probe is 340 mW, at the laser point 455 mW.

2.5.5. Fourier-Transform Infrared Spectroscopy

Fourier-transform infrared spectroscopy (FTIR) spectra are acquired using Varian 640-IR spectrometer by Agilent Technologies. The samples are measured with a resolution of 4 cm^{-1} and 20 scans per sample. The measurements are standardized with a KBr pellet, dried at 150 ˚C for 24 h.

2.5.6. X-Ray Photoelectron Spectroscopy

X-ray photoelectron spectroscopy (XPS) measurements are done with the ESCALABTM 250Xi, Thermo ScientificTM. The equipment is equipped with the monochromatic Al K Alpha X-ray gun source. The spot size, energy step size, and pass energy are 650 μm, 0.1 eV, and 20 eV, respectively. Peaks deconvolution is performed with Fityk [86] software.

2.5.7. Photoluminescence and Absolute Reflectance

The absolute reflectance and photoluminescence (PL) of the powders are measured using EDINBURGH INSTRUMENTS FLS980 spectrometer equipped with an integrated sphere. For the absolute reflectance, each spectrum is averaged over four measurements, and the excitation and emission beam slits are 10 and 0.4, accordingly. The step and the dwell time are 0.1 nm and 0.25 s, respectively. For the PL measurements, the excitation and emission beam slits are 3.0 and 1.0 for the undoped and Tm^{3+} doped materials and 10.0 and 1.0 for the Nd^{3+} doped materials. The step and dwell time are 1.0 nm and 0.1 s, correspondingly.

2.5.8. UV-Vis

The UV-vis extinction spectra are taken in the absorbance mode with Perkin Elmer Lambda 12 spectrometer, in the 200 – 1100 nm range with a step interval of 1 nm. For this analysis, the powders are dispersed in the solvent by sonication for about 5 min. To analyze the effect of the refractive index on the position of the Mie scattering peak, the powders are dispersed in water, tetraethyl orthosilicate (TEOS), chloroform, and 1,2-dichlorobenzene, with the refractive index of 1.3330, 1.3830, 1.4458, and 1.5514, respectively.

3. Results and Discussion

3.1. Intrinsic Material Synthesis and Characterization

3.1.1. Morphology

The synthesized gadolinium niobate morphologies are presented in **Figure 3.1.1.1**. The particles with bar- and cube-like morphologies are formed by slab-like crystallites placed on top of each other (**Figures 3.1.1.1a, 3.1.1.1b,** and **3.1.1.1c, 3.1.1.1d,** respectively). The flower-like particles appear as petal-like polycrystalline layers (**Figures 3.1.1.1e** and **3.1.1.1f**). All three morphologies are polycrystalline with measured crystallite width of 121.2 ± 60.1, 140.8 ± 53.5, and 18.6 ± 6.9 nm for the bars, cubes, and flowers, respectively. These results are supported by a Rietveld analysis for bars and cubes (**Table 3.1.5.1**).

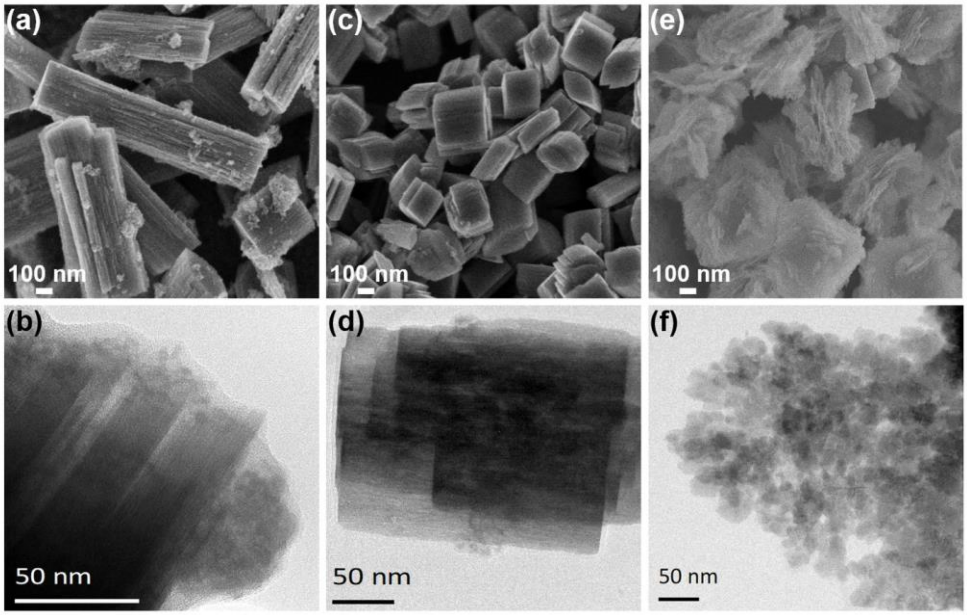

Figure 3.1.1.1. SEM and TEM micrographs of the (a), (b) bar- (c), (d) cube-, and (e), (f) flower-like morphologies, respectively.

Table 3.1.1.1. Dimensions of the various morphologies measured from SEM and TEM images, length (l), width (w), and thickness (t).

Morphology	l [nm]	w [nm]	t [nm]
Bars	784 ± 186	328 ± 73	189 ± 32
Cubes	246 ± 70	237 ± 47	190 ± 47
Flowers	543 ± 78	---	---

3.1.2. Morphology with Wide Temperature Range

Synthesis conditions, such as precursors' solution pH and temperature during the KOH addition (T_{KOH}), and the rate of the KOH addition, are crucial for successful synthesis. Small shifts from these conditions (**Table 2.2.1**) result in a different pH value and cause changes in the morphology and quality of the material. In addition, a temperature variation during the KOH addition affects the control over the morphology (**Figure 3.1.2.1**). To control the synthesis better, T_{KOH} is kept within a narrow range of 1 ˚C (**Table 2.2.1**), and the morphology (**Figure 3.1.1.1**) is controlled solely by pH. Surfactant is not necessary at any stage of the synthesis.

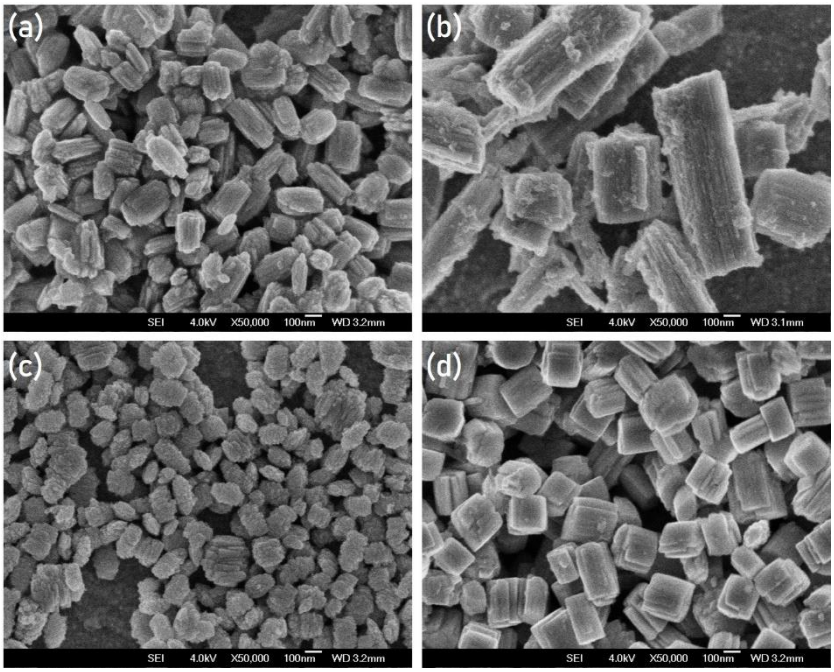

Figure 3.1.2.1. Morphology of $GdNb_2O_6$ synthetized at various temperature ranges during the KOH addition (a) T = 12.0 – 16.0 ˚C (pH = 6.50 ± 0.07), (b) T = 12.0 – 16.5 ˚C (pH = 6.48 ± 0.07), (c) T = 13.5 – 19.8 ˚C (pH = 6.84 ± 0.04), and (d) T = 12.0 – 19.0 ˚C (pH = 6.81 ± 0.1).

3.1.3. Morphology Evolution with pH

Figure 3.1.3.1 demonstrates the morphology evolution with increased pH values for the precursors' solution temperature of 18.0 – 19.0 ˚C. For the pH 6.78 ± 0.10 (**Figure 3.1.3.1a**), it is possible to observe a significant amount of small particles (residues) that did not adopt any specific morphology. At slightly higher pH values (7.04 ± 0.03, **Figure 3.1.3.1b**), short bars with some cubes are formed. Only cubes are present at the pH values 7.15 ± 0.07 and 7.28 ± 0.04 (**Figures 3.1.3.1c** and **3.1.3.1d**). At the pH values 7.64 ± 0.13 (**Figure 3.1.3.1e**), it is possible to see that the cube-like morphology has more opened layers. Also, some flowers are present at these pH values. When the pH reaches values of 7.93 ± 0.05, the morphology becomes flower-like (**Figure 3.1.3.1f**).

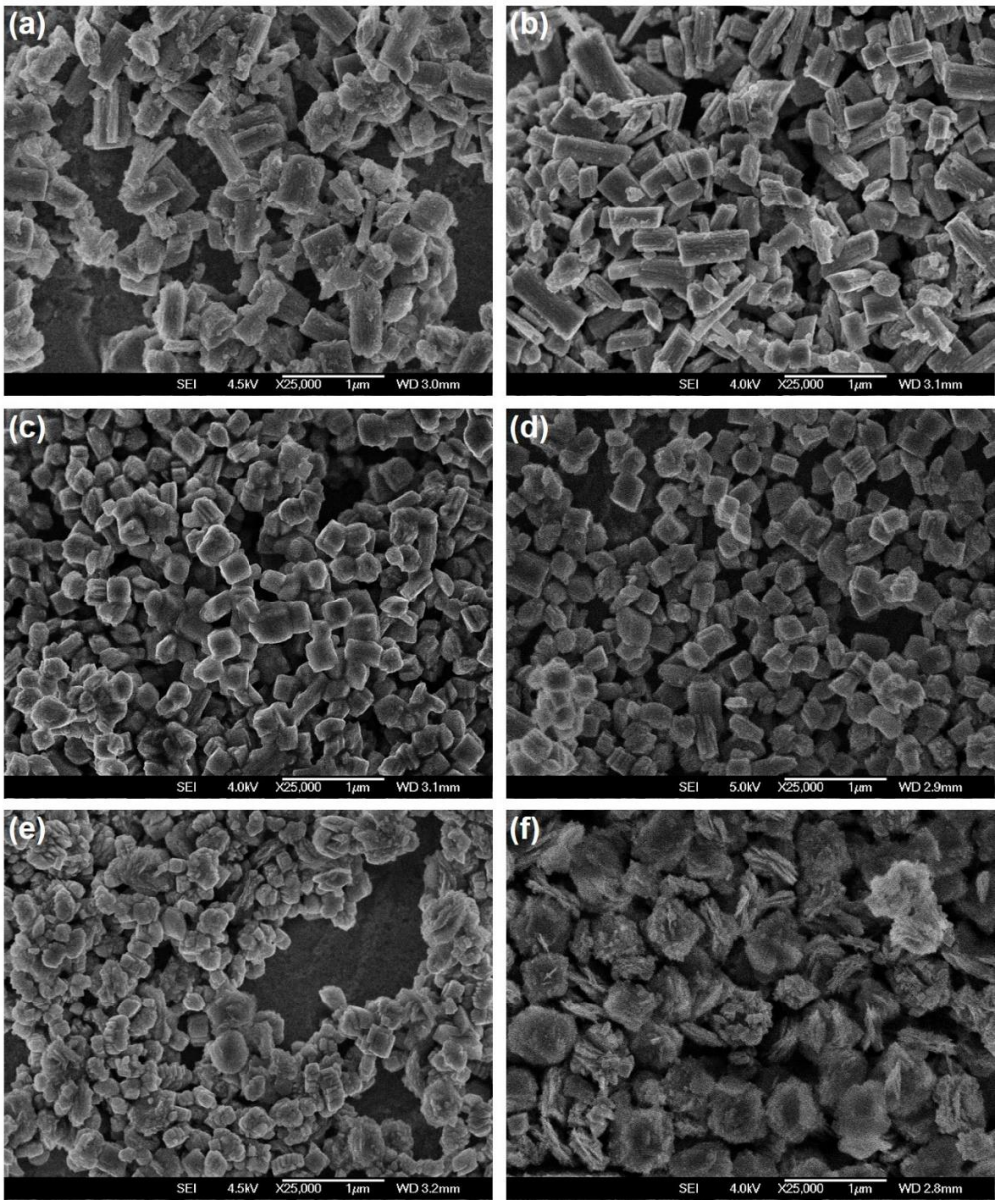

Figure 3.1.3.1. Morphology at the precursors' solution temperature of 18.0 – 19.0 ˚C and pH values (a) 6.78 ± 0.10, (b) 7.04 ± 0.03, (c) 7.15 ± 0.07, (d) 7.28 ± 0.04, (e) 7.64 ± 0.13 and (f) 7.93 ± 0.05.

3.1.4. Nucleation Mechanism

Crystallites nucleation mechanism can be partially understood from **Figure 3.1.4.1**. All three morphologies start the growth from a supersaturated solution (where the rate of nucleation is higher than the growth rate) [87–90]. The

nucleation starts at the source and grows away, ensuring continuous contact with the nutritious solution. Alkalinity (increased with KOH concentration) is the main factor for the bars and cubes aspect ratio (length/width) [91,92]. A cube-like morphology tends to form for a higher KOH concentration. The flower-like morphology can be related to the nucleation mechanism of the barite roses [87], where a radial habit of growth is adopted. In this case, the growth along the edges is simultaneous with the growth of the corners.

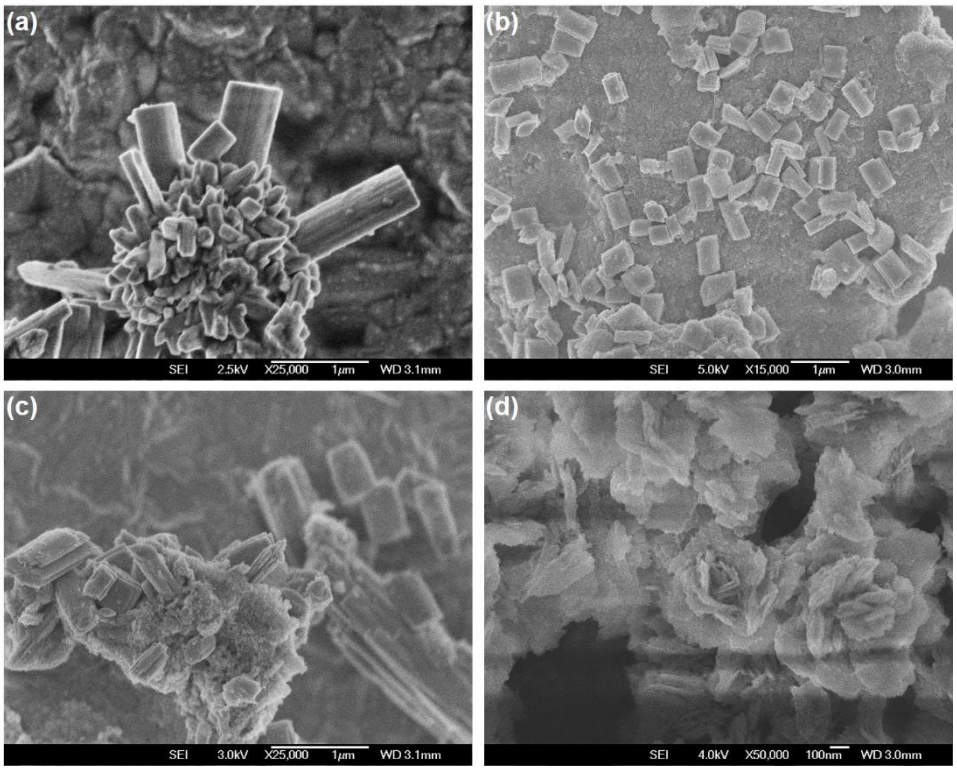

Figure 3.1.4.1. The $GdNb_2O_6$ nanomaterials in the process of growth (a) bar-, (b) cube-, (c) bar- and cube-, and (d) flower-like morphologies.

3.1.5. XRD and Rietveld Analysis

A good fit is found between the simulated XRD pattern for the perfect $GdNb_2O_6$ crystalline structure and the measured diffractograms for the bars and cubes (**Figure 3.1.5.1**). All peaks are present, and peaks due to contamination are not observed. The low values of R-factor (R_p), weighted residual R-factor (R_{wp}), and the goodness of fit (GOF) (**Table 3.1.5.1**) confirm the good fit between the calculated and experimental XRD data [57,58] and validate the crystallographic model. Hence, $GdNb_2O_6$ and $EuTiNbO_6$ [84] are isostructural with orthorhombic crystal structure and a *Pnma* (62) space group. For the flower-like morphology, additional peaks related to the $GdNbO_4$ crystalline structure are observed (**Figure 3.1.5.1**), suggesting a mixed $GdNb_2O_6/GdNbO_4$ phase. The refined lattice parameters for the bar-like morphology are, a = 11.1939(4), b = 7.5212(2), and c = 5.2903(1) Å, whereas for the cube-like morphology they slightly deviate, a = 11.2060(4), b = 7.5212(2), and c = 5.2864(2) Å. This shift in the lattice parameters is explained by the surface strain caused by the morphology effect [93], surface excess charge, and the adsorbed water and OH^- groups [94,95]. Due to the low-quality diffractogram and not properly defined peaks for the flower-like morphology, it is not possible to perform a Rietveld analysis.

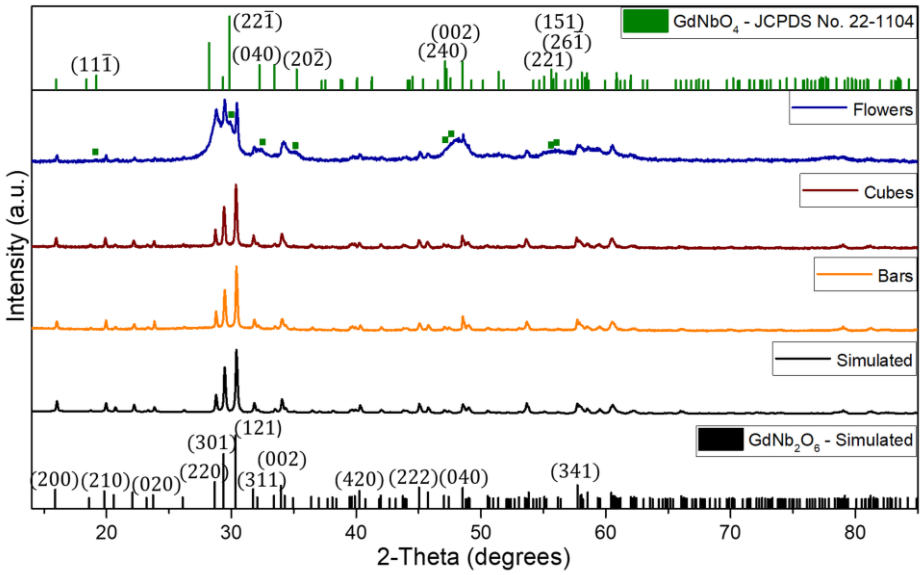

Figure 3.1.5.1. (a) XRD patterns; simulated (black) and experimental of bars (orange), cubes (wine), and flowers (blue).

Table 3.1.5.1. R_p, R_{wp}, GOF, and L (crystallite size) obtained from the Rietveld analysis using HighScore Plus (HSP) [83] and experimental average crystallite width (L_{avg}) measured from SEM and TEM images.

Morphology	**R_p [%]**	**R_{wp} [%]**	**GOF [%]**	**L [nm]**	**L_{avg} [nm] Experimental**
Bars	2.13	2.96	2.51	102	121.2 ± 60.1
Cubes	3.01	3.90	1.24	115	140.8 ± 53.5
Flowers	---	---	---	---	18.6 ± 6.9

Table 3.1.5.2. Micro-strains ε_{hkl} obtained by HSP for the lattice parameters *a*, *b*, *c*.

Morphology	***a* ε_{200} [%]**	***b* ε_{020} [%]**	***c* ε_{002} [%]**
Bars	0.304	0.342	0.104
Cubes	0.271	0.352	0.186

In the case of bars, thermally treated in three steps; (1) 120 ˚C – 3h, (2) 200 ˚C – 2h, and (3) T = 400, 600 and 700 ˚C, no structural changes are observed even after long annealing times (16 h) up to 600 ˚C (**Figure 3.1.5.2**).

The XRD patterns (**Figure 3.1.5.2**) are measured with SIEMENS D5000 (different equipment from the one used for the diffractograms for the refinement). The equipment operates at 40 kV, 25 mA. The step size and the scan speed are 0.02 degrees and 10 s/step, respectively. For the measurement, the powder is compressed into a pellet. Thus, a preferred orientation is induced along the (002) crystallographic plane (**Figure 3.1.5.2**).

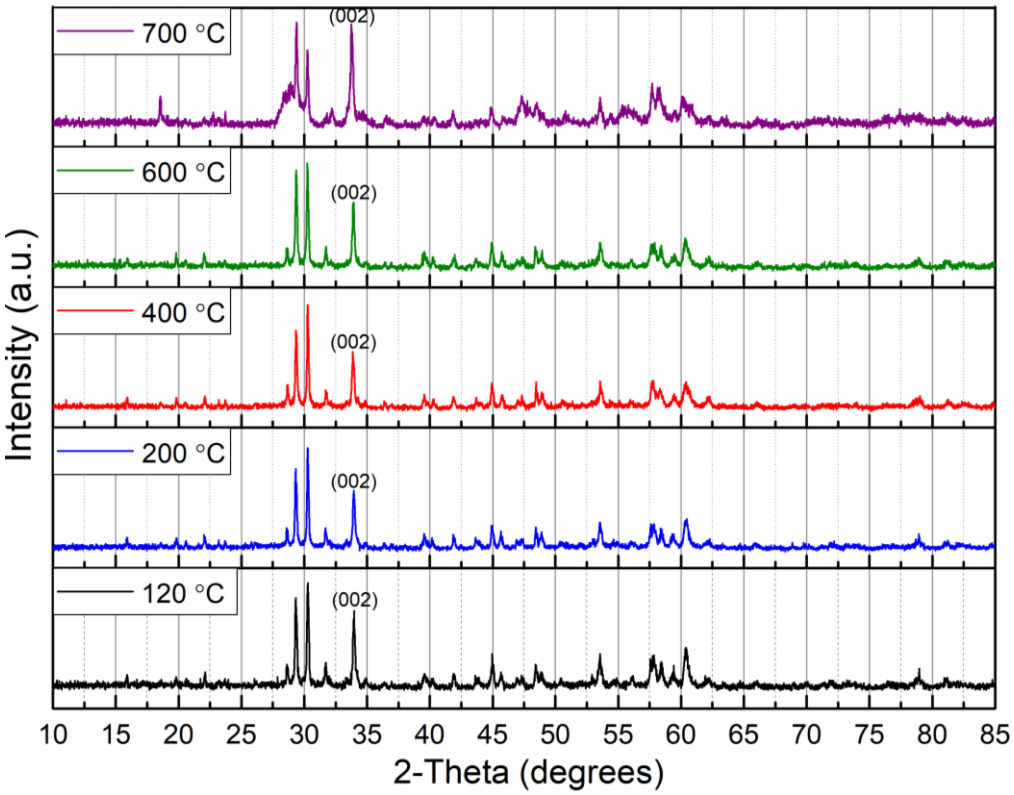

Figure 3.1.5.2. XRD patterns of the bar-like morphology annealed at 200 ˚C, 400 ˚C, 600 ˚C, and 700 ˚C for 16 h. All the samples were first annealed at 120 ˚C for 3 h. For the samples that were annealed at temperatures ≥ 400 ˚C, the samples were also thermally treated at 200 ˚C for 2 h. For the diffractogram of 120 ˚C the sample was annealed for 5 h at that temperature.

3.1.6. EDS

The representative EDS measurements for bars, cubes, and flowers are shown in **Figures 3.1.6.1**, **3.1.6.2**, and **3.1.6.3** and **Tables 3.1.6.1**, **3.1.6.2**, and **3.1.6.3**, accordingly. Average values from four measurements are presented in **Table 3.1.6.4**.

Two types of samples are analyzed; (1) thermally treated at 100 ˚C for 15 min (2) annealed in three steps; first at 120 ˚C – 3 h, then at 200 ˚C – 2 h, and finally at 250 ˚C – 16 h (to ensure a significant water elimination). The EDS analysis of the nanoscale $GdNb_2O_6$ shows that even though a 1:1 Nb:Gd mol ratio is added for the synthesis, the ratio is closer to 2:1 atomic percent (at. %) for bars and cubes (**Table 3.1.6.4**). Accordingly, the $GdNb_2O_6$ structure is favored for the synthesis conditions (**Table 2.2.1**) of these morphologies. For the flowers, the Nb:Gd at. % ratio is ~1.3:1 (**Table 3.1.6.4**), confirming the XRD data. Hence, $GdNb_2O_6/GdNbO_4$ mixed structure is formed. An increased amount of oxygen excess is observed with the change in the morphology (flowers > cubes > bars). This result might be related to the amount of OH^- groups and water molecules attached to the surface due to the increased surface area. Thus, the flower-like morphology contains the highest amount of water molecules attached to its surface. According to the EDS analysis, after the thermal treatment at 250 ˚C, only a slight reduction in oxygen content is observed for the bars, and the reduction is more significant for the cubes and flowers (**Table 3.1.6.4**).

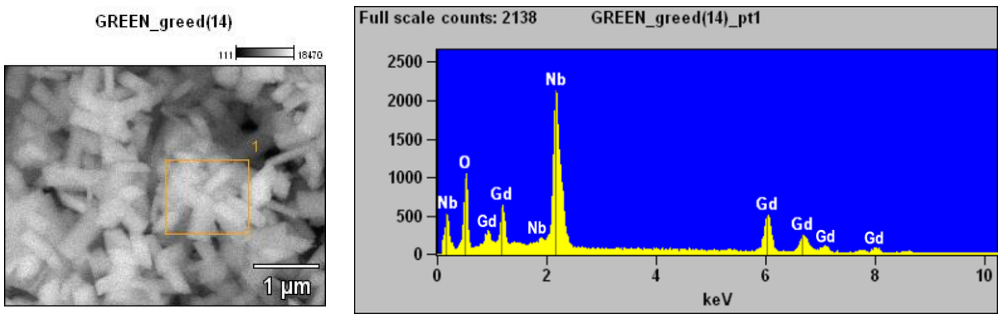

Figure 3.1.6.1. SEM image of the measured area and representative EDS spectra of bar-like morphology.

Table 3.1.6.1. EDS analysis of the bar-like morphology after three-step annealing at 120 ˚C (3 h), 200 ˚C (2 h), and 250 ˚C (16 h).

Element Line	ZAF Compnd	Element wt. % ± error	Element at. % ± error
O K	4.385	36.80 ± 0.39	80.55 ± 0.85
Nb L	1.437	34.82 ± 0.31	13.12 ± 0.12
Gd L	1.210	28.38 ± 0.71	6.32 ± 0.16
Total		100	100

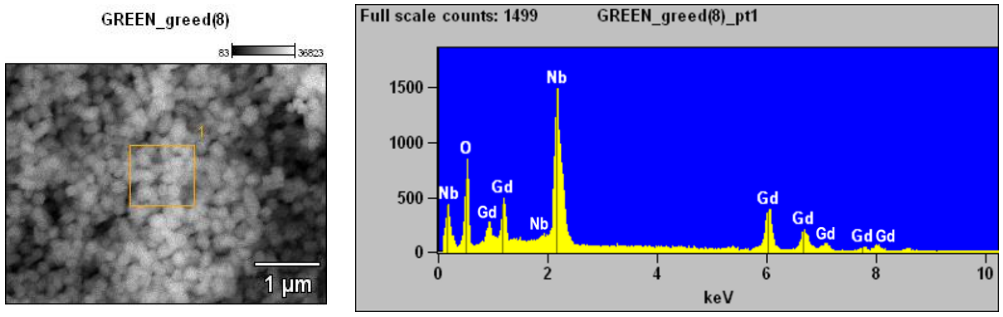

Figure 3.1.6.2. SEM image of the measured area and representative EDS spectra of cube-like morphology.

Table 3.1.6.2. EDS analysis of the cube-like morphology after three-step annealing at 120 ˚C (3 h), 200 ˚C (2 h), and 250 ˚C (16 h).

Element Line	ZAF Compnd	Element wt. % ± error	Element at. % ± error
O K	4.277	37.91 ± 0.45	81.40 ± 0.97
Nb L	1.447	33.30 ± 0.50	12.31 ± 0.19
Gd L	1.211	28.78 ± 0.54	6.29 ± 0.12
Total		100	100

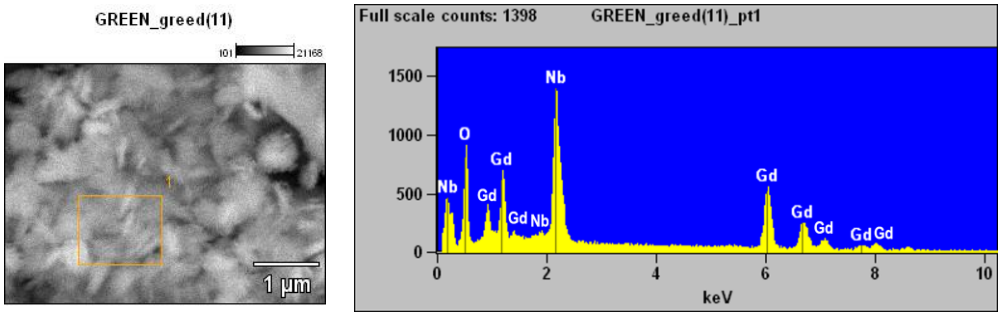

Figure 3.1.6.3. SEM image of the measured area and representative EDS spectra of flower-like morphology.

Table 3.1.6.3. EDS analysis of the flower-like morphology after three-step annealing at 120 ˚C (3 h), 200 ˚C (2 h), and 250 ˚C (16 h).

Element Line	ZAF Compnd	Element wt. % ± error	Element at. % ± error
O K	3.911	34.61 ± 0.40	80.02 ± 0.91
Nb L	1.532	28.23 ± 0.47	11.24 ± 0.19
Gd L	1.192	37.16 ± 0.85	8.74 ± 0.20
Total		100	100

Table 3.1.6.4. EDS analysis of the various morphologies after the thermal treatments at (1) 100 ˚C (15 min), and (2) 120 ˚C (3h), 200 ˚C (2h), and 250 ˚C (16h).

Morphology (thermal treatment)	Gd (at. %)	Nb (at. %)	O (at. %)	Nb:Gd	O:Nb
Bars (100 ˚C)	5.7 ± 0.2	12.4 ± 0.2	81.8 ± 0.4	2.1 ± 0.1	6.6 ± 0.1
Bars (250 ˚C)	6.0 ± 0.2	12.6 ± 0.6	81.4 ± 0.9	2.1 ± 0.1	6.5 ± 0.4
Cubes (100 ˚C)	5.5 ± 0.4	10.6 ± 0.5	83.9 ± 0.9	1.9 ± 0.1	7.9 ± 0.5
Cubes (250 ˚C)	6.2 ± 0.4	11.9 ± 0.7	81.9 ± 1.0	1.9 ± 0.1	6.9 ± 0.5
Flowers (100 ˚C)	7.2 ± 0.5	9.2 ± 0.4	83.5 ± 1.1	1.3 ± 0.1	9.1 ± 0.7
Flowers (250 ˚C)	8.9 ± 0.2	11.1 ± 0.3	80.0 ± 0.4	1.3 ± 0.1	7.2 ± 0.2

3.1.7. Raman

Raman spectra (**Figure 3.1.7.1**) with similar characteristics are observed for the bars and cubes. For flowers, some bands are missing or shifted (**Table 3.1.7.1**). Also, a few bands are shifted for cubes relative to the bars ("in parentheses"). The Raman modes correspond to different bond distances in the crystalline structure, and shifts of these bands indicate structural distortions [96]. Most of the observed bands (**Figure 3.1.7.1a**) are related to $GdNbO_4$ (in bold) [97–99] and $RETiNbO_6$ (in *italic*) [44,100] structures, indicating structural similarities [96]. It is important to note that the Raman bands reported for the $GdNbO_4$ structure match better the flower-like morphology, while some of these bands are shifted for bars and cubes (**Table 3.1.7.1**) [97–99]. These results confirm the presence of a mixed $GdNb_2O_6$/$GdNbO_4$ structure for the flower-like morphology. Also, Raman bands for $GdNb_2O_6$ are slightly shifted compared to reported $RETiNbO_6$ structures [44,100]. This behavior is expected due to the differences in the cation size [44,96,100]. The 261 cm^{-1} band is intense for bars and cubes and insignificant for flowers (260 cm^{-1}). This difference is most likely due to the dominance of the $GdNb_2O_6$ phase for bars and cubes and the structural distortion of a mixed $GdNb_2O_6$/$GdNbO_4$ phase for flowers [101,102]. The 494 (492) cm^{-1} band found for all three morphologies is reported for the $CaNb_2O_6$ [103]. Bands centered at 810, 835, 897, and 994 cm^{-1} are found in the Raman spectra for both the bars and cubes (**Figure 3.1.7.1b** and **3.1.7.1c**), while only bands centered at 810, 835, and 996 cm^{-1} are present for the flowers (**Table 3.1.7.1**, **Figure 3.1.7.1d**). The 810, 835, and 897 cm^{-1} bands are assigned to the NbO_6 octahedron [96,103,104], while the 994 cm^{-1} is associated with NbO_4 tetrahedra, Nb=O stretching vibration [105,106]. Consequently, both Nb^{+4} and Nb^{+5} species are present [107]. Previous studies [104,105] show that the 994 cm^{-1} band appears when the NbO_4 tetrahedra are dehydrated. In the present study, this band is observed before and after thermal treatment (**Figure 3.1.7.1**).

Table 3.1.7.1. Raman active modes (Raman shift in cm^{-1}) for the bar-, cube-, and flower-like morphologies. $GdNbO_4$ structure is in bold and $RETiNbO_6$ in italic.

Morphology	**Gd – O Vibration modes** **[cm^{-1}]** [98,100]	**NbO_6 Bending modes** **[cm^{-1}]** [44,98,100]	**NbO_6 Tilting modes** **[cm^{-1}]** [44,98]	**NbO_6 Stretching modes** **[cm^{-1}]** [44,98,100,103]
Bars (Cubes)	***120***, *157*	**178 (180)**, **218**, **233**, *261*, *290*, *303*, *308 (306)*, **331**	**368**, **416**, **430**, **457**, *485*, 494	*558 (556)*, **642 (644)**, **668**, **684**, *810*, *835*, 897, 994
Flowers	***120***	**180**, **220**, **235**, *260*, *297*, *303*, **333**	**368**, **417**, **430**, **457**, *485*, 492	*524*, **648**, **668**, **687**, *810*, *835*, 996

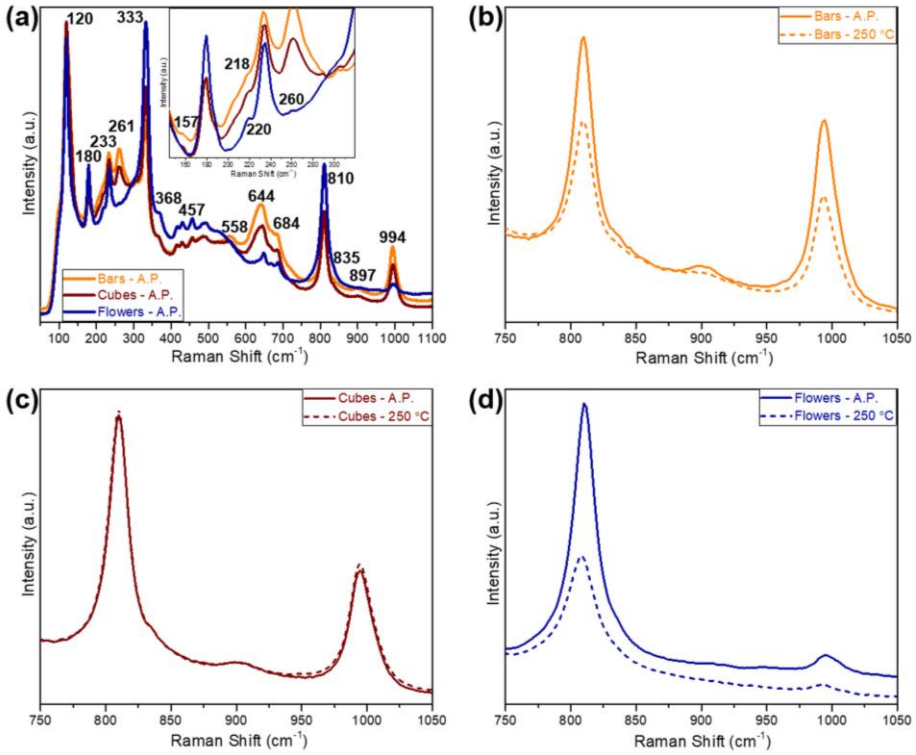

Figure 3.1.7.1. (a) Raman spectra (normalized to the most intense peak) in the range of 50 – 1100 cm^{-1}, with enlarged 150 – 320 cm^{-1} region, and 750 – 1050 cm^{-1} region of (b) bar-, (c) cube-, and (d) flower-like morphologies of as-prepared (solid line) and annealed 250 ˚C – 16 h (dash line).

3.1.8. Band Gap

The optical band gap (E_g) of the various morphologies is evaluated from the diffuse reflectance (F(R)) calculated with the Kubelka-Munk (K-M) method [108]. Where F(R) is proportional to the attenuation coefficient (α) and the general Tauc equation [109,110] for the band gap is modified [111]:

(3.1.8.1.)

$$\alpha h\upsilon \approx B(h\upsilon - E_g)^n \rightarrow F(R)h\upsilon \approx B(h\upsilon - E_g)^n$$

where *h* is Planck's constant (J·s), *B* represents the absorption constant, and υ is the photon frequency (Hz). The E_g is extracted by plotting $(F(R)\cdot h\upsilon)^n$ *vs.* $h\upsilon$ (photon energy in eV) (**Figure 3.1.8.1**). The case n = ½ is an indirect allowed transition, and n = 2 is a direct one [111]. It turned out that $GdNb_2O_6$ is an indirect band gap material with calculated E_g of 3.52 ± 0.01, 3.57 ± 0.01, and 3.63 ± 0.02 eV for the bar-, cube-, and flower-like morphologies, respectively (**Figure 3.1.8.1a**). These numbers are close to the reported value for $EuTiNbO_4$ (3.55 eV) [45]. The reported calculated and experimental E_g values for $GdNbO_4$ are 3.74 and 3.84 eV, respectively [50]. Hence, even though a mixed $GdNb_2O_6/GdNbO_4$ structure is present in the case of flowers, the band gap value tends to be closer to the one of $GdNb_2O_6$. In our case, the E_g values increase slightly with the change in the morphology (flowers > cubes > bars). It is shown in **Table 3.1.5.2** that the strain induced on the unit cell differs in between the bar- and cube-like morphologies, which is responsible for the slight shifts in the E_g [112,113]. Consequently, the optical band gap can be tuned by changing the morphology. The calculated band gaps of the $GdNb_2O_6$ various morphologies after the three-step thermal treatment ((1) 120 ˚C – 3 h, (2) 200 ˚C – 2 h, (3) 250 ˚C – 16 h) are 3.48 ± 0.02, 3.55 ± 0.01, and 3.58 ± 0.01 eV for the bars, cubes, and flowers, respectively (**Figure 3.1.8.1b**). In general, these values are lower when compared to the as-prepared $GdNb_2O_6$. These results confirm that water and OH^- groups attached to the nanoscale morphologies surface induce strain in these structures [94,95].

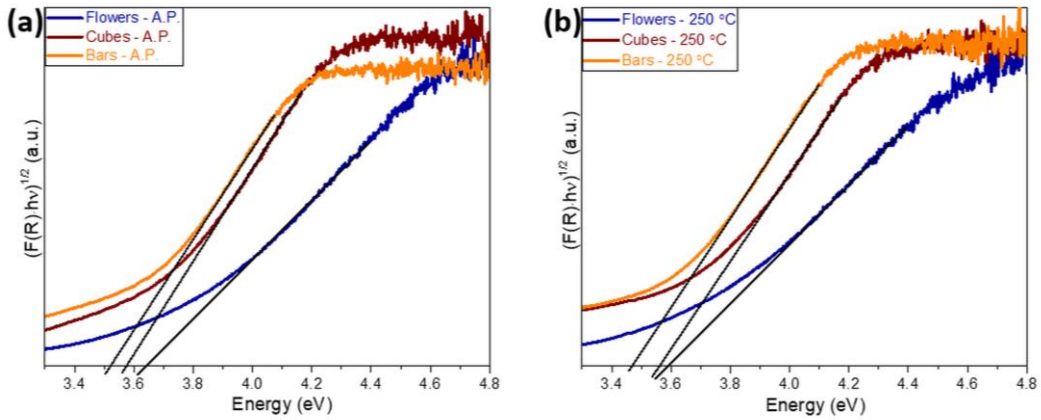

Figure 3.1.8.1. Calculated band gap for (a) as-prepared (A.P.) and (b) three-step thermally treated (250 ˚C) bars (orange), cubes (wine), and flowers (blue).

3.1.9. FTIR

FTIR spectra of the as-prepared morphologies (**Figure 3.1.9.1a**) show the presence of bands related to the water and OH^- groups (around 3350 – 3380 and 1625 – 1630 cm^{-1}), originated from the water and KOH involved in the synthesis process [114–116]. Additional bands centered at 1506 cm^{-1} and 1375 cm^{-1} are observed for the flower-like morphology (**Figure 3.1.9.1a**), corresponding to the NO_3^- groups stretching vibrations [117]. Broadband between 400 cm^{-1} and 1000 cm^{-1} present for all morphologies is related to the metal-oxide bonds [54] (**Figure 3.1.9.1b**). The peaks are shifted between the morphologies (**Figure 3.1.9.1b**), as listed in **Table 3.1.9.1**. A similar phenomenon is observed for ZnO NP's. These shifts are attributed to the preferential growth along a specific axis and oxygen defects at the NP's surface [118,119]. These results agree with the shift in the lattice parameters of the bar- and cube-like morphologies (**section 3.1.5**) [119].

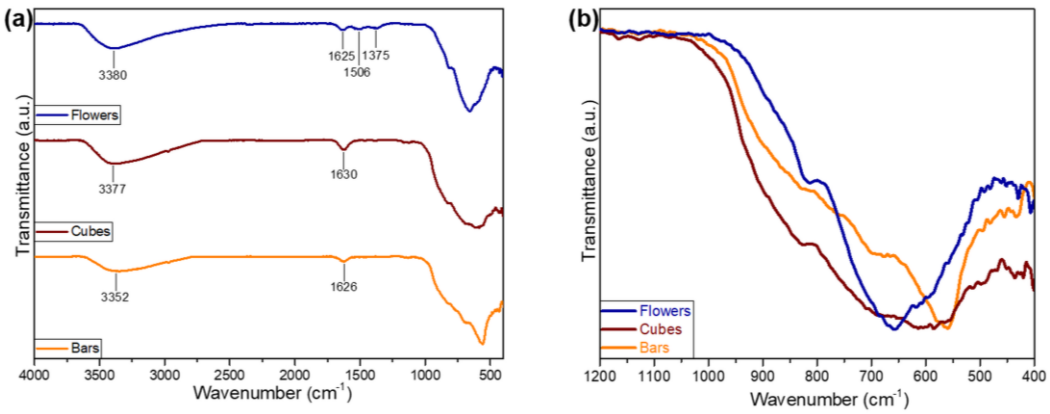

Figure 3.1.9.1. Transmittance FTIR spectra of the as-prepared submicron morphologies (a) complete and (b) magnified region at 400 - 1200 cm^{-1} for the bars (orange), cubes (wine), and flowers (blue).

Table 3.1.9.1. FTIR peaks related to the metal-oxide bonds.

Morphology	Peak 1 [cm^{-1}]	Peak 2 [cm^{-1}]	Peak 3 [cm^{-1}]	Peak 4 [cm^{-1}]	Peak 5 [cm^{-1}]	Peak 6 [cm^{-1}]
Bars	829	694	677	580	559	434
Cubes	827	690	675	584	554	436
Flowers	814	684	671	596	559	430

To eliminate the surface water and water trapped in between the crystallites, the submicron morphologies are thermally treated in three-step: (1) 120 ˚C – 3 h, (2) 200 ˚C – 2h, and (3) 250 ˚C – 16 h. After this annealing at 250 ˚C, the measured FTIR spectra (**Figure 3.1.9.2**) show that the broadband between ~2500 – 3600 cm^{-1} shifted to higher wavenumbers, 3437, 3427, and 3435 cm^{-1} for the bars, cubes, and flowers, respectively. These results suggest that water is mostly eliminated but a significant amount of OH^- groups remained attached to the submicron $GdNb_2O_6$ surface [120,121]. The surface hydroxyl is very stable and found for metal oxides even after annealing at temperatures higher than 600 ˚C. The more stable hydroxyl appears at higher frequencies in the FTIR spectra [115].

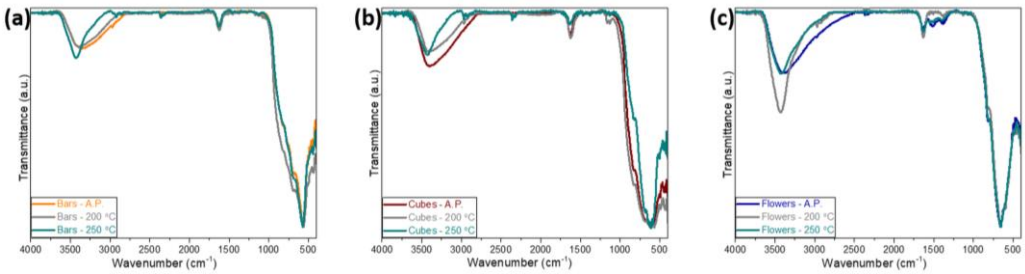

Figure 3.1.9.2. Transmittance FTIR spectra of the as-prepared (a) bars (orange), (b) cubes (wine), and (c) flowers (blue) and thermally treated at 200 ˚C (120 ˚C – 3 h and 200 ˚C – 4 h) and at 250 ˚C (120 ˚C – 3 h, 200 ˚C – 2 h, and 250 ˚C – 16 h).

In addition, after the three-step thermal treatment ((1) 120 ˚C – 3 h, (2) 200 ˚C – 2 h, (3) 250 ˚C – 16 h), a color change is observed for all three morphologies (**Figure 3.1.9.3**). This behavior might be attributed to the change in the oxidation state [122] due to the elimination of water molecules that were attached to the Nb (breakage of Nb–H_2O coordination bond) [105–107]. The color is less prominent for the flowers, presumably due to the presence of the mixed-phase and its morphology, where the bulk is negligible (**Figure 3.1.1.1**).

Figure 3.1.9.3. Powder of the (a) bar-, (b) cube-, and (c) flower-like morphologies before (as-prepared – A.P.) and after the three-step thermal treatment; (1) 120 ˚C for 3 h, (2) 200 ˚C for 2 h, and (3) 250 ˚C for 16 h (An.).

3.1.10. XPS

The XPS spectra of the Nb 3d doublet peaks for the as-prepared various morphologies are presented in **Figure 3.1.10.1**. The full information on the deconvoluted peaks is in **Tables 3.1.10.1-3.1.10.3**. The measured data and the

deconvolution (decon.) sum are mostly overlapping. The oxidation state of niobium oxides is frequently evaluated for Nb 3d orbitals, where a higher oxidation state is manifested at higher binding energies. Mixed niobium oxides with different oxidation states are often formed, and the peaks shift is discussed based on Nb^{4+} and Nb^{5+} characters' contributions [107,123–125]. The doublet peaks centered at 206.9, 209.6 eV, and 207.7, 210.5 eV for the bar-like morphology (**Figure 3.1.10.1a**) match the binding energies of NbO_2 (Nb^{4+} character) and Nb_2O_5 (Nb^{5+} character) phases, accordingly [123,126]. These peaks are located at 206.9, 209.6 eV, and 207.9, 210.4 eV in the case of cubes (**Figure 3.1.10.1b**) and at 206.3, 209.0 eV, and 207.4, 210.2 eV for the flowers (**Figure 3.1.10.1c**), similar to the reported values for $GdNbO_4$ [19]. The origin of the ~ 212.5 eV peak present for all three morphologies is unclear, but it is reported for HfO_2 [127]. These results imply that both Nb^{4+} and Nb^{5+} oxidation states are present on the surface of $GdNb_2O_6$ and $GdNb_2O_6/GdNbO_4$ compounds.

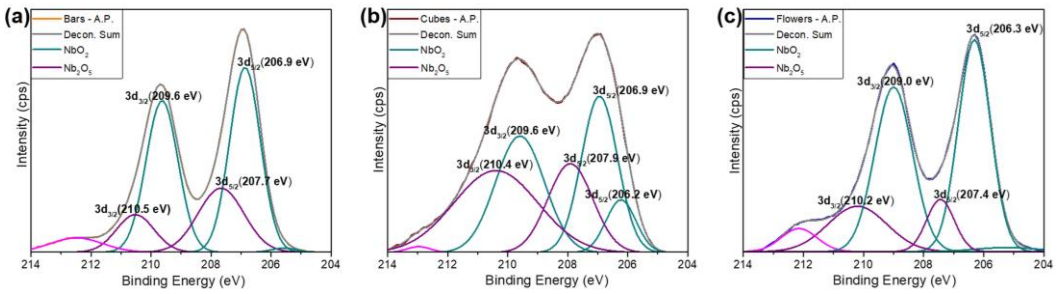

Figure 3.1.10.1. XPS spectra of the Nb 3d doublets peaks of the as-prepared (a) bar-(b) cube-, and (c) flower-like morphologies.

Table 3.1.10.1. XPS Nb 3d peaks deconvolution information for bar-like morphology.

Peak Type	Center	Height (cps)	Area (cps·eV)	FWHM (eV)
Gaussian	205.57	432.26	445.33	0.968
Gaussian	206.87	19045.50	24504.30	1.209
Gaussian	207.67	6606.88	12639.10	1.797
Gaussian	209.63	15620.40	20916.60	1.258
Gaussian	210.53	3875.83	6082.98	1.474
Gaussian	212.48	1477.21	3221.51	2.049

Table 3.1.10.2. XPS Nb 3d peaks deconvolution information for cube-like morphology.

Peak Type	Center	Height (cps)	Area (cps·eV)	FWHM (eV)
Gaussian	206.23	2723.00	3399.60	1.173
Gaussian	206.94	8053.32	12165.20	1.419
Gaussian	207.91	4576.09	8586.7	1.762
Gaussian	209.59	5992.87	12245.50	1.920
Gaussian	210.39	4225.38	14869.70	3.306
Gaussian	212.97	314.17	319.58	0.956

Table 3.1.10.3. XPS Nb 3d peaks deconvolution information for flower-like morphology.

Peak Type	Center	Height (cps)	Area (cps·eV)	FWHM (eV)
Gaussian	205.232	394.282	1030.740	2.456
Gaussian	206.309	19693.500	26476.500	1.263
Gaussian	207.439	4864.220	5602.270	1.082
Gaussian	208.997	15305.900	24074.800	1.478
Gaussian	210.203	4224.820	10396.200	2.312
Gaussian	212.146	2151.420	3232.160	1.411

3.1.11. PL (Pristine and Water Related)

In the case of gadolinium niobate fergusonite structure $GdNbO_4$ (prepared *via* solid-state method), a weak blue-white emission centered at λ_{em} = 440 nm is reported at room temperature when it excited with λ_{ex} = 254 nm. In addition, a yellow weak emission (for λ_{ex} = 365 nm) is reported at 77 K (quenched at room temperature) [48,128]. This emission is attributed to the $(NbO_4)^{3-}$ groups. The emission is weak due to significant energy transfer to the Gd^{3+} ions that are abundant in the structure. This energy transfer process eventually leads to luminescence quenching. The λ_{ex} = 365 nm excitation band is related to the $^1A_1 \rightarrow {}^3T_2$ transitions of the $(NbO_4)^{3-}$ groups [50] and is responsible for the weak emission in the 300 – 500 nm region [54]. In the current study, distinctive PL characteristics is observed at room temperature for all three morphologies before and after the water elimination.

The excitation (240 – 380 nm) and the emission (415 – 700 nm) spectra of $GdNb_2O_6$ before (as-prepared) and after the thermal treatment (annealed at 250 ˚C) are depicted in **Figure 3.1.11.1**. For the excitation wavelength of λ_{ex} = 365 nm, all the as-prepared morphologies present an emission peak at about λ_{em} = 440 nm (**Figures 3.1.11.1a, 3.1.11.1b,** and **3.1.11.1c**), which is several orders of magnitude more intense for the cubes (**Figure 3.1.11.1b**). A similar peak is observed for layered double hydroxides (LDH) such as ZnAl [129] and MgAl [130], and it is attributed to surface defects and interactions with solvent in the case of the colloidal suspension. In addition, the as-prepared flowers (**Figure. 3.1.11.1c**) present broad emission peaks centered at about λ_{em} = 550 and λ_{em} = 580 nm when the material is excited with λ_{ex} = 254 and λ_{ex} = 310 nm, respectively. The excitation bands centered at λ_{ex} = 270 and λ_{ex} = 310 nm are attributed to the $(NbO_4)^{3-}$ groups ($^1A_1 \rightarrow {}^1T_2$ transitions) [54] and Gd^{3+} ions ($^6P_{7/2} \rightarrow {}^8S_{7/2}$ transitions), respectively, in the case of $GdNbO_4$ [18,131]. For the bar- and cube-like morphologies, the emission centered at λ_{em} = 550 nm is weak for the λ_{ex} = 310 nm excitation wavelength before and after the thermal

treatment (**Figures 3.1.11.1a, 3.1.11.1d,** and **3.1.11.1b, 3.1.11.1e,** respectively) and quenched for λ_{ex} = 254 nm.

After the three-step thermal treatment ((1) 120 ˚C – 3 h, (2) 200 ˚C – 2h, and (3) 250 ˚C – 16 h), the emission spectra obtained with λ_{ex} = 365 nm are broadband for all three morphologies (**Figures 3.1.11.1d, 3.1.11.1e,** and **3.1.11.1f**). The PL emission is centered at about λ_{em} = 550 nm for bars (**Figure 3.1.11.1d**) and cubes (**Figure 3.1.11.1e**). For flowers, the emission is centered at about λ_{em} = 480 nm with an additional peak around λ_{em} = 550 nm. Likewise, for flowers, the intensity of the λ_{em} = 550 nm and λ_{em} = 580 nm emissions is reduced for λ_{ex} = 254 nm and λ_{ex} = 310 nm, respectively, when compared to the as-prepared material (**Figures 3.1.11.1c** and **3.1.11.1f**). In addition, after the thermal treatment, the intensity of the excitation band for λ_{em} = 550 nm increased by a factor of 9.0, 4.2, and 1.6 for bars, cubes, and flowers, respectively (**Figure 3.1.11.1**). That must be attributed to a competitive energy transfer mechanism of water and niobium oxide groups of the $GdNb_2O_6$ matrix. After a significant elimination of water, transitions through the energy levels of niobium oxide dominate.

These results imply that water at the surface and in between the crystallite slabs has a direct effect on the PL of the pristine $GdNb_2O_6$. This behavior is most prominent in cubes (**Figures 3.1.11.1b** and **3.1.11.1e**), where the intense blue emission at λ_{em} = 440 nm (originated from water) [132] vanishes after the thermal treatment together with excitation bands at about λ_{ex} = 278 nm [130]. The excitation band of water-related emission at λ_{ex} = 370 nm [129,133] overlaps with the one of the pristine $GdNb_2O_6$. Nonetheless, after annealing, the intensity of the excitation band monitored for λ_{em} = 440 nm is suppressed and shift to λ_{ex} = 366 nm (**Figures 3.1.11.1b** and **3.1.11.1e**). It is important to note that for the bar-like morphology, a small peak at λ_{em} = 440 nm is present in addition to the λ_{em} = 550 nm band after the thermal treatment (**Figure 3.1.11.1d**). This peak must be related to a minute amount of water adsorbed by the $GdNb_2O_6$ surface at the moment of measurement due to exposure to air humidity.

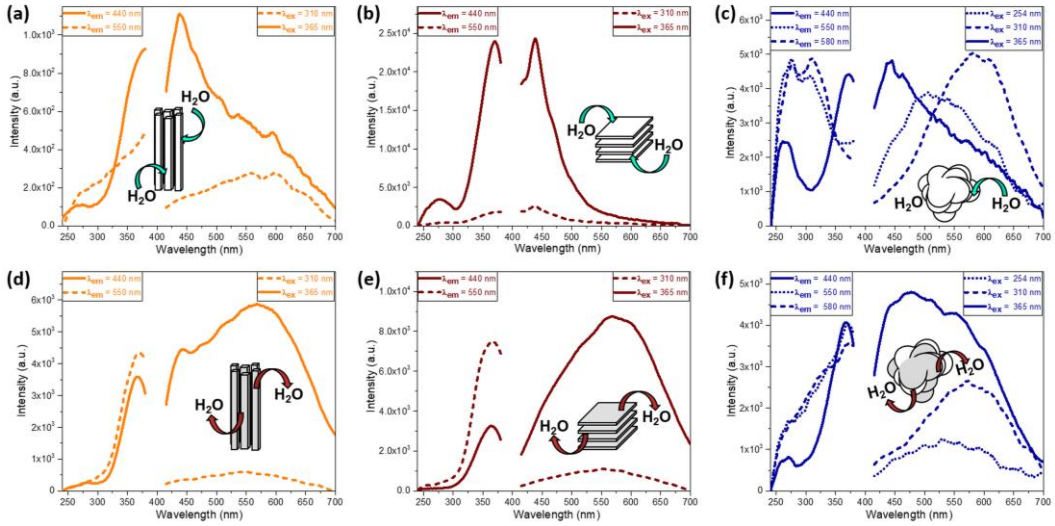

Figure 3.1.11.1. Excitation (240 – 380 nm) and emission (415 – 700 nm) spectra of as-prepared (a), (b), (c) and annealed (d), (e), (f), bars (orange), cubes (wine), and flowers (blue), respectively.

3.1.12. Intrinsic PL Stability

To evaluate the PL stability of the $GdNb_2O_6$ various morphologies, the powders that are thermally treated in three steps ((1) 120 ˚C – 3 h, (2) 200 ˚C – 2h, and (3) 250 ˚C – 16 h) are stored for 60 days in the air and then thermally treated only in two steps (120 ˚C – 3 h, 200 ˚C – 1 h). After the thermal treatment at 250 ˚C, the broad λ_{em} = 550 nm band is observed for the bars and cubes (**Figure 3.1.12.1a**). It is important to mention that for the bar-like morphology, a small peak at λ_{em} = 440 nm is present in addition to the λ_{em} = 550 nm band after this thermal treatment at 250 ˚C (**Figure 3.1.12.1a**). This peak must be related to a minute amount of water adsorbed by the $GdNb_2O_6$ surface at the moment of measurement due to exposure to air humidity, as discussed in **section 3.1.11**. After the exposure of the annealed bar- and cube-like morphologies to air for 60 days, the λ_{em} = 440 nm peak associated with water is present for both morphologies. Nonetheless, for the cubes, the intensity of the water-related peak

is of lesser intensity compared to the as-prepared material (**Figure 3.1.11.1b**). These results imply that the process of water reabsorption is slow and that the as-prepared material contains more water. After the annealing at 200 ˚C (**Figure 3.1.11.1c**), the λ_{em} = 440 nm water-related peak is quenched, and the broadband centered at λ_{em} = 550 nm is of similar intensity as after annealing at 250 ˚C, for both bars and cubes (**Figure 3.1.11.1a**). Hence, the bar- and cube-like morphology present stability for the repeated thermal treatment. Also, only short annealing is necessary to eliminate the reabsorbed water (120 ˚C – 3 h, 200 ˚C – 1 h). For the flowers (**Figure 3.1.11.1d**), the λ_{em} = 440 nm water-related peak is present after the exposure to air for 60 days. In addition, after the thermal treatment at 200 ˚C, the λ_{em} = 440 nm peak remains present. Most likely, longer annealing times (> 1 h) or/and higher temperature (> 200 ˚C) are necessary to restore the broadband emission (λ_{em} = 550 nm) for the flowers.

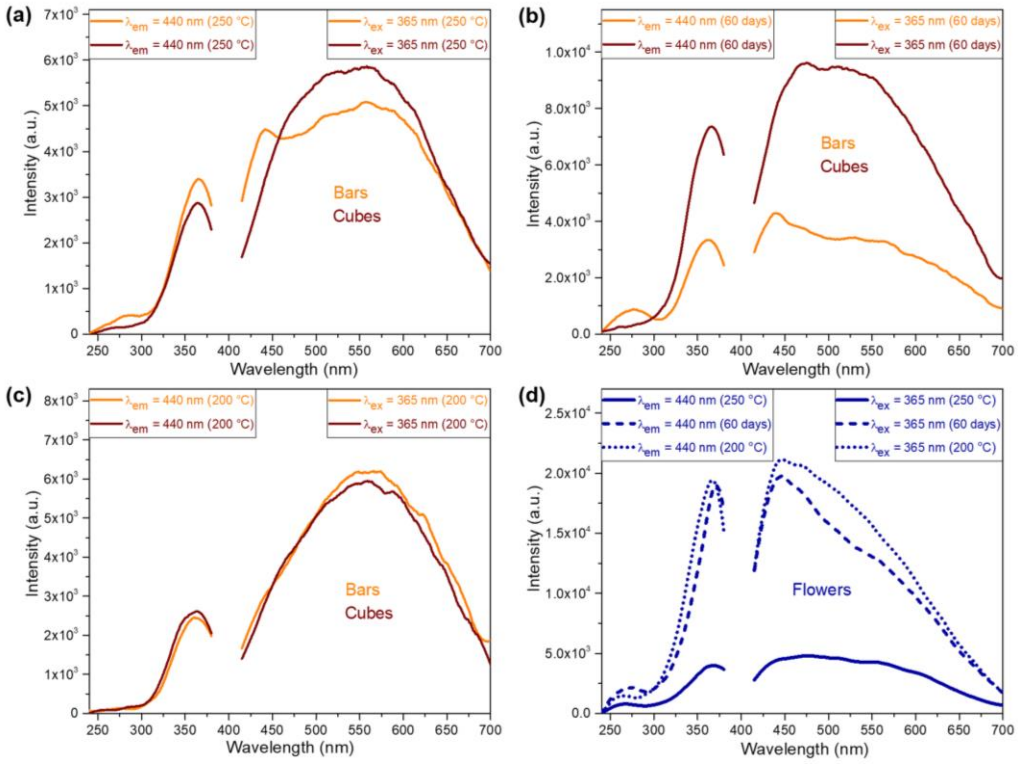

Figure 3.1.12.1. Excitation (240 – 380 nm) and emission (415 – 700 nm) spectra after (a) annealing at 250 ˚C (b) 60 day in air, and (c) annealing at 200 ˚C for bars (orange) and cubes (wine) and (d) similar spectra for flowers (blue).

3.2. Thulium (Tm^{3+}) Doped Material

3.2.1. XRD and Rietveld Analysis

The diffraction patterns of the as-prepared undoped $GdNb_2O_6$ and thulium-doped $Gd_{0.96}Tm_{0.04}Nb_2O_6$ cubes are similar (**Figure 3.2.1.1**). All the peaks of the $GdNb_2O_6$ phase are present with small shifts. These shifts are manifested in the values of the lattice parameters (**Table 3.2.1.1**), and it is most likely rises due to the difference in the ionic (crystal) radius of Gd^{3+} 1.053 Å (1.193 Å) and Tm^{3+} 0.994 Å (1.134 Å) [57,134]. Rietveld analysis of the $Gd_{0.96}Tm_{0.04}Nb_2O_6$ diffractogram results in low values of R_p, R_{wp}, and GOF (**Table 3.2.1.1**). These results confirm that $Gd_{0.96}Tm_{0.04}Nb_2O_6$ phase is in good agreement with the intrinsic $GdNb_2O_6$. Evaluation of the micro-strain (**Table 3.2.1.2**) shows higher values for $Gd_{0.96}Tm_{0.04}Nb_2O_6$ structure when compared to the intrinsic $GdNb_2O_6$. It is possible to see in **Figure 3.2.1.1** that in the 10 – 15 ˚ and 25 – 35 ˚ 2-theta regions, an amorphous phase is present for $Gd_{0.96}Tm_{0.04}Nb_2O_6$. The origin of the amorphous phase can be from the adsorbed water and OH^- groups, which leads to a surface strain [94,95].

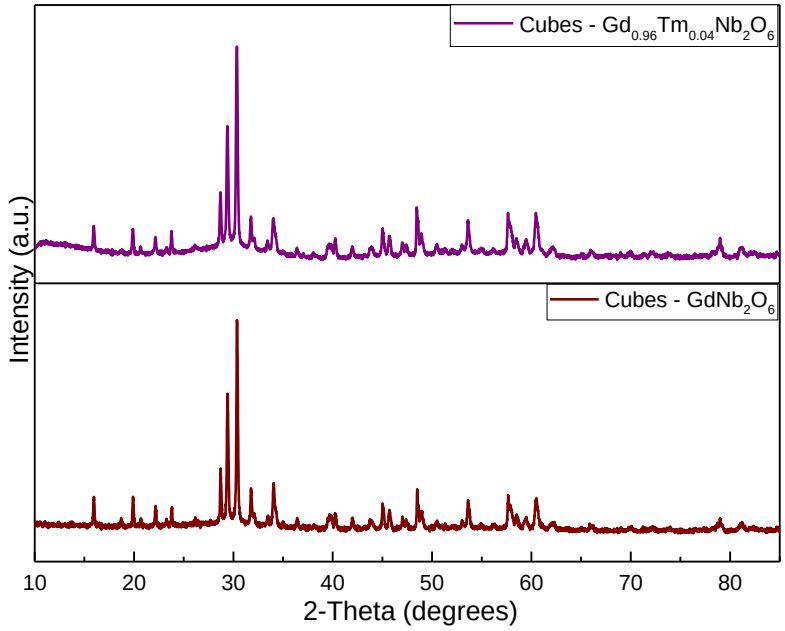

Figure 3.2.1.1. XRD patterns of cube-like morphology of $GdNb_2O_6$ (wine) and $Gd_{0.96}Tm_{0.04}Nb_2O_6$ (purple).

Table 3.2.1.1. Lattice parameters (*a*, *b*, *c*), R_p, R_{wp}, and GOF, obtained from the Rietveld analysis using HighScore Plus (HSP) [83].

Morphology	*a*	*b*	*c*	R_p [%]	R_{wp} [%]	GOF [%]
Cubes ($GdNb_2O_6$)	11.2060(4)	7.5212(2)	5.2864(2)	3.01	3.90	1.24
Cubes ($Gd_{0.96}Tm_{0.04}Nb_2O_6$)	11.1928(4)	7.5178(0)	5.2833(3)	3.14	4.01	4.63

Table 3.2.1.2. Micro-strains ε_{hkl} obtained from HSP for the lattice parameters *a*, *b*, *c*.

Morphology	*a* ε_{200} [%]	*b* ε_{020} [%]	*c* ε_{002} [%]
Cubes ($GdNb_2O_6$)	0.271	0.352	0.186
Cubes ($Gd_{0.96}Tm_{0.04}Nb_2O_6$)	0.495	0.376	0.239

3.2.2. Morphology

The morphology of the $Gd_{0.96}Tm_{0.04}Nb_2O_6$ is shown in **Figure 3.2.2.1**. The morphology of the bars and flowers (**Figures 3.2.2.1a** and **3.2.2.1c**) is similar to the undoped $GdNb_2O_6$ (**Figure 3.1.1.1**). Nonetheless, some of the cubes (**Figure 3.2.2.1b**) appear with more open layers when compared to the intrinsic $GdNb_2O_6$ (**Figure 3.1.1.1c**). That must be the result of the use of thulium(III) chloride hexahydrate instead of nitride as in the case of gadolinium ($Gd(NO_3)_3 \cdot 6H_2O$). The addition of chloride changes the pH of the precursors' solution, and therefore the preferred cube-like morphology is obtained at lower pH values. A similar effect is observed for Nd^{3+} doped material (**Figure 3.3.2.1**), where the desired cube-like morphology is achieved at lower pH values. In this case, doping does not lead to morphological changes as often occur for doped materials [135].

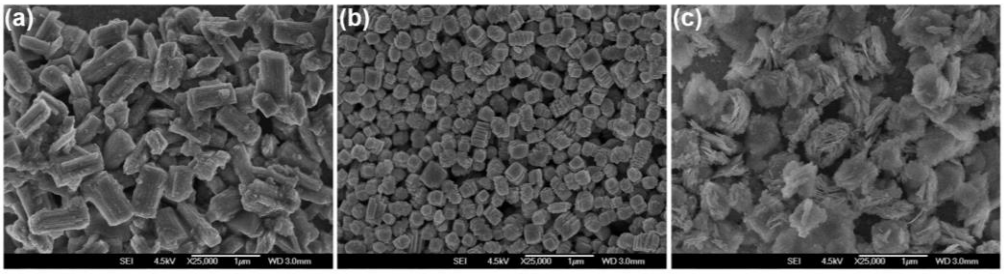

Figure 3.2.2.1. SEM images of $Gd_{0.96}Tm_{0.04}Nb_2O_6$ (a) bar-, (b) cube-, and (c) flower-like morphologies.

3.2.3. Band Gap

The measured band gap values of the as-prepared (**Figure 3.2.3.1a**) thulium-doped $GdNb_2O_6$ ($Gd_{1-0.96}Tm_{0.04}Nb_2O_6$) are 3.48, 3.60, and 3.58 eV for the bars, cubes, and flowers, respectively. For the material that annealed in three steps ((1) 120 ˚C – 3 h, (2) 200 ˚C – 2h, and (3) 250 ˚C – 16 h)) the band gaps are 3.44, 3.68, and 3.59 eV for the bars, cubes, and flowers, accordingly (**Figure 3.2.3.1b**). When compared to the intrinsic $GdNb_2O_6$ (**Figure 3.1.8.1**), band gap values of as-prepared $Gd_{0.96}Tm_{0.04}Nb_2O_6$ bars and flowers (**Figure 3.2.3.1a**) are similar to the ones of the undoped material after the annealing (**Figure 3.1.8.1b**). After the thermal treatment, the band gap of the $Gd_{0.96}Tm_{0.04}Nb_2O_6$ bars is reduced and remains similar for the flowers (**Figure 3.2.3.1b**). As for the as-prepared and annealed $Gd_{0.96}Tm_{0.04}Nb_2O_6$ cubes, the band gap values are higher (**Figures 3.2.3.1a** and **3.2.3.1b**) when compared to the intrinsic material (**Figures 3.1.8.1a** and **3.1.8.1b**). That must be the result of a higher amount of an amorphous phase, probably originating from the water and OH^- groups, as was shown by the XRD analysis in **section 3.2.1**. An additional reason can be the slight difference in the morphology (**Figure 3.2.2.1**) compared to the intrinsic material (**Figure 3.1.1.1**).

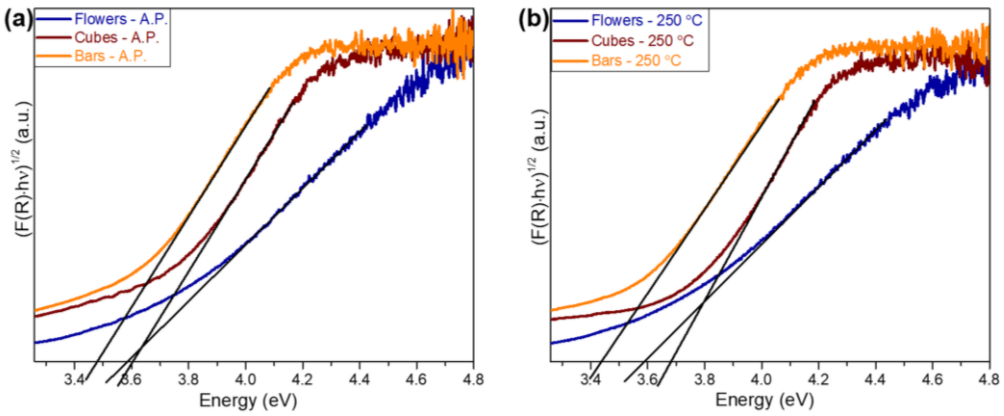

Figure 3.2.3.1. Band gap of $Gd_{0.96}Tm_{0.04}Nb_2O_6$ bar-, cube-, and flower-like morphologies (a) as-prepared and (b) annealed in three steps ((1) 120 ˚C – 3 h, (2) 200 ˚C – 2h, and (3) 250 ˚C – 16 h)).

3.2.4. PL (Thulium and Water Related)

The PL properties of thulium-doped gadolinium niobate ($Gd_{1-x}Tm_xNb_2O_6$) nanophosphors are analyzed concerning Tm^{3+} and water-associated emissions (**Figure 3.2.4.1**). The as-prepared (A.P.) cube-like morphology doped with different concentrations of Tm^{3+} show a λ_{em} = 457 nm emission for the excitation wavelength of λ_{ex} = 361 nm ($^3H_6 \rightarrow {}^1D_2$ transitions) [20] (**Figure 3.2.4.1a**). This emission is associated with the $^1D_2 \rightarrow {}^3F_4$ inter-electronic energy levels transitions of Tm^{3+} ion [16]. For as-prepared $Gd_{0.99}Tm_{0.01}Nb_2O_6$, only the λ_{em} = 440 nm peak related to water emission is present (**Figure 3.2.4.1a**). In addition, a broadband in the excitation spectra (240 – 380 nm) for this emission peak, centered at λ_{ex} = 278 nm [130], is observed. It is important to note that the λ_{ex} = 361 nm of Tm^{3+} ion is overlapping with the excitation band of the host matrix (niobium oxide, λ_{ex} = 365 nm) [48] and water (λ_{ex} = 370 nm) [133]. As the concentration of Tm^{3+} is increased, the λ_{em} = 457 nm emission is more evident, and the water-related peak is less prominent (**Figure 3.2.4.1a**). The intensity of the λ_{ex} = 278 nm band for $Gd_{0.96}Tm_{0.04}Nb_2O_6$ is reduced compared to $Gd_{0.93}Tm_{0.03}Nb_2O_6$ (**Figure 3.2.4.1a**), together with the λ_{em} = 440 nm of water. After the three-step thermal treatment (250 ˚C) (**Figure 3.2.4.1b**), an

intense λ_{em} = 550 nm broad emission originated from the host matrix (niobium oxide groups) is observed for $Gd_{0.97}Tm_{0.03}Nb_2O_6$ together with λ_{em} = 457 nm of Tm^{3+}. These results agree with those obtained for the undoped material (**Figure 3.1.11.1**), where a broad emission appears after the thermal treatment (water elimination). As for the $Gd_{0.96}Tm_{0.04}Nb_2O_6$, the emission from the matrix is significantly reduced, and the emission from the Tm^{3+} ions dominates. These results indicate that the emission associated with water and niobium oxide groups is quenched with the increased Tm^{3+} doping concentration. Therefore, the $Gd_{0.96}Tm_{0.04}Nb_2O_6$ composition is chosen for the synthesis of bars and flowers to study the Tm^{3+}-related emission.

Among the three synthesized morphologies (bars, cubes, and flowers), the as-prepared $Gd_{0.96}Tm_{0.04}Nb_2O_6$ bars present the lowest λ_{em} = 457 nm emission intensity (**Figure 3.2.3.1c**), and the water-related peak (λ_{em} = 440 nm) is evident only in the case of cubes. This behavior is consistent with the results for the undoped $GdNb_2O_6$, where the λ_{em} = 440 nm emission is several orders of magnitude higher for the as-prepared cubes when compared to bars and flowers (**Figures 3.1.11.1a, 3.1.11.1b,** and **3.1.11.1c**). In addition, for flowers, the λ_{ex} = 250 nm band is present before (**Figure 3.2.4.1c**) and after the thermal treatment (**Figure 3.2.4.1d**). This excitation is attributed to the charge transfer band ($O^{2-} \rightarrow Nb^{5+}$) in the case of Tm^{3+} doped $GdNbO_4$ [15].

After the three-step thermal treatment (250 ˚C), compared to the as-prepared $Gd_{0.96}Tm_{0.04}Nb_2O_6$ (**Figure 3.2.4.1c**) nanophosphors, the λ_{em} = 457 nm blue emission is more intense in the case of flowers (**Figure 3.2.4.1d**). On the contrary, this emission is lower for the bars and cubes (**Figure 3.2.4.1d**). It is evident for cubes that the λ_{em} = 440 nm water-related emission (**Figure 3.2.4.1c**) vanished after the thermal treatment (**Figure 3.2.4.1d**). These results imply that for as-prepared $Gd_{0.96}Tm_{0.04}Nb_2O_6$ bars and cubes, the λ_{em} = 457 nm is partially assisted by the water-related emission (**Figures 3.2.4.1c** and **3.2.4.1d**).

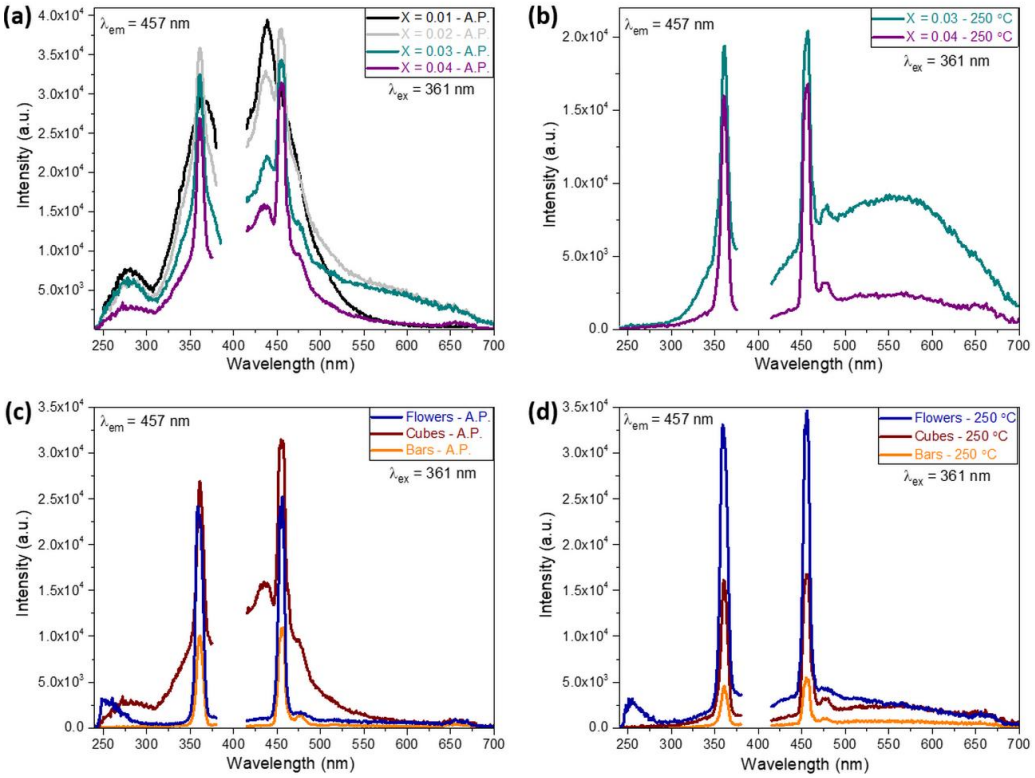

Figure 3.2.4.1. Excitation (250 – 380 nm) and emission (415 – 700 nm) spectra for the as-prepared (A.P.) and the thermally treated (250 ˚C) various submicron morphologies of $Gd_{1-x}Tm_xNb_2O_6$; (a) A.P. and (b) annealed cubes with different concentration of Tm^{3+}, (c) A.P. and (d) thermally treated $Gd_{0.96}Tm_{0.04}Nb_2O_6$ bars (orange), cubes (wine) and flowers (blue).

3.3. Neodymium (Nd^{3+}) Doped Material

3.3.1. XRD

The XRD patterns of the as-prepared and annealed Nd^{3+} doped $GdNb_2O_6$ ($Gd_{0.97}Nd_{0.03}Nb_2O_6$) cubes are shown in **Figure 3.3.1.1**. The diffractograms of the as-prepared and annealed at 500 ˚C $Gd_{0.97}Nd_{0.03}Nb_2O_6$ present similar characteristics. These XRD patterns match the $GdNb_2O_6$ crystalline structure. Nonetheless, when the material is thermally treated at 800 ˚C, structural changes

are observed ($Gd_{1-x}Nd_xNb_yO_z$). After the annealing at 800 ˚C, the crystalline phase becomes mainly monoclinic $GdNbO_4$ (**Figure 3.3.1.1**) with additional peaks related to the Gd_3NbO_7 and $GdNb_2O_6$ crystalline structures.

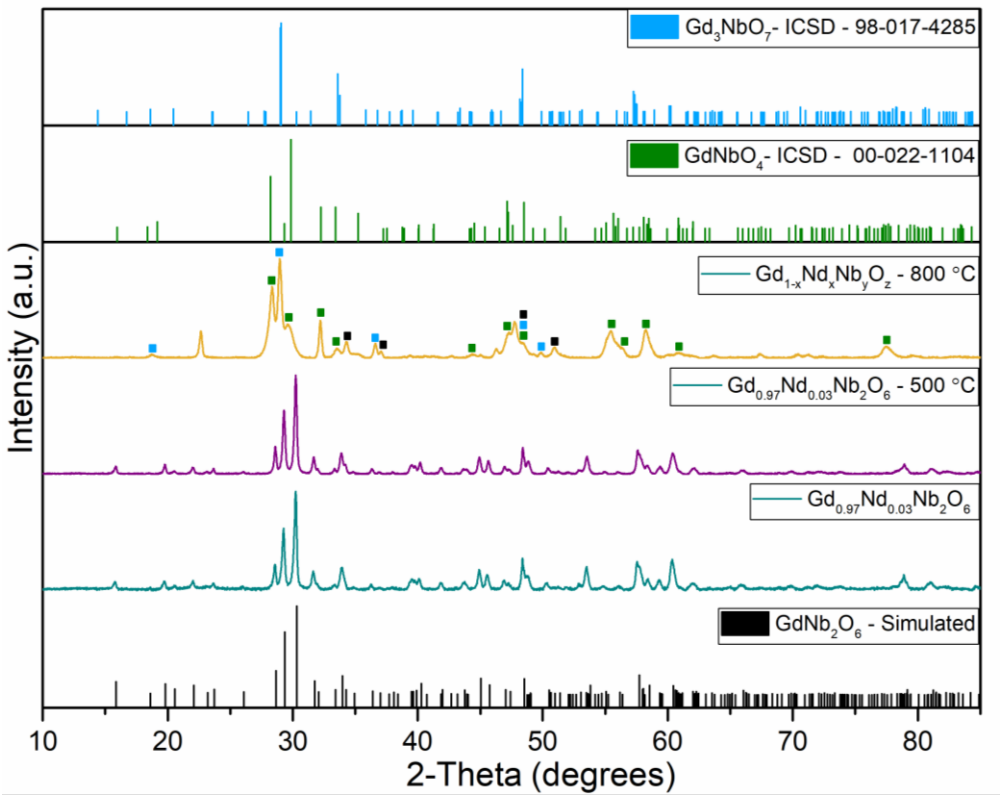

Figure 3.3.1.1. XRD patterns of the as-prepared and annealed at 500 ˚C and 800 ˚C $Gd_{0.97}Nd_{0.03}Nb_2O_6$.

3.3.2. Morphology

The morphology of the $Gd_{0.97}Nd_{0.03}Nb_2O_6$ is shown in **Figure 3.3.2.1**. For the pH > 7.10, some of the cubes (**Figure 3.3.2.1b**) appear with more open layers, and the layers are less defined when compared to the material prepared at pH < 7.10 (**Figure 3.3.2.1a**). That must be a result of neodymium(III) chloride hexahydrate used instead of nitride, as in the case of gadolinium ($Gd(NO_3)_3 \cdot 6H_2O$). The addition of chloride changes the pH of the precursors' solution, and therefore the preferred cube-like morphology is obtained at lower pH values (**Figure 3.3.2.1a**). Similar is happening for the Tm^{3+} doped material

(**Figure 3.2.2.1b**). As in the case of Tm^{3+} doping, morphological changes don't occur with the addition of the doping (**Figure 3.3.2.1a**) [135].

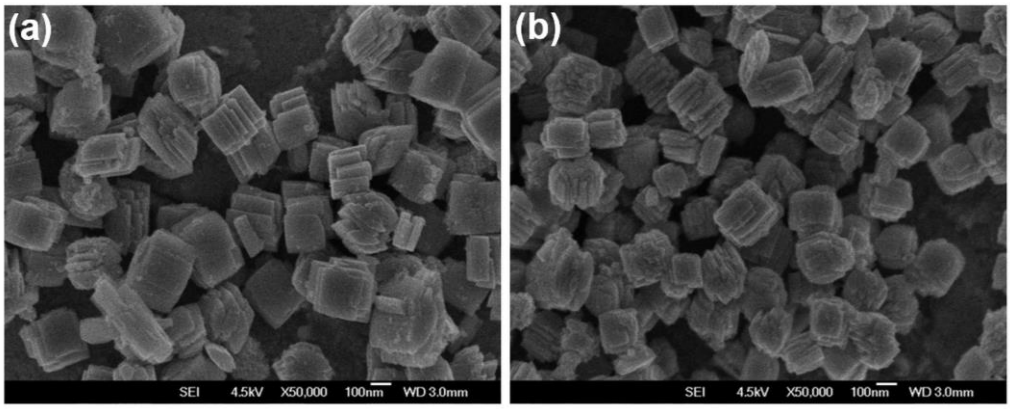

Figure 3.3.2.1. Morphology of $Gd_{0.97}Nd_{0.03}Nb_2O_6$ for precursors' solution temperature 18 – 19 ˚C and (a) pH = 7.06 and (b) pH = 7.26.

SEM images in **Figure 3.3.2.2** presents the morphology of as-prepared and annealed $Gd_{0.97}Nd_{0.03}Nb_2O_6$ cubes. It is clear from **Figures 3.3.2.2a**, **3.3.2.2b** and **3.3.2.2c**, **3.3.2.2d** that the temperature of 500 ˚C does not lead to any morphological changes. The layers of the cube-like morphology are preserved. After annealing at 800 ˚C, the layered structure is completely lost, and aggregates are formed (**Figures 3.3.2.2e**, **3.3.2.2f**).

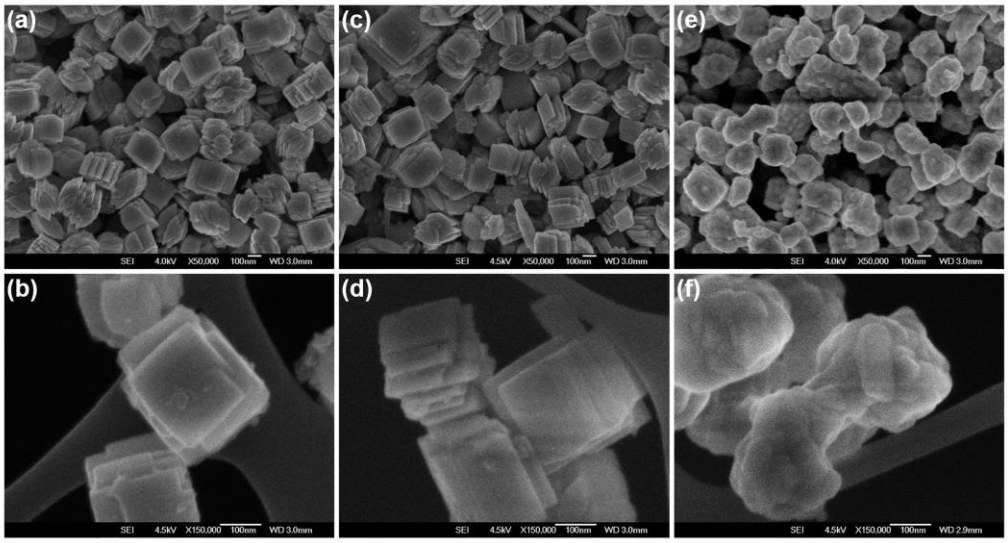

Figure 3.3.2.2. Low and high magnifications SEM images of $Gd_{0.97}Nd_{0.03}Nb_2O_6$ (a), (b) as-prepared, (c), (d) annealed at 500 ˚C, and (e), (f) annealed at 800 ˚C.

3.3.3. FTIR

For the elimination of surface water and water trapped in between the crystallites, the $Gd_{0.97}Nd_{0.03}Nb_2O_6$ cubes are thermally treated in four-steps: (1) 120 ˚C – 3 h, (2) 200 ˚C – 2h, (3) 250 ˚C – 4 h, and (4) 500 ˚C or 800 ˚C – 16 h. After this annealing at 500 ˚C and 800 ˚C, the measured FTIR spectra (**Figure 3.3.3.1**) show that the broadband between ~2500 – 3600 cm^{-1} related to water and OH^- groups is significantly reduced with increased annealing temperature. These results suggest that the content of water and OH^- groups are considerably reduced for the material annealed at 800 ˚C when compared to the as-prepared one [120,121].

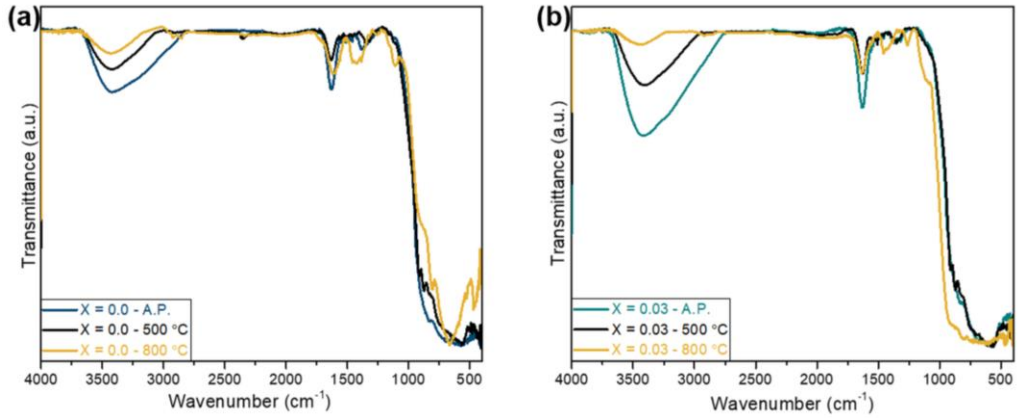

Figure 3.3.3.1. Transmittance FTIR spectra of the as-prepared and thermally treated at 500 ˚C and 800 ˚C (a) $GdNb_2O_6$ and (b) $Gd_{1-x}Nd_xNb_2O_6$.

3.3.4. PL (Neodymium and Water Related)

The excitation (240 – 380 nm and 415 – 700 nm) and the emission (415 – 700 nm and 850 – 1200 nm) spectra of $Gd_{1-x}Nd_xNb_2O_6$ cube-like morphology, annealed at 500 ˚C and 800 ˚C, are depicted in **Figure 3.3.4.1**. For the excitation wavelength of λ_{ex} = 358 nm, the material annealed at 500 ˚C presents near-infrared (NIR) emission peaks at about λ_{em} = 1071 and 881 nm (**Figure 3.3.4.1a**). For the thermal treatment of 800 ˚C, the optical emission for λ_{ex} = 358 nm is quenched in the 850 – 1200 nm region (**Figure 3.3.4.1b**). When the material annealed at 500 ˚C is excited with visible light (λ_{ex} = 586 nm), the λ_{em} = 1071 and 881 nm are observed (**Figure 3.3.4.1c**). The Nd^{3+}-related emission for the excitation with visible light is of higher intensity after annealing at 800 ˚C (**Figure 3.3.4.1d**). In addition, for this annealing temperature, the excitation and emission wavelengths are shifted to λ_{ex} = 590 nm and λ_{em} = 1065 and 890 nm, respectively. Similar results are reported for the $GdNbO_4$ crystalline structure [54]. It agrees with the XRD patterns (**Figure 3.3.1.1**), where structural changes are observed after annealing at 800 ˚C. The emissions at λ_{em} = 872, 877, 890, 925, and 1065 nm are associated with characteristic 4f intra-electronic energy transitions of Nd^{3+} ions, $^4F_{3/2} \rightarrow {}^4I_{9/2}$, $^2P_{1/2} \rightarrow {}^4F_{3/2}$, $^4F_{3/2} \rightarrow {}^4I_{9/2}$, $^2P_{1/2} \rightarrow {}^4F_{5/2}$, and $^4F_{3/2} \rightarrow {}^4I_{11/2}$, respectively [54,136,137]. In the visible range (**Figures**

3.3.4.1e and **3.3.4.1f**), for excitation wavelength of λ_{ex} = 360 nm, emissions at λ_{em} = 418, 456, and 504 nm, associated with intra-electronic energy transitions of Nd^{3+} ions, $^4D_{3/2} \rightarrow {}^4I_{13/2}$, $^2G_{9/2} \rightarrow {}^4I_{9/2}$ ($^4D_{3/2} \rightarrow {}^4I_{15/2}$ and $^2P_{3/2} \rightarrow {}^4I_{13/2}$), and $^2P_{3/2} \rightarrow {}^4I_{15/2}$, respectively, are present for both annealing temperatures (500 ˚C and 800 ˚C) [136]. In addition, Nd^{3+}-related emission at λ_{em} = 600, 610 nm ($^2P_{3/2} \rightarrow {}^4I_{13/2}$), and 656 nm ($^4D_{3/2} \rightarrow {}^4F_{5/2}$, 500 ˚C) and λ_{em} = 614, and 657 nm (800 ˚C) are observed (**Figures 3.3.4.1e** and **3.3.4.1f**) [136]. The best material annealed at 500 ˚C is $Gd_{0.97}Nd_{0.03}Nb_2O_6$ for both excitation wavelengths λ_{ex} = 358 nm and 586 nm (**Figures 3.3.4.1a** and **3.3.4.1c**). For the material that was thermally treated at 800 ˚C, is $Gd_{0.98}Nd_{0.02}Nb_2O_6$ for the excitation wavelength of λ_{ex} = 590 nm (**Figures 3.3.4.1d**).

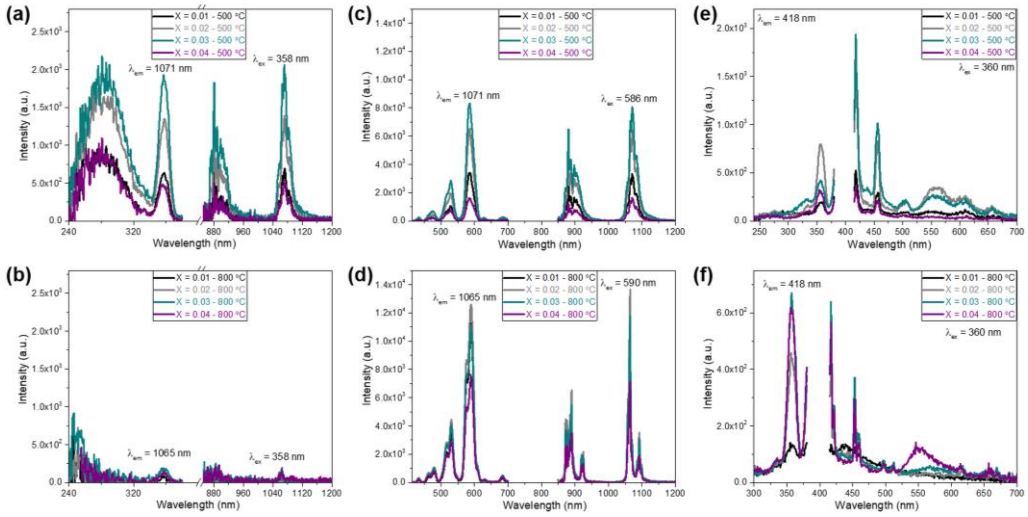

Figure 3.3.4.1. Excitation (240 – 380 nm and 415 – 700 nm) and emission (415 – 700 nm and 850 – 1200 nm) spectra of $Gd_{1-x}Nd_xNb_2O_6$ annealed at (a), (c), (e) 500 ˚C and (b), (d), (f) 800 ˚C.

The effect of water on the PL of the Nd^{3+} doped material is presented in **Figure 3.3.4.2**. For the $Gd_{1-x}Nd_xNb_2O_6$ (X = 0.02 and 0.03), excitation wavelength of λ_{ex} = 358 nm (annealed at 500 ˚C) the presence of water does not affect the PL emission intensity (**Figure 3.3.4.2a**). Nonetheless, for the excitation wavelength, λ_{ex} = 586 nm slight increase in the PL emission intensity is observed (**Figure 3.3.4.2c**). For the material annealed at 800 ˚C, a small increase in the

luminescence intensity is observed for the excitation wavelength of λ_{ex} = 358 nm (**Figure 3.3.4.2b**). The increase is by factors of 2.2 and 4.6 for $Gd_{0.98}Nd_{0.02}Nb_2O_6$ and $Gd_{0.97}Nd_{0.03}Nb_2O_6$, respectively, for λ_{ex} = 590 (**Figure 3.3.4.2d**). The emission spectra in the visible region is confirming the presence of a water-related peak (λ_{em} = 440 nm) for both annealing temperatures (500 ˚C and 800 ˚C) (**Figures 3.3.4.2e** and **3.3.4.2f**).

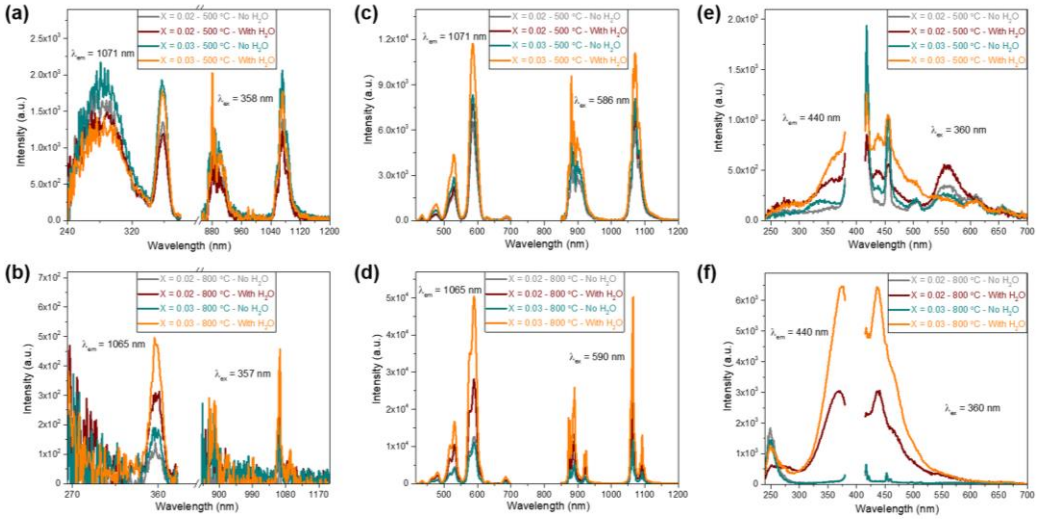

Figure 3.3.4.2. Excitation (240 – 380 nm and 415 – 700 nm) and emission (415 – 700 nm and 850 – 1200 nm) spectra of $Gd_{1-x}Nd_xNb_2O_6$ annealed at 500 ˚C (a), (c), (e) and 800 ˚C (b), (d), (f) with and without presence of water.

The PL spectra of the as-prepared $Gd_{1-x}Nd_xNb_2O_6$ (**Figures 3.3.4.3a** and **3.3.4.3c**) show that the emission intensity is very low for both excitation wavelengths λ_{ex} = 358 and 584 nm, for all doping concentrations. In addition, when the as-prepared material is excited with λ_{ex} = 360 nm (**Figure 3.3.4.3e**), mainly water-related peak (λ_{em} = 440 nm) is observed. The water-related peak is more intense for the $Gd_{0.96}Nd_{0.04}Nb_2O_6$ that musk the Nd^{3+}-related emission. For the $Gd_{0.97}Nd_{0.03}Nb_2O_6$, the water-related peak is less intense, and the λ_{em} = 418 and 457 nm Nd^{3+}-related emission peaks are observed. The PL emission and excitation spectra of the Nd^{3+} doped cube-like morphology annealed at 250 ˚C show a slight increase in the PL emission intensity for both excitation

wavelength λ_{ex} = 358 and 584 nm (**Figures 3.3.4.3b** and **3.3.4.3d**). The PL spectra for the excitation wavelength of λ_{ex} = 360 nm do not show the presence of the water-related peak (**Figure 3.3.4.3f**) for all doping concentrations (x = 1, 2, 3, and 4). For the $Gd_{0.99}Nd_{0.01}Nb_2O_6$, an intense emission from the matrix (niobium oxide groups) is detected. For the $Gd_{0.97}Nd_{0.03}Nb_2O_6$ the Nd^{3+}-related emission peaks at λ_{em} = 421, 453, 457, 498, and 512 nm are observed. Also, the Nd^{3+}-related excitation band centered at about λ_{ex} = 357 nm is detected (**Figure 3.3.4.3f**).

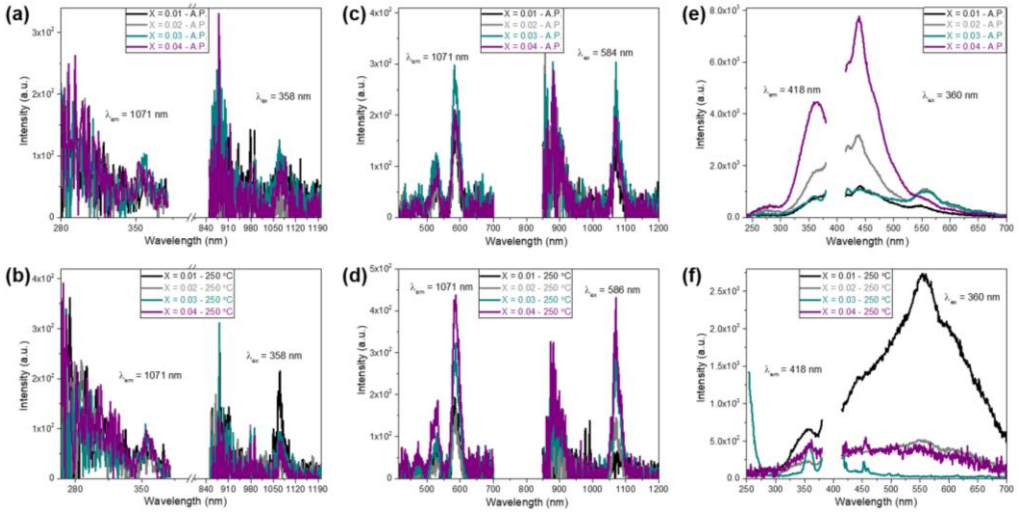

Figure 3.3.4.3. Excitation (240 – 380 nm and 415 – 700 nm) and emission (415 – 700 nm and 850 – 1200 nm) spectra of $Gd_{1-x}Nd_xNb_2O_6$ as-prepared (a), (c), (e) and annealed at 250 ˚C (b), (d), (f).

3.4. Mie Scattering

The morphology and the size distributions of the analyzed $GdNb_2O_6$ submicron particles are presented in **Figure 3.4.1**. The average particles size is the biggest for system S1 and the lowest for system S4 (S1 > S2 > S3 > S4), as presented in **Table 3.4.1**. The system S1 consists of bar-like particles, while the system S2 contains mainly cube-like particles and some bar-like particles. Systems S3 and S4 have a more homogeneous distribution of cube-like particles. In addition, systems S1 and S2 present similar size distribution. Nonetheless, for S1, the

amount of small particles is about 35 %, and the bigger particles are 65 %. On the contrary, for S2, the amount of small particles is about 60 %, and the bigger particles are 40 % (**Table 3.4.1**).

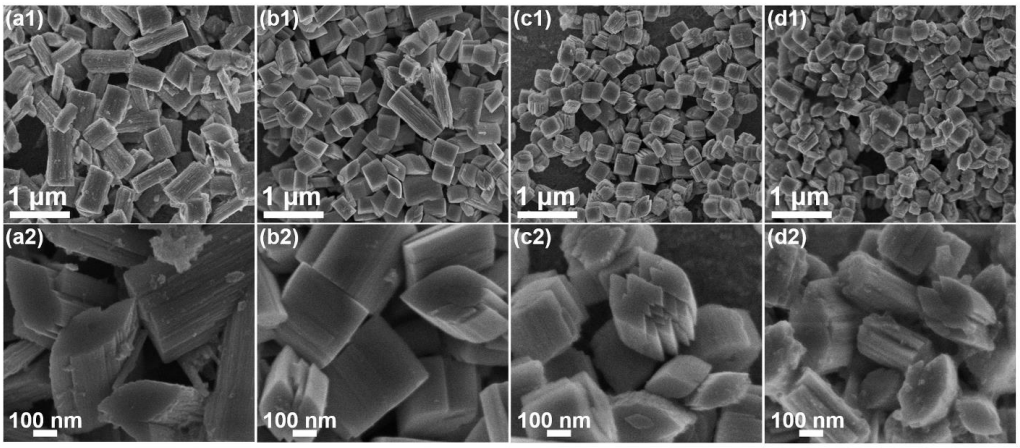

Figure 3.4.1. SEM images of sizes distribution and cross section of systems (a1), (a2) S1, (b1), (b2) S2, (c1), (c2) S3 and (d1), (d2) S4.

Table 3.4.1. Calculated (Calc.) average particle size with its weight in percentage, band gap, and refractive index of systems S1-S4.

System	Calc. Avg. particle size size1 (nm)	Weight size1 (%)	Calc. Avg. particle size size2 (nm)	Weight size2 (%)	Band gap (eV)	Refractive index n
S1	295 ± 60	35.0	500 ± 190	65.0	3.518	2.206
S2	330 ± 80	60.0	580 ± 150	40.0	3.545	2.199
S3	300 ± 40	60.0	560 ± 170	40.0	3.501	2.210
S4	240 ± 44	47.5	400 ± 200	52.5	3.560	2.195

Figure 3.4.2a depicts the experimental extinction spectra (Q_{ext}) of the four systems (S1-S4). All the spectra are a broad peak followed by a dip. The peak is blue-shifted with the decreased average particle size as predicted by Mie theory [61]. In addition, the dip is more pronounced for S3, where the particles size distribution is the most homogeneous. The absolute absorbance spectra (Q_{abs}, **Figures 3.4.3b-3.4.3f**) lack the broad peak component. This behavior

indicates that the broad peak is scattering-related [29,138]. It is possible to see from here that it is important to control the size of the particles. This control allows shifting Mie resonance to a different wavelength. As a result, the various sizes can be excited by a different wavelength to obtain lasing or enhanced luminescence [21,22].

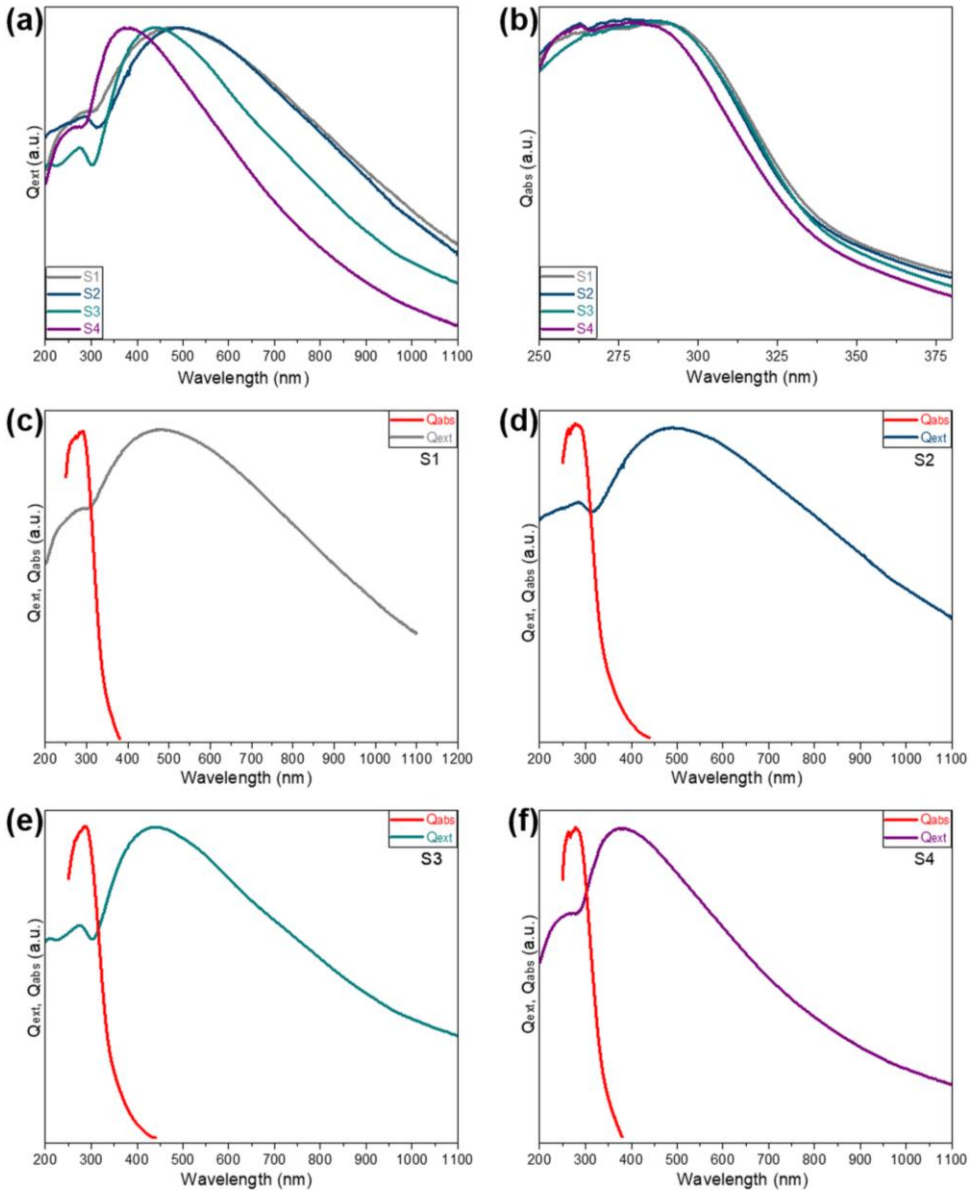

Figure 3.4.2. Experimental (a) extinction (Q_{ext}) and (b) absolute absorbance (Q_{abs}) spectra of systems S1-S4, and Q_{ext} and Q_{abs} of systems (c) S1, (d) S2 (e) S3, and (f) S4.

From **Figures 3.4.3a** and **3.4.3b**, it is possible to see that the particles size distribution of systems S1 and S2 measured from the SEM images coincides

with the calculated one (with two Gaussian functions). Whereas, for the systems S3 and S4 (**Figures 3.4.3c** and **3.4.3d**), the sizes around 600 nm are practically missing for the measured size distribution. Particles bigger than 600 nm in length were not observed in the SEM images. These sizes might result from small aggregates of two or three particles (**Figure 3.4.4**). In general, the maximum particle size (length) observed in the UV-Vis region of the extinction spectra (**Figure 3.4.2a**) for these $GdNb_2O_6$ particles is ~ 1000 nm.

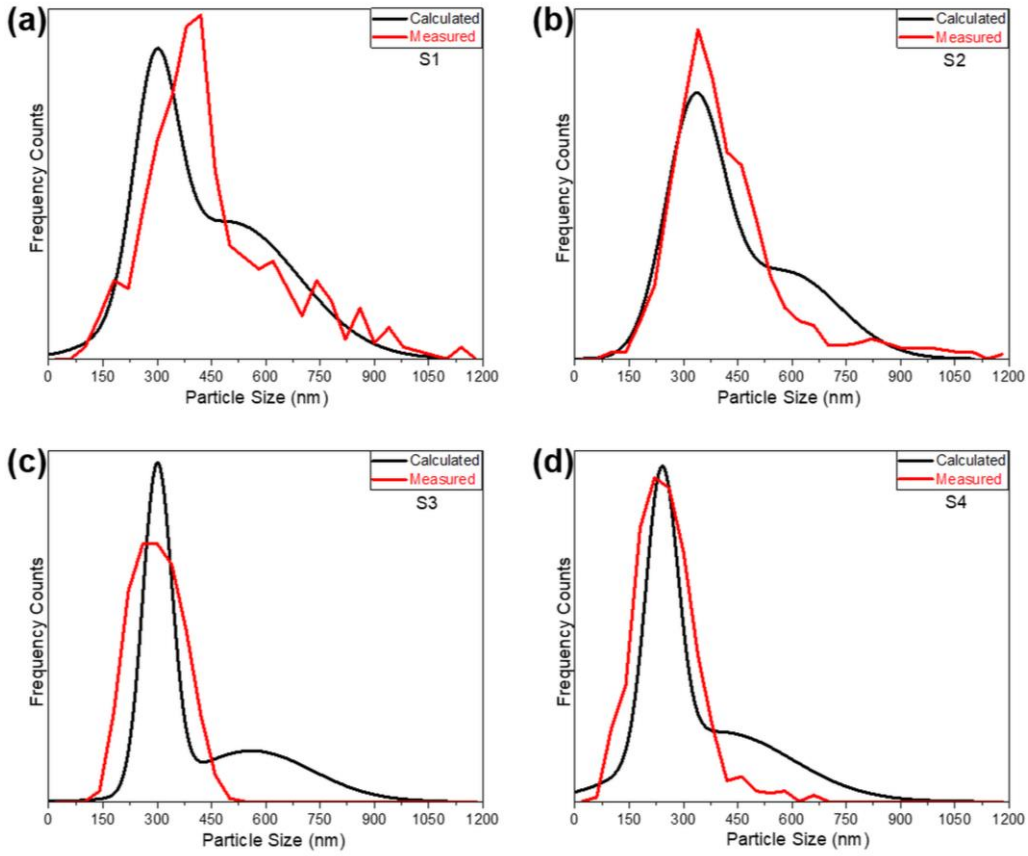

Figure 3.4.3. Calculated (with two Gaussian functions) and measured from SEM images (Measured) size distribution of systems (a) S1, (b) S2, (c) S3, and (d) S4.

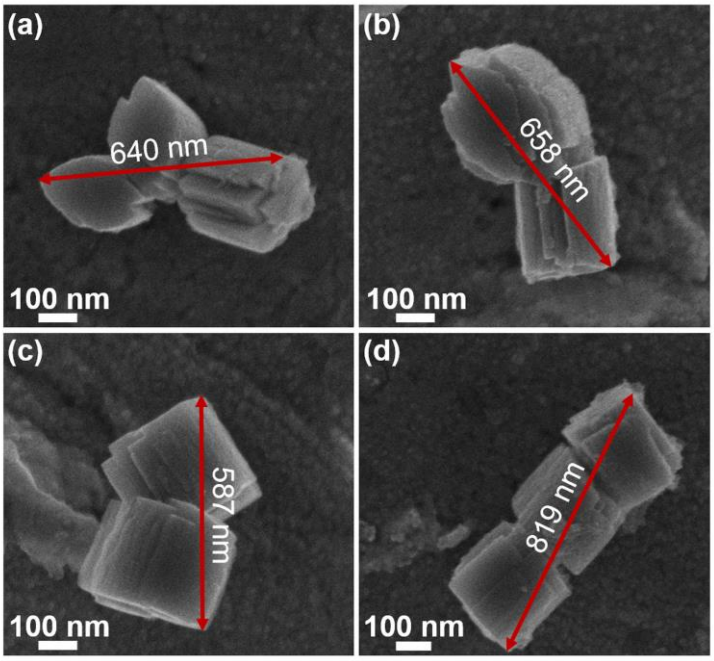

Figure 3.4.4. SEM images of two and three particles aggregates of a size (a) 640 nm, (b) 658 nm, (c) 587 nm, and (d) 819 nm.

In **Figure 3.4.5**, the comparison between the experimental and the calculated extinction spectra is presented. For the Mie-resonance of a single particle (Mie-1-Particle), a ripple structure is present (centered at the experimental extinction) [61]. This ripple structure vanishes when the Mie scattering is averaged with particles size distribution calculated with two Gaussian functions (Mie-2-Gaussian Size), where the experimental and calculated spectra overlap for all systems (**Figure 3.4.5**). For the measured size distribution, the experimental extinction is mainly overlapping with the calculated spectra (Mie-Measured Size). For systems S1 and S2, where the measured and calculated size distribution (two Gaussian functions) agree, the Mie-Measured Size and Mie-2-Gaussian Size spectra agree as well (**Figures 3.4.5a** and **3.4.5b**), as expected. Whereas, for systems S3 and S4, where the distribution of sizes with dimensions larger than 600 nm are missing, the Mie-Measured Size spectra only fit a part of the experimental one (**Figures 3.4.5c** and **3.4.5d**).

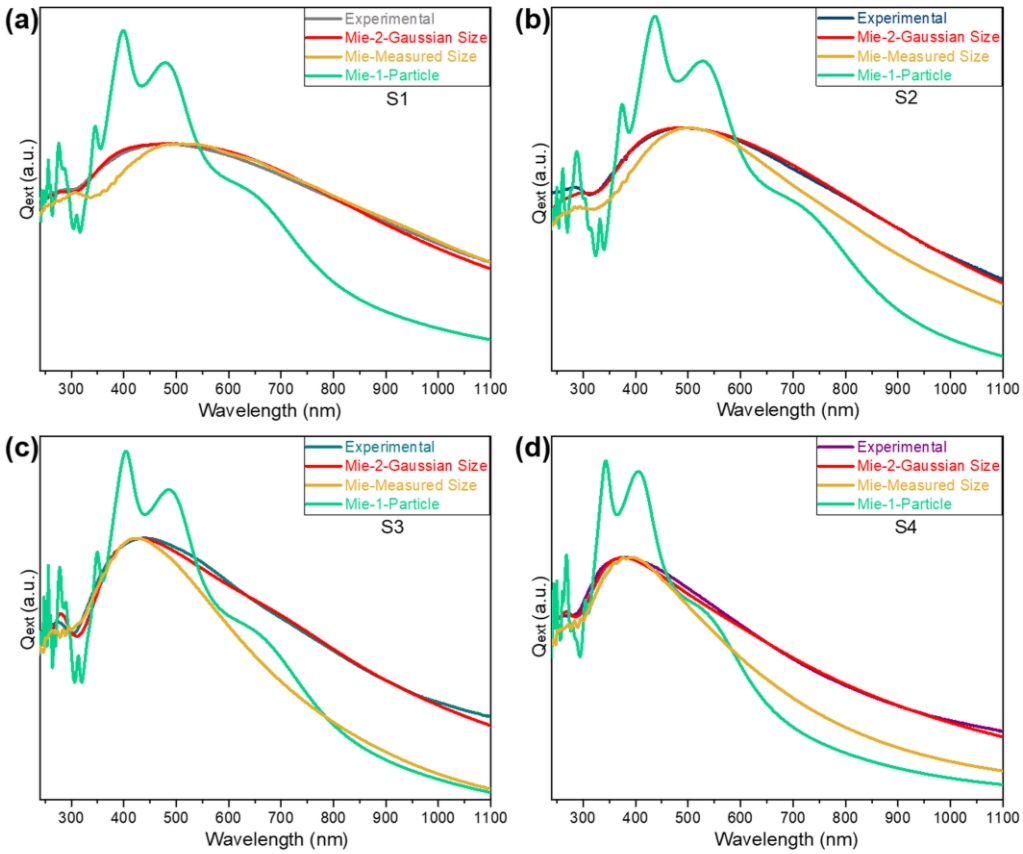

Figure 3.4.5. Measured (Experimental), calculated with two Gaussian functions (Mie-2-Gaussian Size), calculated with the measured size distribution (Mie-Measured Size), and calculated for one particle (Mie-1-Particle) extinction spectra of systems (a) S1, (b) S2, (c) S3, and (d) S4.

Extinction spectra of all systems (S1-S4) blue-shifted with the increased value of the refractive index, as predicted by the Mie theory (**Figure 3.4.6**).[61] When the refractive index of the media is getting closer to one of the particles, the scattering efficiency is getting smaller. These results are additional evidence that the broad peak in the extinction spectra is Mie scattering related. This behavior can assist in constructing lasing and luminescence enhanced systems. By tuning the refractive index, it is possible to obtain Mie resonance at different wavelengths.

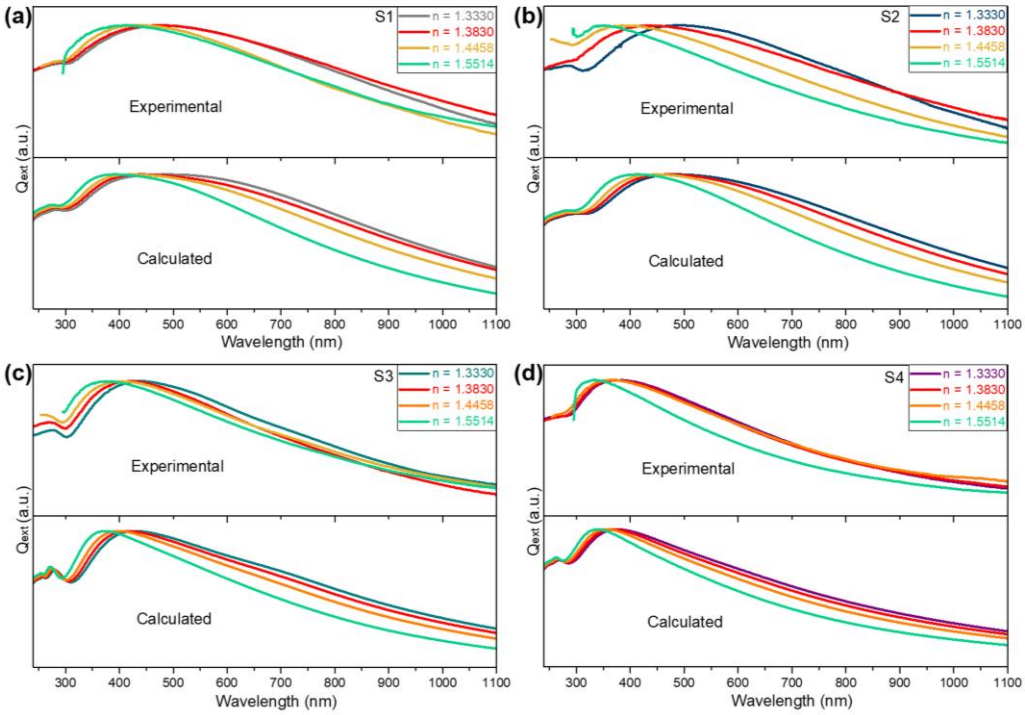

Figure 3.4.6. Measured (Experiment) and calculated with two Gaussian functions refractive index dependence extinction spectra for systems (a) S1, (b) S2, (c) S3, and (d) S4.

The extinction spectrum of a single particle with 300 nm size and the electric and magnetic dipole (ED, MD), quadrupole (EQ, MQ), and octopole (EO, MO) modes contributions are shown in **Figure 3.4.7**. In **Figure 3.4.7a**, it is possible to see that the extinction spectrum (Mie-1-Particle) contains multiple peaks. This appearance is termed ripple structure [61]. The dipole contribution is a sum of the magnetic and electric contributions (**Figure 3.4.7b**). Each mode sum (dipole = electric + magnetic) fits a peak in the extinction spectrum of a single particle (**Figure 3.4.7a**). The quadrupole and octopole contributions have similar behavior. **Figures 3.4.7b**, **3.4.7c**, and **3.4.7d** clearly show that the electric contribution is different from the magnetic one.

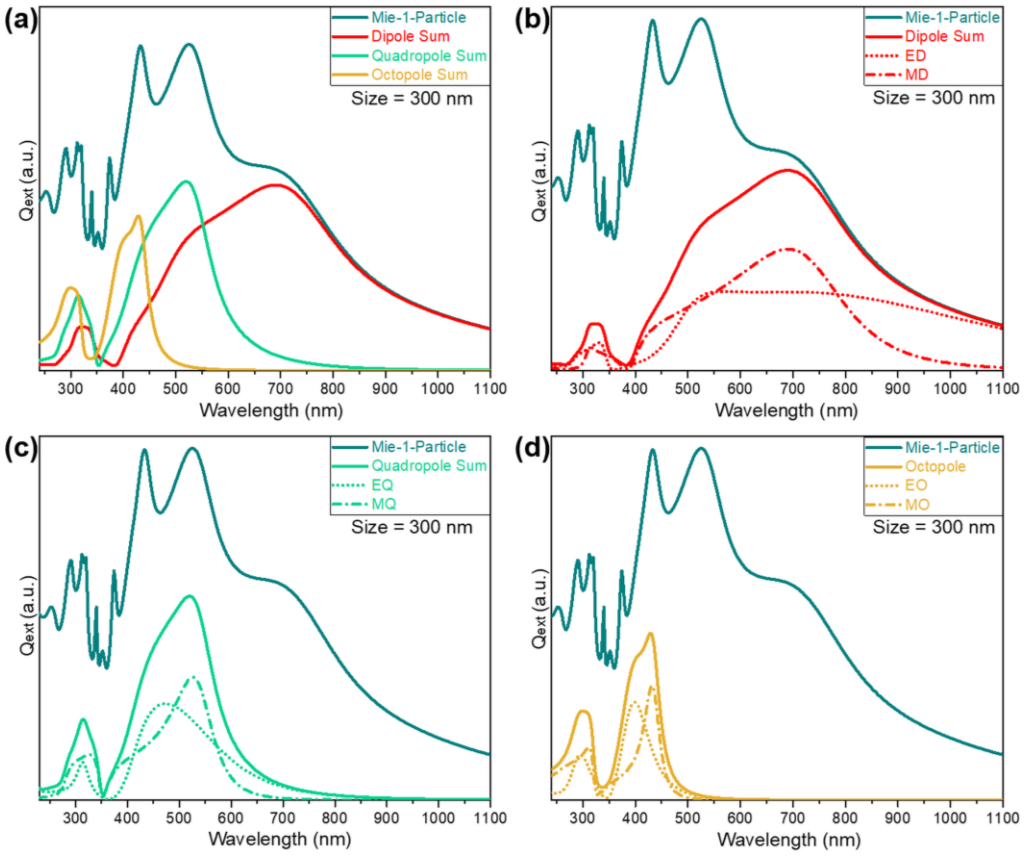

Figure 3.4.7. (a) The calculated extinction spectrum with a sum of an electric and magnetic (b) dipole (ED, MD), (c) quadrupole (EQ, MQ), and (d) octopole (EO, MO) contributions for a single-particle with a size of 300 nm.

The extinction spectrum calculated with the two Gaussian size distribution for S1 and the ED, MD, EQ, MQ, EO, and MO modes contribution are shown in **Figure 3.4.8**. In **Figure 3.4.8a**, it is possible to see that the extinction spectrum (Mie-2-Gaussian Size) does not contain multiple peaks as in the case of a single particle (**Figure 3.4.7**). **Figures 3.4.8b**, **3.4.8c**, and **3.4.8d** show that the electric contribution is similar to the magnetic one. Contrary to the single-particle case, what we see for the multiple-particle system is the superposition of contributions from all the particles of different sizes. Similar results are obtained for all the systems S1-S4. The calculations for system S3 are presented in **Figure 3.4.9** as an additional example.

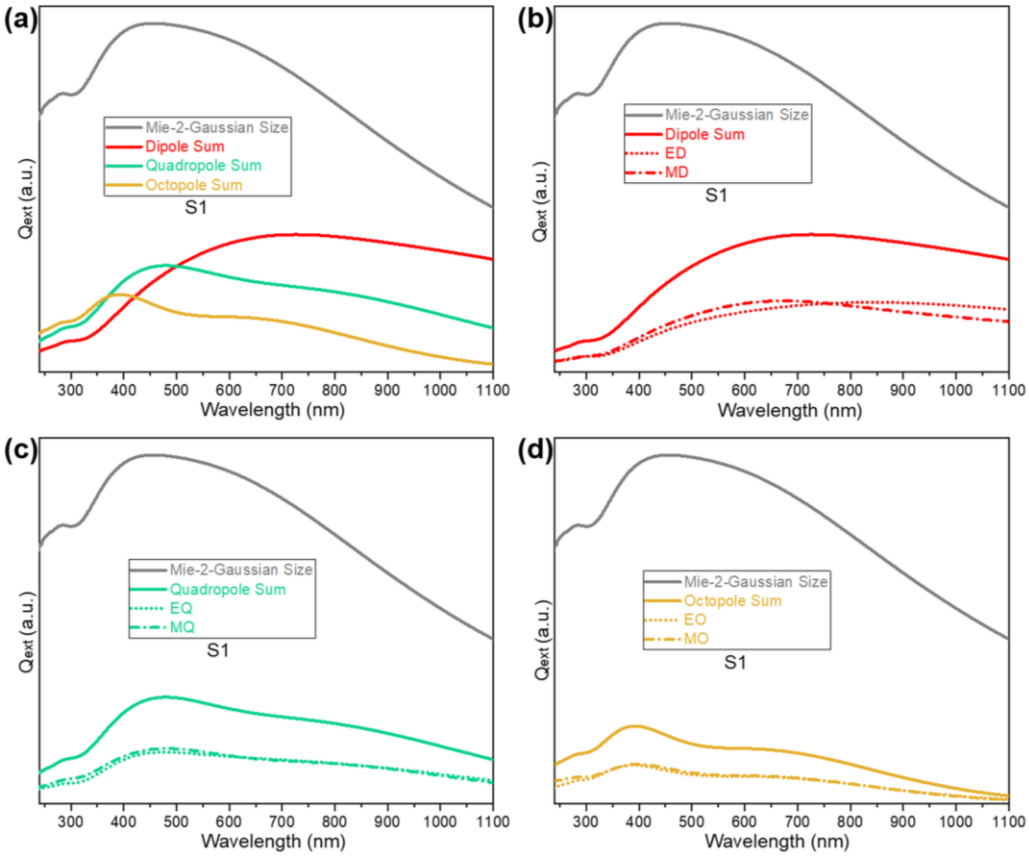

Figure 3.4.8. (a) The calculated extinction spectrum with a sum of an electric and magnetic (b) dipole (ED, MD), (c) quadrupole (EQ, MQ), and (d) octopole (EO, MO) contributions for multiple-particle case of a system S1.

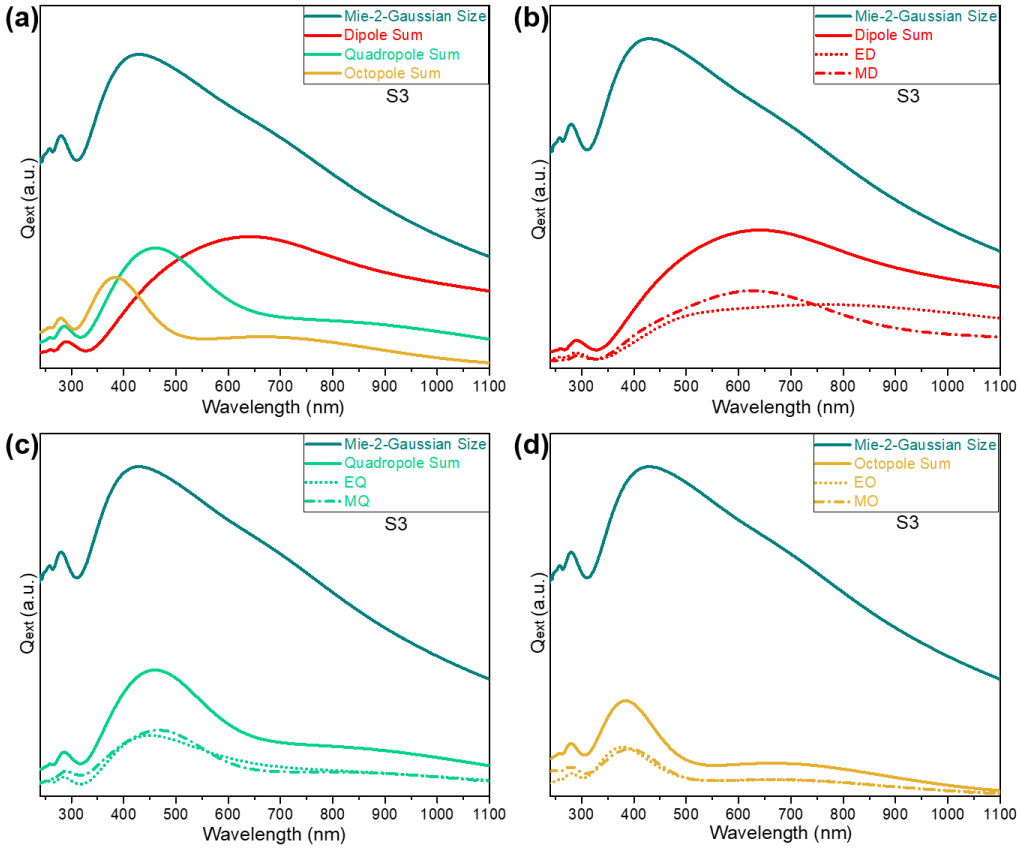

Figure 3.4.9. (a) The calculated extinction spectrum with a sum of an electric and magnetic (b) dipole (ED, MD), (c) quadrupole (EQ, MQ), and (d) octopole (EO, MO) contributions for multiple-particle case of a system S3.

3.5. Random Lasing

To check that $Gd_{0.97}Nd_{0.03}Nb_2O_6$ present random lasing behavior, the powders annealed at 500 ˚C and 800 ˚C ($Gd_{0.97}Nd_{0.03}Nb_yO_z$), are dispersed in PMMA media (**section 2.4**). The emission from the PMMA films is analyzed by excitation with increased pump energy of 808 nm laser. **Figure 3.5.1a** shows that for the powder that was annealed at 500 ˚C, the emission intensity is increased with the pump energy. It is clear from **Figure 3.5.1b** that this dependence is linear. The threshold is 4.50 W/cm^2, and at the pump energy of 27.67 W/cm^2, saturation is reached. The full width at half maximum (FWHM)

of this λ_{em} = 1071 nm emission peak is reduced with the increased pump energy (**Figure 3.5.1b**), characteristic of lasers action [139,140]. Also, for the Nd^{3+} doped powder annealed at 800 ˚C, a linear dependence of the λ_{em} = 1065 nm emission with the increased pump energy is observed. For this material, the threshold is about 16.10 W/cm^2, and the saturation is not reached for the maximum pump energy of 31.5 W/cm^2. For material annealed at 800 ˚C, the emission peak is narrower (FWHM = 4.93 nm) compared to material annealed at 500 ˚C (FWHM = 20.00 nm).

Analysis of the extinction spectra of the Nd^{3+} doped cube-like morphology in the PMMA media (**Figure 3.5.2**) shows that the spectrum of the powder annealed at 800 ˚C is broader (**Figure 3.5.2b**) compared to the material annealed at 500 ˚C (**Figure 3.5.2a**). The scattering efficiency is higher for this material (annealed 800 ˚C) at the 808 nm wavelength (**Figure 3.5.2b**). The 1071 and 1065 nm emissions for the materials annealed at 500 ˚C and 800 ˚C, respectively, overlap with the Mie scattering at these wavelengths (**Figure 3.5.2**). Hence, possibly the random lasing action of Nd^{3+} doped cube-like morphology in PMMA media is due to this overlap (**Figure 3.5.2**). The random lasing action is most likely due to the Purcell effect where a radiative dipole is placed in a resonance cavity [75]. The resonance cavity modifies the local density of optical states (LDOS), and it is proportional to the absolute squared local electric field of the cavity normalized to the incident intensity. In the resonance cavity, the peak of the LDOS is at the resonance wavelength, and dipole emits into this mode at a high rate. The cavity can reradiate this energy, and the dipole emission is enhanced. When the scattering spectrum of the NP's overlaps with the fluorophore emission (as in our case, **Figure 3.5.2**), the emission is enhanced due to the variation in the LDOS [75].

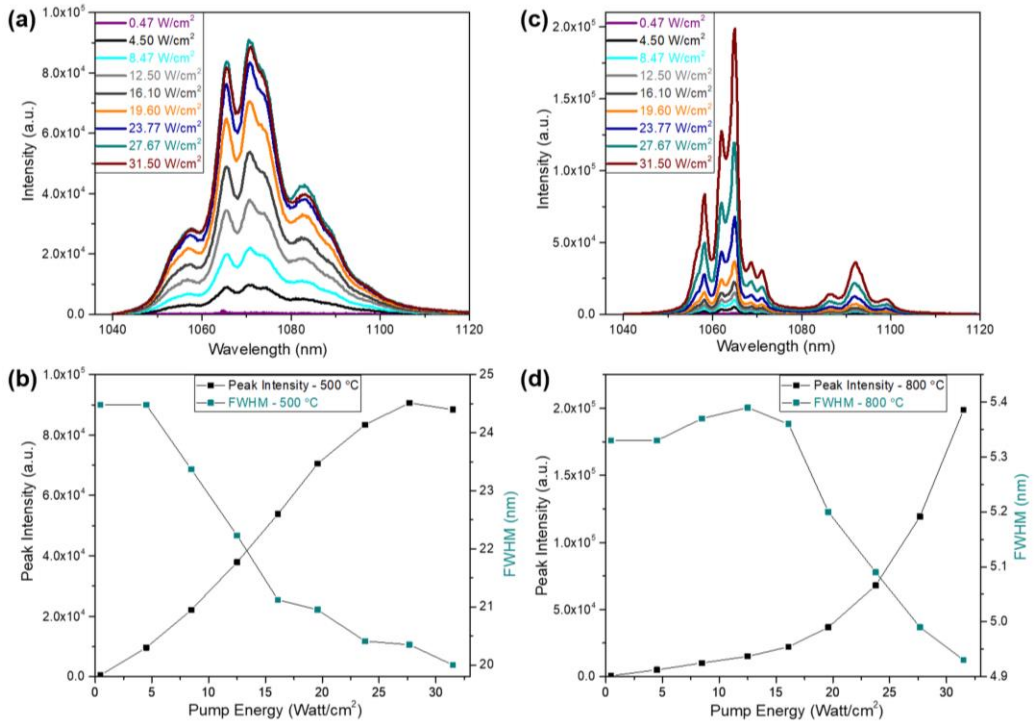

Figure 3.5.1. NIR emission dependence on the power of λ_{ex} = 808 nm laser and the FWHM for $Gd_{0.97}Nd_{0.03}Nb_2O_6$ annealed at (a), (b) 500 ˚C and (c), (d) 800 ˚C.

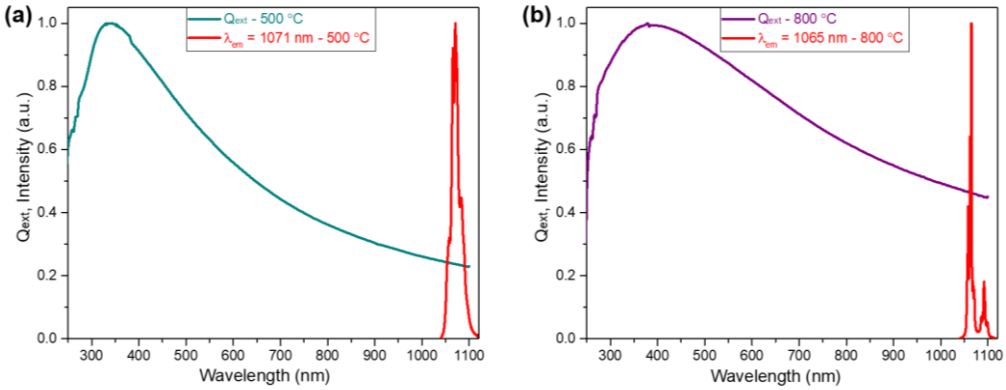

Figure 3.5.2. Extinction and emission spectra of Nd^{3+} doped cube-like morphology annealed at (a) 500 ˚C and (b) 800 ˚C dispersed in PMMA.

4. Conclusions

In the current work, the $GdNb_2O_6$, $Gd_{1-x}Tm_xNb_2O_6$, and $Gd_{1-x}Nd_xNb_2O_6$ compounds are synthesized for the first time. Various morphologies such as bar-, cube-, and flower-like are obtained without the addition of any surfactant. The nucleation mechanism is similar to the one of zeolites and barite roses. The morphology was strictly controlled by pH and a narrow temperature range (≤ 1 ˚C) during the KOH addition to the precursors' solution.

These compounds are isomorphic of the aeschynite-type orthorhombic $EuTiNbO_6$ with a *Pnma* (62) space group. For the flower-like morphology, a mixed $GdNb_2O_6/GdNbO_4$ phase is formed, as confirmed by XRD and Raman analyses.

The FTIR analysis shows that OH^- groups remain attached to the $GdNb_2O_6$ nanostructures' surface even after annealing at elevated temperatures such as 800 ˚C. In addition, Raman and XPS analyses confirm the presence of both Nb^{+4} and Nb^{+5} species in the as-prepared $GdNb_2O_6$ and $GdNb_2O_6/GdNbO_4$ nanostructures. Therefore, charge compensation is expected by the OH^- groups at the surface and the Nb^{+4} and Nb^{+5} species in the bulk.

These compounds are indirect band gap (Eg) materials with optical Eg values of 3.52 – 3.63 eV and 3.48 – 3.58 eV before and after water elimination, respectively. The Eg value increased slightly with the change in the morphology (flower > cubes > bars). This behavior is strain-related for bars and cubes.

The $GdNb_2O_6$ surface-water interactions are analyzed by photoluminescence (PL). The PL varies between the morphologies before and after surface water elimination. Intrinsic PL emission of $GdNb_2O_6$ appears as broadband between 400 – 700 nm. Whereas, $GdNb_2O_6$ surface-water interactions lead to an intense blue emission centered at about λ_{em} = 440 nm. This emission is a direct result of the overlap between the excitation bands of $GdNb_2O_6$ and water. In addition, a color change is observed for all morphologies after annealing at low temperature (250 ˚C) for 16 h.

Thulium doped $GdNb_2O_6$ ($Gd_{1-x}Tm_xNb_2O_6$) present a characteristic thulium λ_{em} = 457 nm blue emission when excited with λ_{ex} = 361 nm. This emission is partially water-assisted. Hence, thermal treatment is not necessary to obtain emission from Tm^{3+} ions ($^1D_2 \rightarrow {}^3F_4$ transitions) in the $Gd_{1-x}Tm_xNb_2O_6$ compounds.

The PL properties of Nd^{3+} doped $GdNb_2O_6$ cube-like morphology are also studied. In this case, two annealing temperatures are analyzed, 500 ˚C and 800 ˚C. When the material is excited with a visible light (λ_{ex} = 586 and 590 nm), an efficient emission in the NIR region is observed for both annealing temperatures. For the excitation wavelength of λ_{ex} = 358 nm (UV), the optical emission is present only for $Gd_{1-x}Nd_xNb_2O_6$ annealed at 500 ˚C. Nevertheless, the emission intensity for the material annealed at 800 ˚C is higher compared to annealing at 500 ˚C (λ_{ex} = 586 and 590 nm). In addition, the emissions are centered at λ_{em} = 1071 and 881 nm, and λ_{em} = 1065 and 890 nm, for the annealing at 800 ˚C and 500 ˚C, respectively. The λ_{em} = 1065 and 890 nm emissions are characteristic of monoclinic $GdNbO_4$. The XRD shows that after annealing at 800 ˚C, the crystalline structure is mainly $Gd_{1-x}Nd_xNb_2O_6$. The best Nd^{3+} doped materials are $Gd_{0.98}Nd_{0.02}Nb_2O_6$ and $Gd_{0.97}Nd_{0.03}Nb_2O_6$ for the annealing at 800 ˚C and 500 ˚C temperatures, respectively. Also, for this doping presence of water trapped in the structure affects the optical emission. For the material annealed at 800 ˚C, a small increase in the luminescence intensity is observed for the excitation wavelength of λ_{ex} = 358 nm. Nonetheless, for the excitation wavelength of λ_{ex} = 590, the enhancement is by factors of 2.2 and 4.6 for $Gd_{0.98}Nd_{0.02}Nb_2O_6$ and $Gd_{0.97}Nd_{0.03}Nb_2O_6$, respectively.

Mie scattering phenomenon in the intrinsic $GdNb_2O_6$ bar- and cube-like morphologies is investigated by the experimental and the theoretical means. The presence of the Mie scattering is proven by comparison the extinction and the absolute absorption spectra. Also, it is shown that the extinction spectra are blue-shifted with the decreased particles size and increased refractive index, as predicted by the Mie theory. The experimental extinction spectra are fitted with the calculated (Mie-2-Gaussian) and measured size distributions. The calculated

size distribution has a better fit. Using the Mie theory, it is also possible to calculate the different modes that contribute to the scattering, such as dipole, quadrupole, and octopole. For the multi-particle case, these modes are a superposition of all the modes contributions from all the particles sizes.

The $Gd_{0.97}Nd_{0.03}Nb_2O_6$ cube-like morphology embedded in the PMMA media is tested as a random laser. Materials annealed at both 500 ˚C and 800 ˚C show lasing action. For both temperatures, the emission intensity is increased, and FWHM is decreased with the increased pump energy. For the material annealed at 500 ˚C, the threshold is 4.50 W/cm^2, and at the pump energy of 27.67 W/cm^2, saturation is reached. For the Nd^{3+} doped powder annealed at 800 ˚C, the threshold is about 16.10 W/cm^2, and the saturation is not reached for the maximum pump energy of 31.5 W/cm^2. Also, for material annealed at 800 ˚C, the emission peak is narrower (FWHM = 4.93 nm) compared to material annealed at 500 ˚C (FWHM = 20.00 nm).

The current study suggests that $GdNb_2O_6$, $Gd_{1-x}Tm_xNb_2O_6$, and $Gd_{1-x}Nd_xNb_2O_6$ compounds can be potentially incorporated in humidity sensors and optical applications, such as light-emitting diodes and random lasers.

5. Future Work

1. To publish on the Nd^{3+} doping and the Mie scattering phenomenon (**sections 3.3**, **3.4**, and **3.5**).
2. To test the Tm^{3+} doped ($Gd_{1-x}Tm_xNb_2O_6$) cube- and bar-like morphologies as random lasers.
3. To dope the bar- and flower-like morphologies with Nd^{3+} ($Gd_{1-x}Nd_xNb_2O_6$) and compare their PL characteristics with the ones of the cube-like morphology studied in the current work.
4. It will be interesting to test different polymeric media as a host for the $Gd_{1-x}Tm_xNb_2O_6$ and $Gd_{1-x}Nd_xNb_2O_6$ materials for random lasers application. It is shown in the current study (**sections 3.4**) that the refractive index affects the scattering efficiency. The lower the refractive index, the more scattering is observed for the cubes and bars. Hence, a polymeric matrix with the lowest refractive index most likely will lead to more scattering and more efficient random laser action.
5. The Gd^{3+} [141,142] and Nd^{3+} [143] ions based materials are famous by their unique magnetic properties. Thus, it is important to study the magnetic properties of the doped and undoped gadolinium niobates synthesized in the current work.
6. It is shown in the current work that the surface water attached to the $Gd_{1-x}RE_xNb_2O_6$ (RE = Tm^{3+}, Nd^{3+}) surface affects the PL emission of these nanoscale materials. Consequently, replacing this water with antennas and other functional groups such as PBH [144], carboxylic groups, PEG, PAH, PSS, *etc*.[145,146] might lead to optical emission enhancement. Also, encapsulating these $Gd_{1-x}RE_xNb_2O_6$ submicron materials with a polymeric matrix might prevent water reabsorption.

6. Publication

[1] A. Sedova, M.M. Tellez-Cruz, C. Falcony, Pristine and humidity-related photoluminescence in gadolinium niobate nanophosphors synthesized at low temperatures, Mater. Res. Bull. (2021) 111600.

7. References

[1] G.K. Ong, C.A. Saez Cabezas, M.N. Dominguez, S.L. Skjærvø, S. Heo, D.J. Milliron, Electrochromic niobium oxide nanorods, Chem. Mater. 32 (2019) 468–475.

[2] J. Meng, Q. He, L. Xu, X. Zhang, F. Liu, X. Wang, Q. Li, X. Xu, G. Zhang, C. Niu, Identification of Phase Control of Carbon-Confined Nb2O5 Nanoparticles toward High-Performance Lithium Storage, Adv. Energy Mater. 9 (2019) 1802695.

[3] V. Ojha, K. Kato, M.A. Kabbani, G. Babu, P.M. Ajayan, Nb2O5/reduced graphene oxide nanocomposite anode for high power hybrid supercapacitor applications, ChemistrySelect. (2019) 1098–1102.

[4] C. Zhou, R. Shi, G.I.N. Waterhouse, T. Zhang, Recent advances in niobium-based semiconductors for solar hydrogen production, Coord. Chem. Rev. 419 (2020) 213399.

[5] N.-D. Kohlenbach, C. Kijatkin, M. König, M. Haase, M. Imlau, K. Kömpe, The role of cations in hydrothermal synthesis of nonlinear optical sodium niobate nanocrystals, Nanoscale. 12 (2020) 19223–19229.

[6] A.M. Hamilton, S. O'Donnell, B. Zoellner, I. Sullivan, P.A. Maggard, Flux-mediated synthesis and photocatalytic activity of NaNbO3 particles, J. Am. Ceram. Soc. 103 (2020) 454–464.

[7] Y. Repelin, E. Husson, H. Brusset, Etude par spectroscopies d'absorption ir et de diffusion Raman des composés AIIBV2O6 de structure de type "blocs 1× 2"—I. Etude du niobate de baryum BaNb2O6, Spectrochim. Acta Part A Mol. Spectrosc. 35 (1979) 937–948.

[8] I.-S. Cho, S.T. Bae, D.H. Kim, K.S. Hong, Effects of crystal and electronic structures of ANb2O6 (A= Ca, Sr, Ba) metaniobate compounds on their photocatalytic H2 evolution from pure water, Int. J. Hydrogen Energy. 35 (2010) 12954–12960.

[9] K.L. Keester, R.R. Neurgaonkar, T.C. Lim, E.J. Staples, Strontium metaniobate: Its crystallography, polymorphism, and isomerism, Mater. Res. Bull. 15 (1980) 821–826.

[10] H.P. Beck, A study on AB2O6 compounds, Part III: Co-ordination needs and patterns of connectivity, Zeitschrift Für Krist. Mater. 228 (2013) 271–288.

[11] M. Zeng, J. Liu, H. Yu, M. Chao, B. Tang, S. Zhang, NiNb2O6-BaTiO3 Ceramics for Energy-Storage Capacitors, Energy Technol. 6 (2018) 899–905.

[12] Y. Zhou, Z. Qiu, M. Lü, Q. Ma, A. Zhang, G. Zhou, H. Zhang, Z. Yang, Photoluminescence characteristics of pure and Dy-doped ZnNb2O6 nanoparticles prepared by a combustion method, J. Phys. Chem. C. 111 (2007) 10190–10193.

[13] A. Kormányos, A. Thomas, M.N. Huda, P. Sarker, J.P. Liu, N. Poudyal, C. Janáky, K. Rajeshwar, Solution combustion synthesis, characterization, and photoelectrochemistry of CuNb2O6 and ZnNb2O6 nanoparticles, J. Phys. Chem. C. 120 (2016) 16024–16034.

[14] M. Hirano, K. Ishikawa, Concentration dependence of luminescence properties of GdNbO4: Er3+/Yb3+ synthesized through hydrothermal route, J. Alloys Compd. 709 (2017) 64–71.

[15] X. Liu, C. Chen, S. Li, Y. Dai, H. Guo, X. Tang, Y. Xie, L. Yan, Host-Sensitized and Tunable Luminescence of GdNbO4: Ln3+ (Ln3+= Eu3+/Tb3+/Tm3+) Nanocrystalline Phosphors with Abundant Color, Inorg. Chem. 55 (2016) 10383–10396.

[16] A. Dwivedi, K. Mishra, S.B. Rai, Multi-modal luminescence properties of RE3+ (Tm3+, Yb3+) and Bi3+ activated GdNbO4 phosphors—upconversion, downshifting and quantum cutting for spectral conversion, J. Phys. D. Appl. Phys. 48 (2015) 435103.

[17] M. Hirano, M. Hara, Formation and luminescence properties of GdTiNbO6: Er3+/Yb3+ through the hydrothermal route, J. Ceram. Soc. Japan. 126 (2018) 178–183.

[18] A. Dwivedi, A.K. Singh, S.B. Rai, Down-shifting and upconversion photoluminescence in Ho3+/Yb3+ codoped GdNbO4: effect of the Bi3+ ion and the magnetic field, Dalt. Trans. 43 (2014) 15906–15914.

[19] G.S.R. Raju, E. Pavitra, H. Lee, G. Nagaraju, R. Baskaran, S.G. Yang, C.H. Kwak, G.P. Nagaraju, Y.S. Huh, Y.-K. Han, Pre-ouzo effect derived fergusonite gadolinium ortho-niobate mesoporous nanospheroids for multimodal bioimaging and photodynamic therapy, Appl. Surf. Sci. 505 (2020) 144584.

[20] Y. Lu, X. Tang, L. Yan, K. Li, X. Liu, M. Shang, C. Li, J. Lin, Synthesis and luminescent properties of GdNbO4: RE3+ (RE= Tm, Dy) nanocrystalline phosphors via the sol–gel process, J. Phys. Chem. C. 117 (2013) 21972–21980.

[21] E. Tiguntseva, K. Koshelev, A. Furasova, P. Tonkaev, V. Mikhailovskii, E. V Ushakova, D.G. Baranov, T. Shegai, A.A. Zakhidov, Y. Kivshar, Room-temperature lasing from Mie-resonant nonplasmonic nanoparticles, ACS Nano. 14 (2020) 8149–8156.

[22] E.Y. Tiguntseva, G.P. Zograf, F.E. Komissarenko, D.A. Zuev, A.A. Zakhidov, S. V Makarov, Y.S. Kivshar, Light-emitting halide

perovskite nanoantennas, Nano Lett. 18 (2018) 1185–1190.

[23] S. Kruk, Y. Kivshar, Functional meta-optics and nanophotonics governed by Mie resonances, ACS Photonics. 4 (2017) 2638–2649.

[24] T. Okazaki, H. Sugimoto, T. Hinamoto, M. Fujii, Color Toning of Mie Resonant Silicon Nanoparticle Color Inks, ACS Appl. Mater. Interfaces. 13 (2021) 13613–13619.

[25] P.A. Dmitriev, D.G. Baranov, V.A. Milichko, S. V Makarov, I.S. Mukhin, A.K. Samusev, A.E. Krasnok, P.A. Belov, Y.S. Kivshar, Resonant Raman scattering from silicon nanoparticles enhanced by magnetic response, Nanoscale. 8 (2016) 9721–9726.

[26] H. Sugimoto, T. Okazaki, M. Fujii, Mie resonator color inks of monodispersed and perfectly spherical crystalline silicon nanoparticles, Adv. Opt. Mater. 8 (2020) 2000033.

[27] F. Timpu, A. Sergeyev, N.R. Hendricks, R. Grange, Second-harmonic enhancement with Mie resonances in perovskite nanoparticles, ACS Photonics. 4 (2017) 76–84.

[28] J.R.G. Navarro, M.H. V Werts, Resonant light scattering spectroscopy of gold, silver and gold–silver alloy nanoparticles and optical detection in microfluidic channels, Analyst. 138 (2013) 583–592.

[29] L. Yadgarov, C.L. Choi, A. Sedova, A. Cohen, R. Rosentsveig, O. Bar-Elli, D. Oron, H. Dai, R. Tenne, Dependence of the absorption and optical surface plasmon scattering of MoS2 nanoparticles on aspect ratio, size, and media, ACS Nano. 8 (2014) 3575–3583. https://doi.org/10.1021/nn5000354.

[30] S. Ishii, K. Chen, H. Okuyama, T. Nagao, Resonant optical absorption and photothermal process in high refractive index germanium nanoparticles, Adv. Opt. Mater. 5 (2017) 1600902.

[31] S. Jahani, Z. Jacob, All-dielectric metamaterials, Nat. Nanotechnol. 11

(2016) 23–36.

[32] K. Binnemans, Lanthanide-based luminescent hybrid materials, Chem. Rev. 109 (2009) 4283–4374.

[33] H. Dong, L.-D. Sun, C.-H. Yan, Energy transfer in lanthanide upconversion studies for extended optical applications, Chem. Soc. Rev. 44 (2015) 1608–1634.

[34] X. Huang, S. Han, W. Huang, X. Liu, Enhancing solar cell efficiency: the search for luminescent materials as spectral converters, Chem. Soc. Rev. 42 (2013) 173–201.

[35] K. Mishra, S.K. Singh, A.K. Singh, M. Rai, B.K. Gupta, S.B. Rai, New perspective in garnet phosphor: low temperature synthesis, nanostructures, and observation of multimodal luminescence, Inorg. Chem. 53 (2014) 9561–9569.

[36] K. Byrappa, T. Adschiri, Hydrothermal technology for nanotechnology, Prog. Cryst. Growth Charact. Mater. 53 (2007) 117–166.

[37] K. Byrappa, M. Yoshimura, Handbook of hydrothermal technology, William Andrew, 2013.

[38] R.I. Walton, Subcritical solvothermal synthesis of condensed inorganic materials, Chem. Soc. Rev. 31 (2002) 230–238.

[39] F. Pirajno, Hydrothermal processes and mineral systems, Springer Science & Business Media, 2009.

[40] G. Brunner, Hydrothermal and supercritical water processes, Elsevier, 2014.

[41] X. Qi, C.-M. Liu, C.-C. Kuo, Pr3+ doped LaTiNbO6 as a single phosphor for white LEDs, J. Alloys Compd. 492 (2010) L61–L63.

[42] X. Qi, R. Illingworth, H.G. Gallagher, T.P.J. Han, B. Henderson, Potential laser gain media with the stoichiometric formula RETiNbO6,

J. Cryst. Growth. 160 (1996) 111–118.

[43] M. Hirano, Y. Takagi, Phase transition and luminescence properties of GdTiNbO6: Eu3+ formed by hydrothermal route, Mater. Res. Bull. 105 (2018) 13–20.

[44] J. Zhang, R. Zuo, Raman scattering and infrared reflectivity study of orthorhombic/monoclinic LaTiNbO6 microwave dielectric ceramics by A/B-site substitution, Ceram. Int. 44 (2018) 16191–16198.

[45] M. Hirano, S. Kondo, S. Sato, Mild hydrothermal formation and comparative coprecipitation route for EuTiNbO6 fine phosphor, Ceram. Int. 42 (2016) 8240–8246.

[46] S.A. Mather, P.K. Davies, Nonequilibrium phase formation in oxides prepared at low temperature: Fergusonite-related phases, J. Am. Ceram. Soc. 78 (1995) 2737–2745.

[47] K.P.F. Siqueira, R.L. Moreira, A. Dias, Synthesis and crystal structure of lanthanide orthoniobates studied by vibrational spectroscopy, Chem. Mater. 22 (2010) 2668–2674.

[48] G. Blasse, A. Bril, Luminescence phenomena in compounds with fergusonite structure, J. Lumin. 3 (1970) 109–131.

[49] M. Yang, X. Liu, T. Hou, L. Du, Q. Wang, B. Chang, B. Li, J. Liu, G. Deng, I. V Kityk, Synthesis and luminescent properties of GdNbO4: Bi3+ phosphors via high temperature high pressure, J. Alloys Compd. 723 (2017) 1–8.

[50] S. Ding, H. Zhang, Q. Zhang, Y. Chen, R. Dou, F. Peng, W. Liu, D. Sun, Experimental and first principle study of the structure, electronic, optical and luminescence properties of M-type GdNbO4 phosphor, J. Solid State Chem. 262 (2018) 87–93.

[51] S. Ding, H. Zhang, Y. Chen, Q. Zhang, R. Dou, W. Liu, G. Sun, D. Sun, Structure, electronic and optical properties of LaNbO4: An

experimental and first-principles study, Solid State Commun. 277 (2018) 7–12.

[52] S. Ding, F. Peng, Q. Zhang, J. Luo, W. Liu, D. Sun, R. Dou, J. Gao, G. Sun, M. Cheng, Crystal growth, spectral properties, and continuous wave laser operation of Nd: GdNbO4, J. Alloys Compd. 693 (2017) 339–343.

[53] R. Yan, X. Li, W. Yao, Y. Shen, Z. Zhou, F. Peng, Q. Zhang, R. Dou, J. Gao, 926 nm laser operation in Nd: GdNbO4 crystal based on 4F3/2→ 4I9/2 transition, Opt. Laser Technol. 101 (2018) 515–519.

[54] P.K. Shahi, P. Singh, S.B. Rai, A. Bahadur, Host-sensitized NIR quantum cutting emission in Nd3+ doped GdNbO4 phosphors and effect of Bi3+ ion codoping, Inorg. Chem. 55 (2016) 1535–1541.

[55] M. Yang, X. Zhao, Y. Ji, F. Liu, W. Liu, J. Sun, X. Liu, Hydrothermal approach and luminescent properties for the synthesis of orthoniobates GdNbO4: Ln 3+(Ln= Dy, Eu) single crystals under high-temperature high-pressure conditions, New J. Chem. 38 (2014) 4249–4257.

[56] M. Hirano, K. Ishikawa, Direct synthesis of nanocrystalline GdNbO4 and GdNbO4-based phosphors doped with Eu 3+ through hydrothermal route, J. Ceram. Soc. Japan. 124 (2016) 42–48.

[57] G. Will, Powder diffraction: The Rietveld method and the two stage method to determine and refine crystal structures from powder diffraction data, Springer Science & Business Media, 2006.

[58] R.A. Young, The rietveld method, 1993.

[59] B.H. Toby, R factors in Rietveld analysis: How good is good enough?, Powder Diffr. 21 (2006) 67–70.

[60] M.I. Mishchenko, L.D. Travis, A.A. Lacis, Scattering, absorption, and emission of light by small particles, Cambridge University Press, 2002.

[61] C.F. Bohren, D.R. Huffman, Absorption and scattering of light by small

particles, John Wiley & Sons, Inc., 1998.

[62] M.H. Nayfeh, Fundamentals and Applications of Nano Silicon in Plasmonics and Fullerines: Current and Future Trends, Elsevier, 2018.

[63] G. Blasse, B.C. Grabmaier, A general introduction to luminescent materials, in: Lumin. Mater., Springer, 1994: pp. 1–9.

[64] K.F. Renk, Basics of laser physics, Springer, 2012.

[65] H. Cao, Lasing in random media, Waves in Random Media. 13 (2003) R1–R39.

[66] F. Luan, B. Gu, A.S.L. Gomes, K.-T. Yong, S. Wen, P.N. Prasad, Lasing in nanocomposite random media, Nano Today. 10 (2015) 168–192.

[67] H. Cao, Y.G. Zhao, S.T. Ho, E.W. Seelig, Q.H. Wang, R.P.H. Chang, Random laser action in semiconductor powder, Phys. Rev. Lett. 82 (1999) 2278.

[68] C.M. Soukoulis, X. Jiang, J.Y. Xu, H. Cao, Dynamic response and relaxation oscillations in random lasers, Phys. Rev. B. 65 (2002) 41103.

[69] V.F. Zolin, The nature of plaser-powdered laser, J. Alloys Compd. 300 (2000) 214–217.

[70] N.M. Lawandy, R.M. Balachandran, A.S.L. Gomes, E. Sauvain, Laser action in strongly scattering media, Nature. 368 (1994) 436–438.

[71] M.A. Noginov, G. Zhu, A.M. Belgrave, R. Bakker, V.M. Shalaev, E.E. Narimanov, S. Stout, E. Herz, T. Suteewong, U. Wiesner, Demonstration of a spaser-based nanolaser, Nature. 460 (2009) 1110–1112.

[72] X. Meng, K. Fujita, S. Murai, T. Matoba, K. Tanaka, Plasmonically Controlled Lasing Resonance with Metallic− Dielectric Core− Shell Nanoparticles, Nano Lett. 11 (2011) 1374–1378.

[73] J.M. Pitarke, V.M. Silkin, E. V Chulkov, P.M. Echenique, Theory of surface plasmons and surface-plasmon polaritons, Reports Prog. Phys. 70 (2006) 1.

[74] K.A. Willets, R.P. Van Duyne, Localized surface plasmon resonance spectroscopy and sensing, Annu. Rev. Phys. Chem. 58 (2007) 267–297.

[75] M. Li, S.K. Cushing, N. Wu, Plasmon-enhanced optical sensors: a review, Analyst. 140 (2015) 386–406.

[76] D. Sarid, W.A. Challener, Modern introduction to surface plasmons: theory, Mathematica modeling, and applications, Cambridge University Press, 2010.

[77] N. Umemura, K. Yoshida, K. Kato, Phase-matching properties of KNbO3 in the mid-infrared, Appl. Opt. 38 (1999) 991–994.

[78] J. Solé, L. Bausa, D. Jaque, An introduction to the optical spectroscopy of inorganic solids, John Wiley & Sons, 2005.

[79] P. Herve, L.K.J. Vandamme, General relation between refractive index and energy gap in semiconductors, Infrared Phys. Technol. 35 (1994) 609–615.

[80] N.M. Ravindra, P. Ganapathy, J. Choi, Energy gap–refractive index relations in semiconductors–An overview, Infrared Phys. Technol. 50 (2007) 21–29.

[81] C.A. Schneider, W.S. Rasband, K.W. Eliceiri, NIH Image to ImageJ: 25 years of image analysis, Nat. Methods. 9 (2012) 671–675.

[82] V. Favre-Nicolin, R. Černý, FOX,free objects for crystallography': a modular approach to ab initio structure determination from powder diffraction, J. Appl. Crystallogr. 35 (2002) 734–743. http://objcryst.sourceforge.net.

[83] T. Degen, M. Sadki, E. Bron, U. König, G. Nénert, The highscore suite, Powder Diffr. 29 (2014) S13–S18.

[84] P. Villars, K. Cenzual, eds., EuTiNbO6 Crystal Structure: Datasheet from “PAULING FILE Multinaries Edition – 2012” in SpringerMaterials, (n.d.). https://materials.springer.com/isp/crystallographic/docs/sd_0310759.

[85] J. Perl, J. Shin, J. Schümann, B. Faddegon, H. Paganetti, TOPAS: an innovative proton Monte Carlo platform for research and clinical applications, Med. Phys. 39 (2012) 6818–6837.

[86] M. Wojdyr, Fityk: a general-purpose peak fitting program, J. Appl. Crystallogr. 43 (2010) 1126–1128.

[87] D. London, The barite roses of Oklahoma, Mineral. Rec. 39 (2008) 277.

[88] Z.A.D. Lethbridge, J.J. Williams, R.I. Walton, K.E. Evans, C.W. Smith, Methods for the synthesis of large crystals of silicate zeolites, Microporous Mesoporous Mater. 79 (2005) 339–352.

[89] F. Di Renzo, Zeolites as tailor-made catalysts: control of the crystal size, Catal. Today. 41 (1998) 37–40.

[90] H. Ghobarkar, O. Schäf, B. Paz, P. Knauth, Zeolite synthesis by simulation of their natural formation conditions: from macroscopic to nanosized crystals, J. Solid State Chem. 173 (2003) 27–31.

[91] R. Mostowicz, J.M. Berak, Factors influencing the crystal morphology of ZSM-5 type zeolites, in: Stud. Surf. Sci. Catal., Elsevier, 1985: pp. 65–72.

[92] S.G. Fegan, B.M. Lowe, Effect of alkalinity on the crystallisation of silicalite-1 precursors, J. Chem. Soc. Faraday Trans. 1 Phys. Chem. Condens. Phases. 82 (1986) 785–799.

[93] J.Y. Park, K. Kattel, W. Xu, H.G. Kim, E.J. Lee, G.H. Lee, J.J. Lee, Y. Chang, T.J. Kim, Longitudinal water proton relaxivities of Gd(OH)3 nanorods, Gd(OH)3 nanoparticles, and Gd2O3 nanoparticles: dependence on particle diameter, composition, and morphology, J.

Korean Phys. Soc. 59 (2011) 2376–2380.

[94] P.M. Diehm, P. Ágoston, K. Albe, Size-dependent lattice expansion in nanoparticles: reality or anomaly?, ChemPhysChem. 13 (2012) 2443–2454.

[95] A. Cimino, P. Porta, M. Valigi, Dependence of the lattice parameter of magnesium oxide on crystallite size, J. Am. Ceram. Soc. 49 (1966) 152–156.

[96] J.M. Jehng, I.E. Wachs, Structural chemistry and Raman spectra of niobium oxides, Chem. Mater. 3 (1991) 100–107.

[97] J. Hou, R. Zhou, J. Zhang, Z. Wang, Z. Zhang, Z. Ding, Pressure and temperature study on the structural stability of GdNbO4: Eu3+, J. Phys. Chem. C. 121 (2017) 14787–14794.

[98] J. Pellicer-Porres, A.B. Garg, D. Vázquez-Socorro, D. Martínez-García, C. Popescu, D. Errandonea, Stability of the fergusonite phase in GdNbO4 by high pressure XRD and Raman experiments, J. Solid State Chem. 251 (2017) 14–18.

[99] M. Yang, X. Zhao, Y. Ji, F. Liu, W. Liu, J. Sun, X. Liu, Hydrothermal approach and luminescent properties for the synthesis of orthoniobates GdNbO 4: Ln 3+(Ln= Dy, Eu) single crystals under high-temperature high-pressure conditions, New J. Chem. 38 (2014) 4249–4257.

[100] A. John, S. Joseph, K.M. Manu, J.K. Thomas, S. Solomon, Structure, microwave dielectric and optical properties of Ln2/3Gd1/3TiNbO6 (Ln= Ce, Pr, Nd and Sm) ceramics, J. Mater. Sci. Mater. Electron. 22 (2011) 776–780.

[101] P. Colomban, A. Slodczyk, Raman intensity: an important tool in the study of nanomaterials and nanostructures, Acta Phys. Pol. A Gen. Phys. 116 (2009) 7.

[102] A. Slodczyk, P. Colomban, S. Willemin, O. Lacroix, B. Sala, Indirect

Raman identification of the proton insertion in the high-temperature [Ba/Sr][Zr/Ti] O3-modified perovskite protonic conductors, J. Raman Spectrosc. An Int. J. Orig. Work All Asp. Raman Spectrosc. Incl. High. Order Process. Also Brillouin Rayleigh Scatt. 40 (2009) 513–521.

[103] F.D. Hardcastle, I.E. Wachs, Determination of niobium-oxygen bond distances and bond orders by Raman spectroscopy, Solid State Ionics. 45 (1991) 201–213.

[104] R.M. Pittman, A.T. Bell, Raman studies of the structure of niobium oxide/titanium oxide (Nb2O5. TiO2), J. Phys. Chem. 97 (1993) 12178–12185.

[105] K. Nakajima, Y. Baba, R. Noma, M. Kitano, J. N. Kondo, S. Hayashi, M. Hara, Nb2O5· nH2O as a heterogeneous catalyst with water-tolerant Lewis acid sites, J. Am. Chem. Soc. 133 (2011) 4224–4227.

[106] L.J. Burcham, J. Datka, I.E. Wachs, In situ vibrational spectroscopy studies of supported niobium oxide catalysts, J. Phys. Chem. B. 103 (1999) 6015–6024.

[107] H.T. Kreissl, M.M.J. Li, Y.-K. Peng, K. Nakagawa, T.J.N. Hooper, J. V Hanna, A. Shepherd, T.-S. Wu, Y.-L. Soo, S.C.E. Tsang, Structural studies of bulk to nanosize niobium oxides with correlation to their acidity, J. Am. Chem. Soc. 139 (2017) 12670–12680.

[108] H. AZUMA, N. FUJI, Multi Kubelka Analysis of VIS-NIR Reflectance Spectra, in: Lunar Planet. Sci. Conf., 1990.

[109] J. Tauc, R. Grigorovici, A. Vancu, Optical properties and electronic structure of amorphous germanium, Phys. Status Solidi. 15 (1966) 627–637.

[110] P. Makuła, M. Pacia, W. Macyk, How to correctly determine the band gap energy of modified semiconductor photocatalysts based on UV–Vis spectra, (2018).

[111] R. López, R. Gómez, Band-gap energy estimation from diffuse reflectance measurements on sol–gel and commercial TiO2: a comparative study, J. Sol-Gel Sci. Technol. 61 (2012) 1–7.

[112] H. Peelaers, C.G. Van de Walle, Effects of strain on band structure and effective masses in MoS2, Phys. Rev. B. 86 (2012) 241401.

[113] D.B. Migas, L. Miglio, Band-gap modifications of β− FeSi2 with lattice distortions corresponding to the epitaxial relationships on Si (111), Phys. Rev. B. 62 (2000) 11063.

[114] Y. Zhang, J. Wang, J. Ren, X. Liu, X. Li, Y. Xia, G. Lu, Y. Wang, Mesoporous niobium phosphate: an excellent solid acid for the dehydration of fructose to 5-hydroxymethylfurfural in water, Catal. Sci. Technol. 2 (2012) 2485–2491.

[115] K. Hadjiivanov, Identification and characterization of surface hydroxyl groups by infrared spectroscopy, Adv. Catal. 57 (2014) 99–318.

[116] L.M. Parker, D.M. Bibby, G.R. Burns, An infrared study of H2O and D2O on HZSM-5 and DZSM-5, Zeolites. 13 (1993) 107–112.

[117] M. Shabanian, M. Hajibeygi, A. Raeisi, FTIR characterization of layered double hydroxides and modified layered double hydroxides, in: Layer. Double Hydroxide Polym. Nanocomposites, Elsevier, 2020: pp. 77–101.

[118] Y. Zheng, C. Chen, Y. Zhan, X. Lin, Q. Zheng, K. Wei, J. Zhu, Y. Zhu, Luminescence and photocatalytic activity of ZnO nanocrystals: correlation between structure and property, Inorg. Chem. 46 (2007) 6675–6682.

[119] M. Montero-Muñoz, J.E. Ramos-Ibarra, J.E. Rodríguez-Páez, G.E. Marques, M.D. Teodoro, J.A.H. Coaquira, Growth and formation mechanism of shape-selective preparation of ZnO structures: correlation of structural, vibrational and optical properties, Phys. Chem. Chem.

Phys. 22 (2020) 7329–7339.

[120] T. Kotsokechagia, F. Cellesi, A. Thomas, M. Niederberger, N. Tirelli, Preparation of ligand-free TiO2 (anatase) nanoparticles through a nonaqueous process and their surface functionalization, Langmuir. 24 (2008) 6988–6997.

[121] L.T. Zhuravlev, Concentration of hydroxyl groups on the surface of amorphous silicas, Langmuir. 3 (1987) 316–318.

[122] C. Nico, T. Monteiro, M.P.F. Graça, Niobium oxides and niobates physical properties: Review and prospects, Prog. Mater. Sci. 80 (2016) 1–37.

[123] A. Gupta, M. Mittal, M.K. Singh, S.L. Suib, O.P. Pandey, Low temperature synthesis of NbC/C nano-composites as visible light photoactive catalyst, Sci. Rep. 8 (2018) 1–17.

[124] X. Liu, S.M. Sadaf, M. Son, J. Shin, J. Park, J. Lee, S. Park, H. Hwang, Diode-less bilayer oxide (WOx–NbOx) device for cross-point resistive memory applications, Nanotechnology. 22 (2011) 475702.

[125] K. Jung, Y. Kim, Y.S. Park, W. Jung, J. Choi, B. Park, H. Kim, W. Kim, J. Hong, H. Im, Unipolar resistive switching in insulating niobium oxide film and probing electroforming induced metallic components, J. Appl. Phys. 109 (2011) 54511.

[126] J. Halim, K.M. Cook, M. Naguib, P. Eklund, Y. Gogotsi, J. Rosen, M.W. Barsoum, X-ray photoelectron spectroscopy of select multi-layered transition metal carbides (MXenes), Appl. Surf. Sci. 362 (2016) 406–417.

[127] J. Chastain, R.C. King Jr, Handbook of X-ray photoelectron spectroscopy, Perkin-Elmer, USA. (1992) 261.

[128] G. Blasse, Luminescence processes in niobates with fergusonite structure, J. Lumin. 14 (1976) 231–233.

[129] Z. Zhang, G. Chen, K. Xu, Photoluminescence of colloids of pristine ZnAl layered double hydroxides, Ind. Eng. Chem. Res. 52 (2013) 11045–11049.

[130] K. Xu, Z. Zhang, G. Chen, J. Shen, Photoluminescence of colloids of pristine MgAl layered double hydroxides, RSC Adv. 4 (2014) 19218–19220.

[131] A. Dwivedi, K. Mishra, S.B. Rai, Role of Gd3+ ion on downshifting and upconversion emission properties of Pr3+, Yb3+ co-doped YNbO4 phosphor and sensitization effect of Bi3+ ion, J. Appl. Phys. 120 (2016) 43102.

[132] Y. Hong, J.W.Y. Lam, B.Z. Tang, Aggregation-induced emission: phenomenon, mechanism and applications, Chem. Commun. (2009) 4332–4353.

[133] D. Li, X. Wang, C. Han, Study on the fluorescence spectra characteristics of vinegar-water solutions, J. Spectrosc. 2016 (2016).

[134] R.D. Shannon, Revised effective ionic radii and systematic studies of interatomic distances in halides and chalcogenides, Acta Crystallogr. Sect. A Cryst. Physics, Diffraction, Theor. Gen. Crystallogr. 32 (1976) 751–767.

[135] R. Zamiri, A.F. Lemos, A. Reblo, H.A. Ahangar, J.M.F. Ferreira, Effects of rare-earth (Er, La and Yb) doping on morphology and structure properties of ZnO nanostructures prepared by wet chemical method, Ceram. Int. 40 (2014) 523–529.

[136] L.J. Borrero-González, L.A.O. Nunes, Near-infrared quantum cutting through a three-step energy transfer process in Nd3+–Yb3+ co-doped fluoroindogallate glasses, J. Phys. Condens. Matter. 24 (2012) 385501.

[137] J. Sun, Y. Sun, C. Cao, Z. Xia, H. Du, Near-infrared luminescence and quantum cutting mechanism in CaWO4: Nd3+, Yb3+, Appl. Phys. B.

111 (2013) 367–371.

[138] S.S. Sinha, A. Zak, R. Rosentsveig, I. Pinkas, R. Tenne, L. Yadgarov, Size-Dependent Control of Exciton–Polariton Interactions in WS2 Nanotubes, Small. 16 (2020) 1904390.

[139] S. Ning, Z. Wu, H. Dong, L. Ma, B. Jiao, L. Ding, L. Ding, F. Zhang, The enhanced random lasing from dye-doped polymer films with different-sized silver nanoparticles, Org. Electron. 30 (2016) 165–170.

[140] T. Zhai, X. Zhang, Z. Pang, X. Su, H. Liu, S. Feng, L. Wang, Random laser based on waveguided plasmonic gain channels, Nano Lett. 11 (2011) 4295–4298.

[141] V.D. Ryzhikov, B. V Grinev, E.N. Pirogov, G.M. Onyshchenko, A.I. Ivanov, V.G. Bondar, K.A. Katrunov, S. Al Kostyukevych, Use of gadolinium oxyorthosilicate scintillators in x-ray radiometers, Opt. Eng. 44 (2005) 16403.

[142] K.A. GschneidnerJr, V.K. Pecharsky, A.O. Tsokol, Recent developments in magnetocaloric materials, Reports Prog. Phys. 68 (2005) 1479.

[143] U. Kamber, A. Bergman, A. Eich, D. Iuşan, M. Steinbrecher, N. Hauptmann, L. Nordström, M.I. Katsnelson, D. Wegner, O. Eriksson, Self-induced spin glass state in elemental and crystalline neodymium, Science (80-.). 368 (2020).

[144] M.R. Anoop, P.S. Binil, S. Suma, M.R. Sudarsanakumar, Synthesis and spectral characterization of lanthanide complexes with 1, 2-diphenyl-4-butyl-3, 5-pyrazolidinedione: luminescent property of Tb (III) complex, J. Rare Earths. 30 (2012) 709–715.

[145] T. Pellegrino, S. Kudera, T. Liedl, A. Muñoz Javier, L. Manna, W.J. Parak, On the development of colloidal nanoparticles towards multifunctional structures and their possible use for biological

applications, Small. 1 (2005) 48–63.

[146] A. Escudero, A.I. Becerro, C. Carrillo-Carrión, N.O. Nunez, M. V Zyuzin, M. Laguna, D. González-Mancebo, M. Ocaña, W.J. Parak, Rare earth based nanostructured materials: synthesis, functionalization, properties and bioimaging and biosensing applications, Nanophotonics. 6 (2017) 881–921.